6-13-2013

Optically Pumped Atomic Rubidium Lasers: Two-Photon and Exciplex Excitation Mechanisms

Jeffrey E. Gallagher

Optically Pumped Atomic Rubidium Lasers: Two-Photon and Exciplex Excitation Mechanisms

DISSERTATION

Jeffrey E. Gallagher, Major, USAF

AFIT-ENP-DS-13-J-01

DEPARTMENT OF THE AIR FORCE
AIR UNIVERSITY

AIR FORCE INSTITUTE OF TECHNOLOGY

Wright-Patterson Air Force Base, Ohio

AFIT-ENP-DS-13-J-01

OPTICALLY PUMPED ATOMIC RUBIDIUM LASERS: TWO-PHOTON AND EXCIPLEX EXCITATION MECHANISMS

DISSERTATION

Presented to the Faculty

Graduate School of Engineering and Management

Air Force Institute of Technology

Air University

Air Education and Training Command

in Partial Fulfillment of the Requirements for the

Degree of Doctor of Philosophy

Jeffrey E. Gallagher, B.S., M.S.

Major, USAF

June 2013

AFIT-ENP-DS-13-J-01

OPTICALLY PUMPED ATOMIC RUBIDIUM LASERS: TWO-PHOTON AND EXCIPLEX EXCITATION MECHANISMS

Jeffrey E. Gallagher, B.S., M.S.
Major, USAF

Approved:

Glen P. Perram, PhD (Chairman)	7 June 2013 Date
David Weeks, PhD (Member)	7 June 2013 Date
Jeremy C. Holtgrave, PhD (Member)	7 June 2013 Date
Doug Petkie, PhD (Member)	7 June 2013 Date

Accepted:

Heidi R. Ries, PhD Interim Dean, Graduate School of Engineering and Management	11 June 2013 Date

AFIT-ENP-DS-13-J-01

Abstract

The Doppler-broadened two-photon absorption (TPA) cross-section for the $5^2S_{1/2} \longrightarrow 5^2D_{5/2}$ transition in Rb is measured using direct absorption methods. The selection rule $|\Delta F| \leq 2$ applied to both isotopes yields 17 transitions in 3 Doppler limited lines. A detailed model of the intensity profile was also developed to account for a focused Gaussian beam (with an M^2 value of 1.09) propagating through a two-photon absorption medium. A peak absorbance of 24% was observed for an intensity of 6.28 $\frac{kW}{cm^2}$ at the focus, a Rb density of $4.6 \times 10^{15}\ cm^{-3}$, and a path length of 15 cm. Alkali concentrations from $1.61 - 8.52 \times 10^{15}\ cm^{-3}$ were monitored in the far wing of the D_2 line. Extracting the hyperfine-broadened TPA cross-section from 87 test configurations, while varying the pump power, alkali concentration and focal length, yielded an error-weighted average of $6.75 \times 10^{-21} \frac{cm^4}{W}$ with a standard deviation of $3.61 \times 10^{-21} \frac{cm^4}{W}$. This cross-section is sufficient for a pulsed dye laser to bleach the pump transition in the Two-Photon Pumped Alkali Laser (TPAL) that lases at 420 nm and 5.2 μm.

Optically pumped atomic rubidium lasers pumped in the blue satellite of the D_2 line from the ground Rb-Ar or Rb-Kr collision pair to the dissociative $B^2\Sigma^+_{1/2}$ state produce laser emission at 780.2 nm. Lasing is achieved for pump wavelengths of 752.3 to greater than 760 nm for the Rb-Ar system and $757.1 - 760.4$ nm for the Rb-Kr system. Slope efficiencies increase with both Rb and Ar concentrations and exceed 0.25% using a heat pipe configuration. The gain is very high with photon build-up times of $1 - 3.7$ ns. Laser induced heating and subsequent condensation of alkali vapor in the heat pipe configuration currently limits operation to less than 2500 $Torr$.

Acknowledgements

First and foremost, I want to thank my wife and 4 children for the support and persevering encouragements they provided me while I pursued this chapter of my life. I want to especially recognize my third child, who never wavered praying for me to finish, even when I had to continue in my next duty station.

I next want to thank my professor, Dr. Glen Perram, for the unlimited amount of guidance he provided in both the experimental and theoretical areas of laser physics. I especially appreciate his support on and off duty hours working with me while I was stationed in California.

I want to thank the members of the DPAL research group during my stay at AFIT. Their encouragement during our time in classes, and recommendations while in the lab were invaluable.

Finally, I want to thank the High Energy Laser Joint Technology Office (HEL JTO) for the opportunity to perform the research contained in these pages.

Jeffrey E. Gallagher

Table of Contents

Page

List of Figures

Figure Page

Figure Page

Figure Page

List of Tables

List of Abbreviations

Abbreviation		Page
AFIT	Air Force Institute of Technology	4
Cs	cesium	1
DPAL	Diode-Pumped Alkali Laser	1
PBGFs	hollow-core photonic-band-gap fiber	14
Rb	rubidium	1
TPAL	Two-Photon Pumped Alkali Laser	2
UIUC	University of Illinois, Urbana-Champaign	4
XPAL	Exciplex Pumped Alkali Laser	2

OPTICALLY PUMPED ATOMIC RUBIDIUM LASERS: TWO-PHOTON AND EXCIPLEX EXCITATION MECHANISMS

I. Introduction

Ever since the effective demonstration of the Diode-Pumped Alkali Laser (DPAL) by Krupke et al. in 2003 [65], the laser community has focused much of their attention on investigating this field in the hopes of developing a non-chemical high power laser. The alkali laser is very promising for many reasons. First of all, the DPAL is not a chemical laser, so it does not require the storage or the replenishment of highly toxic chemicals. Instead, the DPAL lasing medium is the alkali vapor contained neatly and compactly inside a glass cell the size of a spool of thread. This alkali vapor is also reusable as the same atom is cycled through the process 100 million times every second. The DPAL system is also not a solid state laser, so it does not have the thermal issues attributed to such a device as pump powers are increased. In fact, there is minimal heat generated in the entire process since the only heat generated originates from the relaxing of the atom from the $n^2P_{3/2}$ state (where n=3,4,5 & 6 corresponding to Na, K, Rb & Cs respectively) down to the $n^2P_{1/2}$ state. This gap represents 238 cm^{-1} to 554 cm^{-1} for rubidium (Rb) and cesium (Cs) respectively and these are both on the order of magnitude of kT at room temperature.

The mechanics of the DPAL system are also quite simple. Using the cesium atom as an example, the pump laser operating at 852 nm excites the ground state ($6^2S_{1/2}$) atom to the $6^2P_{3/2}$ state. Collisional mixing then relaxes the atom to the $6^2P_{1/2}$ state. Population inversion then occurs between the $6^2P_{1/2}$ state and the ground state where lasing occurs at 895 nm. This particular wavelength is in the near-infrared band. For

a more detailed discussion of this process please refer to the papers prepared by Krupke et al. [65, 66].

More recently, higher order variants to the DPAL have been reported to lase back to the ground state. These variants may draw population away from the regular DPAL but also increase the number of wavelengths at which DPAL-like lasers have access to. This research reports findings on two variants, the Exciplex Pumped Alkali Laser (XPAL) and the Two-Photon Pumped Alkali Laser (TPAL).

The TPAL is pumped through a virtual state, halfway between the alkali ground state and the target pump level. As the alkali atom encounters a photon at the frequency of the virtual state, the atom simultaneously absorbs two identical photons moving population to the real pump state. In 2008, Sulham et al. demonstrated that a Cs TPAL system will simultaneously yield a "blue" and a mid-IR lasing wavelength [16, 40, 55] in a cascade effect down to the ground state. The mechanism for achieving population inversion in this upper state is more involved than the originally designed DPAL system, but the applications for such a device are desirable[1]. This research reports the absolute two-photon absorption (TPA) cross-section for the $5^2S_{1/2} \longrightarrow 5^2D_{5/2}$ transition in a Rb vapor, in an effort to understand pump intensity thresholds for a possible Rb TPAL. Although the TPA cross-section for this transition in Rb was first measured in 1983 by Zapka et al., there has been subsequent groups reporting values that differ by as much as a factor of 100. To restore confidence in the true value, this research varied alkali concentration, the beam waist and pump power to generate 87 different test configurations. The resultant average number, weighted against the error of each test case, is reported and compared.

The XPAL system is pumped in the blue satellite wing of the D_2 line and lases either on the D_2 or D_1 line [34, 35, 36, 37, 38]. A pulsed XPAL was first demonstrated

[1]Such applications are under water communications, low diffraction HEL, and IR counter measures at multiple wavelengths

in 2009 by pumping Cs-Ar excimers in a mixture of 500 $Torr$ of argon and 100 $Torr$ of ethane. The excited excimer then populates the upper laser level ($^2P_{1/2}$) in atomic cesium by decay [35]. Lasing occurs on the D_1 line at 894.3 nm after spin-orbit relaxation, aided by the ethane. The excimer step creates a broad band of pump wavelegths ($\approx$ 5 nm) and removes the requirement for hydrocarbons [34, 35, 36, 37, 38]. The four-level Cs-Ar system exhibits a threshold at $130 - 250$ J in a 4 ns pulse with an efficiency of about 1% and has been scaled in pump rate to 2-3 times threshold [4, 36, 37]. This research extends the four-level XPAL work by lasing in Rb-Ar and Rb-Kr mixtures and reports slope efficiencies and laser output powers. This research was the first to use a heat pipe configuration for the XPAL, and was the first to explore rare-gas pressures of up to 2500 $Torr$.

II. Previous Work

The motivation for the Rb TPAL originated from an experiment performed in the summer of 2009 by a team at the Air Force Institute of Technology (AFIT). During the course of tuning a Spectra Physics Nd:YAG pumped Sirah dye laser[1] to various excited states in atomic rubidium in an energy pooling experiment, a bright blue dot was noticed parallel to the pump beam. It was later realized that this occurred when the laser was tuned slightly off resonance near the $5^2P_{3/2}$ state in Rb. Due to the nature of the experiment, the rubidium cell was only being interrogated by a pump laser, so no resonator existed around the cell. It was reported that ASE occurred at about 420 nm and in the Mid-IR in a range from 3.85 - 5.2 μm.

The motivation for the Rb XPAL came from the joint work performed by the DPAL group at AFIT and the XPAL group at the University of Illinois, Urbana-Champaigne (UIUC) [33]. The same Spectra Physics Nd:YAG pumped Sirah dye laser above was used to pump a 17 cm long pyrex cell with a Rb-Ar mixture inside. Slope efficiencies were investigated maintaining constant temperature and pressure.

2.1 The One-Photon Pump Alkali Lasers

Krupke's Diode-Pumped Alkali Laser (DPAL).

In 2003, William Krupke patented the design of the first diode-pumped alkali laser system [65]. Although this was a first-of-a-kind laser system, the alkali vapors were well known by spectroscopists. As early as 1958, Schawlow and Townes [61] used the potassium vapor to push the maser technology into the optical and IR wavelengths. In 1962, two years after the establishment of the laser [51], Rabinowitz et al. was the first to demonstrate an alkali vapor as an actual gain medium in his continuous

[1]This laser delivered up to 100 mJ in 10 ns at 10 Hz.

optically pumped cesium laser [54]. This concept did not gain a strong footing in the laser community since little can be found in the literature afterwards. This is probably due to the lack of efficient pump diodes at the time. For the next four decades, the alkali vapors moved away from being the gain medium to becoming the the work horses in areas such as metrology and spectroscopy. High-power pulsed and cw lasers radiated sealed glass cells containing alkali vapors while the side fluorescence was collected and analyzed to determine important atomic and molecular properties. The cesium atom in particular is probably the most characterized atom next to hydrogen as the unit of time, the second, is defined in terms of 9,192,631,770 periods of the radiation corresponding to the transition between the two hyperfine levels of the ground state of cesium [13]. As a result, the second has become the unit with the smallest uncertainty. The affinity towards the alkali in the scientific community is due primarily to their atomic structure. They possess one valence electron making it hydrogen-like, such as having a smaller than usual ionization energy. Compared to other atoms it doesn't take a significant amount of energy to excite the atom. Therefore, the chemistry, spectroscopy and the kinetics of the alkalis were all a fairly mature concept by the time William Krupke developed the DPAL.

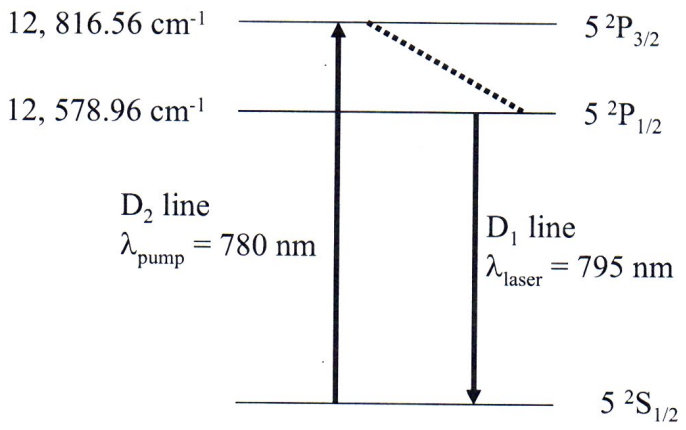

Figure 1. This is the three-level diagram for the DPAL system using the rubidium vapor as the gain medium [66].

Krupke's DPAL functions in the following manner. All alkali vapors have a ground atomic state of $^2S_{1/2}$, with the next two excited states being $^2P_{1/2}$ and $^2P_{3/2}$. There are two electric-dipole allowed transitions in this three-level system. These transitions, the $^2S_{1/2}$-$^2P_{1/2}$ and the $^2S_{1/2}$-$^2P_{3/2}$, are more commonly called the D_1 and the D_2 lines respectively (see Figure 1). The D_2 transition is the pump transition. So, the pump laser for a rubidium cell would be tuned to the 780 nm wavelength in order to move population from the ground state to the $5^2P_{3/2}$ level. The natural lifetimes for the $5^2P_{3/2}$ and the $5^2P_{1/2}$ states are 26.2 ns and 27.7 ns respectively [64]. The population would normally bottle-neck in the upper state because the spin-orbit relaxation rate is slow compared to the pump rate. To compensate for this, a buffer gas is added on the order of 1 atmosphere to increase the relaxation rate from $5^2P_{3/2}$ down to $5^2P_{1/2}$. Finally, with population inversion achieved between the $^2P_{1/2}$ state and the ground state, lasing in the DPAL occurs. At this point the process is able to start all over again for the alkali atom, since the pump laser is still radiating the cell. For a more in-depth study of the DPAL laser please refer to the following articles by Krupke, Beach, Page and Zhdanov [11, 12, 56, 58, 65, 66].

One of the acknowledged challenges to the DPAL system is the narrowness of the spectral width of the D_2 transition (approx. 10 GHz at 1 atmosphere). This becomes a problem when developing a high power laser, because the spectral width from bars and stacks in a semiconductor pump laser at high powers is about 100 times larger than that. One way engineers have tried to mitigate this is to broaden the spectral width of D_2 by adding inert gases to the alkali vapor. This broadening comes at no small cost since enough inert gas must be added to increase the pressure up to 25-50 atmospheres.

2.2 Two-Photon Absorption Spectroscopy

The theory of two-photon absorption using a virtual intermediate state is not new to the scientific community. In fact, the theory is just about as old as the theory of quantum mechanics itself. In 1931, Maria Göppert-Mayer published an article in the Annalen Der Physik pioneering the framework of the theory of two-photon absorption [25] from the then new field of quantum mechanics. This theory remained unproven for three decades waiting for the invention of the laser[2] in 1960 by Maimen[51]. The theory of two-photon absorption was finally confirmed in an experiment using an europium-doped calcium fluoride crystal by Kaiser et al. in 1961 [44], and then in a cesium vapor by Abella in 1962 [8]. For the next several years many articles were published exploring this new field of spectroscopy. Much of the research focused on multiphoton ionization, whether it was of hydrogen and rare-gas atoms [14] or of the alkali atoms [15]. There was also some work done in 1965 and 1967 investigating the infrared emission during the two-photon excitation of the $6^2S_{1/2}$ state in potassium vapors [60, 68]. Recall that the group at AFIT in 2009 concluded that there were IR emission in their two-photon excitation experiment with a rubidium vapor. Another more attractive attribute of the two-photon absorption spectroscopy is the ability to directly access states that are forbidden in one photon transitions [22].

The 1970's saw the emergence of two-photon Doppler-free spectroscopy. This allowed some states to be directly accessible which were once inaccessible due to parity incompatibility [29]. This also allowed the hyperfine structure of high-lying states to be more accurately resolved and consequently the hyperfine splitting to be determined with greater fidelity. One such study was done by a group at Harvard University in

[2]Although Gordon Gould published the term LASER in 1959[26], the laser was also referred to as an optical maser at this time.

1974 [47]. They studied the $3^2S_{1/2}$-$5^2S_{1/2}$ transition in a sodium vapor and determined the hyperfine splitting for the $5^2S_{1/2}$ state to be $101 \pm 15\ MHz$. With the invention of the Ti:Al_2O_3 (Ti-sapphire) laser in 1982 [52] the field of spectroscopy reached higher levels of fidelity. In contrast to the dye lasers, the Ti-sapphire laser had a tuning range that covered three regions of three different dyes, and was able to remain at high power for longer periods of time without degradation in beam quality. In addition to this, the Ti-sapphire laser reached higher output power and a narrower linewidth. Needless to say, this opened the door to better spectroscopy. In 1990, Adams et al. used a Ti-sapphire ring laser to perform high resolution spectroscopy of the $5^2S_{1/2} \leftarrow 5^2D_{5/2,3/2}$ transition [9] in rubidium. Adams et al. knew that the Doppler broadened linewidth

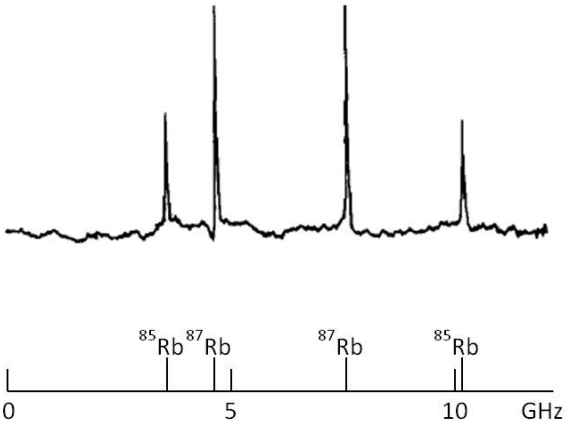

Figure 2. The rubidium $5^2S_{1/2} \rightarrow 5^2D_{3/2}$ transition obtained by Doppler-free two-photon absorption spectroscopy with a Ti:saphire laser [9].

of the $5^2S_{1/2} \rightarrow 5^2D_{3/2}$ transition at room temperature would be about 0.5 GHz. Therefore they chose to use Doppler-free two-photon absorption spectroscopy. Their results are shown in Figure 2. Also in 1990, Garreau et al. [32] used Doppler-free two-photon spectroscopy on atomic hydrogen and deuterium to gain a more accurate value of the Rydberg constant, R_∞[3]. They were able to achieve observed frequencies with an accuracy of 1 part in 10^9. In 2000, the Rydberg constant was again put

[3]The Rydberg constant is the most accurately known physical constant known to man.

to the test when Niering et al. measured the absolute frequency of the hydrogen $1^2S_{1/2} \leftarrow 2^2S_{1/2}$ two-photon transition with an accuracy of 1.8 parts in 10^{14} [50].

With the more recent development of laser cooling and trapping techniques, two-photon spectroscopy has been able to join magneto-optical trap systems to measure more precise two-photon ionization cross-sections [23]. In 2009 a non-linear optics team from the University of California expanded the generalized Kramers-Heisenberg expressions to include two-photon absorption [53]. Also in the late 2000's, two-photon absorption has been seen as an emerging player in the realm of quantum computing [27]. All of these examples indicate a need for recognizing the presence of and the mechanism behind two-photon absorption.

2.3 The Two-Photon Pump Alkali Lasers (TPAL)

Sulham et al. reported ASE from one or both 5^2P states when pumping the virtual states that correspond to the $5^2D_{3/2}, 5^2D_{5/2}$ and the $7^2S_{1/2}$ states (Figure 3). This group was also the first to construct a resonator based on the two-photon pump. However, three unexpected results occurred after constructing such a cavity. For one, the threshold decreased as the concentration of the alkali increased. Slope efficiencies tend to increase with alkali concentration, but it is anomalous for the threshold to decrease. Secondly, it was shown that the resonator actually degraded the power of the ASE line. This too is counterintuitive since the gain of the laser should increase as the optical path length increases. Thirdly, it was observed that the power out decreased as the concentration of He increased. This is unusual because the spectral width of the two-photon pumped $n^2S_{1/2} - n^2D_{5/2,3/2}$ transition is 6 times smaller than the spectral width of the pump laser, which in this case, is 16 GHz delivered by a Spectra Physics Nd:YAG pumped Sirah dye laser [16]. The He (or other rare gas) broadens the spectral width of the transition to better match the spectral width of

the pump laser.

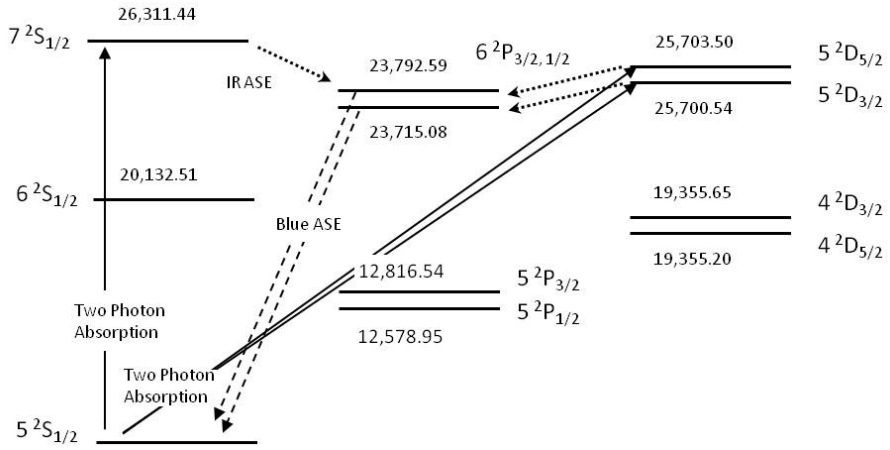

Figure 3. The Grotrian diagram for rubidium. The solid arrows are the two-photon pump transitions. The dotted arrows are the amplified stimulated IR emission lines. The dashed arrows are the amplified stimulated "blue" optical emission lines [16].

2.4 The Two-Photon Absorption Cross-Section

The two-photon absorption (TPA) cross-section, $\sigma_{2\phi}$, is an important quantity to know in order to calculate the pump intensity threshold for a potential two-photon absorption laser system. For the transition in this research there are two simultaneous laser transitions back to the ground state, see Figure 4, that can be taken advantage of by a Two-Photon Pumped Alkali Laser (TPAL).

Referring to Figure 4, the following rate equations can be derived to attain an approximation of the threshold condition.

$$\frac{dn_3}{dt} = \sigma_{2\phi}\frac{I_P^2}{h\nu_P}n_1 - \Gamma_{IR}n_3 \quad (1)$$

$$\frac{dn_2}{dt} = \Gamma_{IR}n_3 - A_{21}n_2 \quad (2)$$

where Γ_{IR} is the branching ratio for the first laser transition and A_{21} is the sponta-

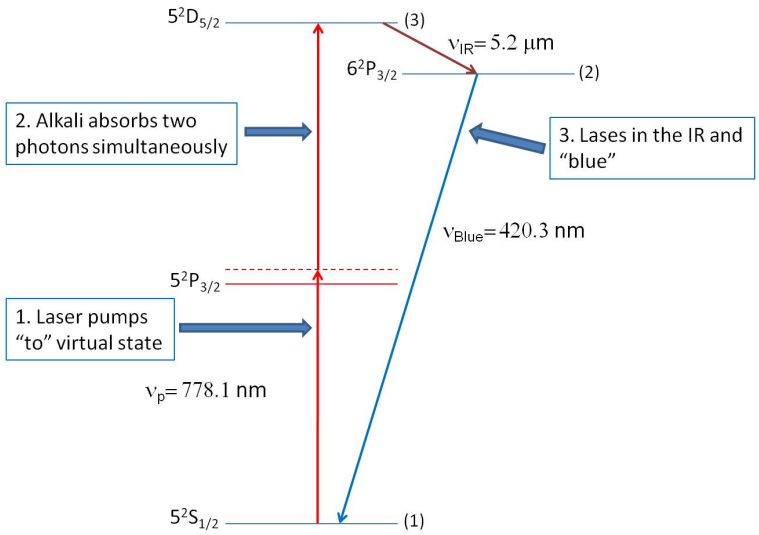

Figure 4. The three laser levels for the Two-Photon Pumped Alkali Laser (TPAL).

neous emission for the upper "blue" laser level. Applying a steady state condition to Equation 1, we can define an approximation to the laser threshold condition to be,

$$I_{th} = \sqrt{(h\nu_P)\frac{A_{21}}{\sigma_{2\phi}}\left(\frac{n_2}{n_1}\right)} \tag{3}$$

Assuming that we have no losses in the system, $\alpha \longrightarrow 0$, we can define the population ratio in Equation 3 to be equal to the degeneracy ratio, or 2. Equation 3 now shows the importance of knowing the TPA cross-section as a first step in developing a TPAL.

There have been a few reports on the value of the two-photon absorption cross-section of the transition $5^2S_{1/2} \longrightarrow 5^2D_{5/2}$ for rubidium. Table 1 displays the values of the TPA cross-section for the $5^2S_{1/2} \longrightarrow 5^2D_{5/2}$ transition from the literature. It is clear from this table that the value of the two-photon absorption cross-section is far from being well established. It is one goal of this research to establish a firm understanding of the true value by performing a comprehensive study of this transition in Rb.

The first value reported was in 1983 by Zapka et al. His group used Doppler-

Table 1. Two-photon absorption cross-sections measured for the $5^2S_{1/2} \longrightarrow 5^2D_{5/2}$ Transition in Rb.

$\sigma_{2\phi}\ \left(\frac{cm^4}{W}\right)$	Reference	Year	Type	Isotope
4×10^{-20}	Zapka *et al.* [67]	1983	Experimental	^{87}Rb
1.2×10^{-18}	Collins *et al.* [19]	1993	Experimental	^{85}Rb
0.57×10^{-18}	Marinescu *et al.* [49]	1994	Theoretical	^{85}Rb
6.5×10^{-20}	Saha *et al.* [43]	2011	Theoretical	^{85}Rb
$5\ \times10^{-20}$	Saha *et al.* [43]	2011	Experimental	^{85}Rb

free, frequency-modulation (FM) spectroscopy to detect the weak absorption in the $5^2S_{1/2} \longrightarrow 5^2D_{5/2}$ transition in an isotopically enriched Rb sample (number densities $^{85}Rb :^{87} Rb \approx 1:6$) [67]. A droplet of this isotropically enriched Rb was inserted into a glass cell, which was contained in an oven heated by coaxial wires and monitored by a thermocouple. Referring to Figure 5, a vertically-polarized single-mode cw pump laser (of about 120 mW) was set at frequency $\nu_0 \approx 12851\ cm^{-1}$ and traversed a polarizing beam splitter and a 15 cm focal length lens before entering the test cell. After recollimating, the beam passed a phase modulator that is driven by an rf oscillator at a frequency ν_{rf} between 100 and 600 MHz. After going through a quarter-wave plate the beam is reflected by an etalon, which acts as a perfect mirror at the two-photon pump frequency and becomes the probe beam back through the test cell. FM spectroscopy was performed by scanning the laser frequency ν_0 and keeping ν_{rf} constant. The absolute absorption of this transition was determined by calibrating the FM-absorption-shaped signal amplitude on a known reference absorption signal. This was done by tuning to one of the adjacent resonant frequencies of the etalon. This procedure then yielded an absolute absorption of 2.5% for the $5^2S_{1/2}(F=2) \longrightarrow 5^2D_{5/2}(F=4)$ transition in ^{87}Rb. A temperature of 182 ^0C amounted to a number density of about $3.3 \times 10^{14}\ cm^{-3}$. The carrier beam was estimated to be about 60 mW, with a beam waist of 70 μm. Under these conditions an approximate value

of $\sigma_{2\phi} = 4 \times 10^{-20}\ \frac{cm^4}{W}$ was determined and reported. Besides the Doppler-free techniques of counter-propagating beams, the experimental set-up in Zapka's work most closely resembled the set-up in our present work.

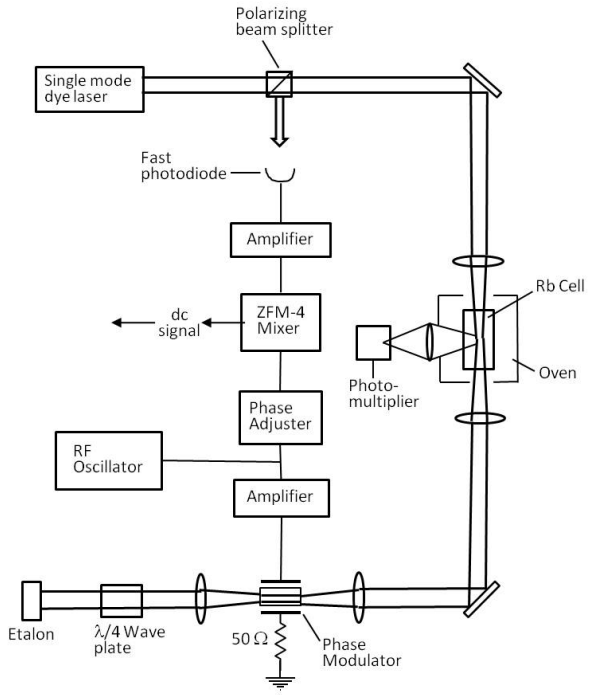

Figure 5. The apparatus used by Zapka et al. [67].

The second value wasn't reported until 10 years later by Collins et al. This group used Doppler free, differential absorption spectroscopy (DAS) with an external-grating-cavity cw diode laser, set at 100 $\frac{W}{cm^2}$, to tune through the $5^2S_{1/2}(F = 2) \longrightarrow 5^2D_{5/2}(F = 0, 1, 2, 3, 4)$ transitions of ^{85}Rb in a 2.54 cm long Pyrex cell containing a number density of $6.8 \times 10^{-18}\ cm^{-3}$ [19]. The absorption signal is detected by an electronic noise-canceling circuit that cancels up to 60 dB of common-mode noise. The laser frequency was swept with a triangle function at 400 Hz. The resulting absorption signal has a FWHM of 43 MHz, which is about 22 MHz larger than the range over which the hyperfine transition is distributed. It was reported that the added linewidth was contributed by a slight Doppler broadening (due to the coun-

terpropagating beams coming in at an angle of 0.95^0) and laser frequency jitter. Key to determining the TPA cross-section in this group was calculating the effective two-photon line strength, $S^{(2)}$. In reaching this number, Collins determines the integrated absorption coefficient and the total atomic excitation rate. The integrated absorption coefficient is found by integrating the absorption curve determined by fitting five Gaussian functions (corresponding to the five hyperfine lines) with the same FWHM to the absorption feature. Accuracy of the final number in this method becomes dependent on the knowledge of the factors involved for the FWHM of the absorption feature. Maintaining a temperature at 143 ^0C (i.e. $N = 6.8 \times 10^{13}\ cm^{-3}$) Collins et al. reported a number that was two orders of magnitude larger than Zapka et al. ten years earlier, $\sigma_{2\phi} = 1.2 \times 10^{-18}\ \frac{cm^4}{W}$.

One year later, Marinescu et al. reports a theoretical value based on modeling reduced absorption rates for this TPA transition [49]. The number that this group reported was $\sigma_{2\phi} = 0.57 \times 10^{-18}\ \frac{cm^4}{W}$. Unfortunately, the method Marinescu chose makes it extremely difficult to compare with this work's reported value.

Most recently in 2011, a TPA cross-section was measured by Saha et al. using low powers (1 mW) and low densities in a hollow-core photonic-band-gap fiber (PBGFs) filled with Rb vapor [43]. A $9 - cm$ long and 6 μm diameter hollow-core PBGF was mounted in a vacuum chamber connected to an Rb source containing naturally occurring Rb. The temperature of the chamber and finger were maintained at 85 ^0C and 55 ^0C respectively. After bake-out the background pressure was measured at $10^{-8}\ Torr$. An external cavity diode laser beam was split 50/50 to counterpropagate through the fiber of equal power and identical polarization. To generate the desired OD ($\approx$ 100) a highly off-resonant 20 mW desorption beam at 805 nm was also coupled to the fiber with an orthogonal polarization. They measured the TPA as a function of the intensity of light using an acouto-optic modulator (AOM) to vary

the intensity of the two counter-propagating beams simultaneously using a triangle wave at 1 kHz. The emitted blue photons are collected and detected from the top of the fiber. For a direct measure of the TPA from the 778.1 nm pump beams, they performed a lock-in detection by using another AOM, to modulate one of the two counter-propagating beams. A weak reflection of the forward propagating beam is collected by a photodiode. A 1% absorption was determined by detecting 30 nW of output blue flourescence at 420.3 nm with a 1 mW diode pump laser. With this method a direct absorption value was calculated to be 5×10^{-20} $\frac{cm^4}{W}$ for the $5^2S_{1/2} \longrightarrow 5^2D_{5/2}$ in ^{85}Rb. This value, although an order of magnitude different from Marinescu, came to within 20% of Zapka's reported value.

It is clear from the literature that an accepted value for the TPA cross-section for this particular transition in Rb has not been agreed upon. As stated earlier, developing a TPAL on this transition, requires knowledge of the TPA cross-section.

The Excimer Pumped Alkali Laser (XPAL).

Referring to Figure 6, the rubidium and argon combine to form the Rb-Ar excimer in it's ground state, $X^2\Sigma^+_{1/2}$. The pump laser excites the excimer to the blue wing of the repulsive $B^2\Sigma^+_{1/2}$ state which then quickly dissociates into a ground state argon atom and the excited $5^2P_{3/2}$ state of atomic rubidium. The remaining process mimics that of a regular DPAL, where the ethane aides in the spin orbit relaxing of the $5^2P_{3/2}$ state to the upper laser lever, the $5^2P_{1/2}$ state. The fifth level is the atomic ground state of Rb completing the XPAL process.

In the latter half of 2008, Readle et al. from the University of Illinois, devised a method to circumvent the spectral width problem mentioned above in the DPAL system. Instead of moving population from the ground state of an atomic alkali atom, they pumped the ground state of an excimer in the blue satellite (837 nm) to the

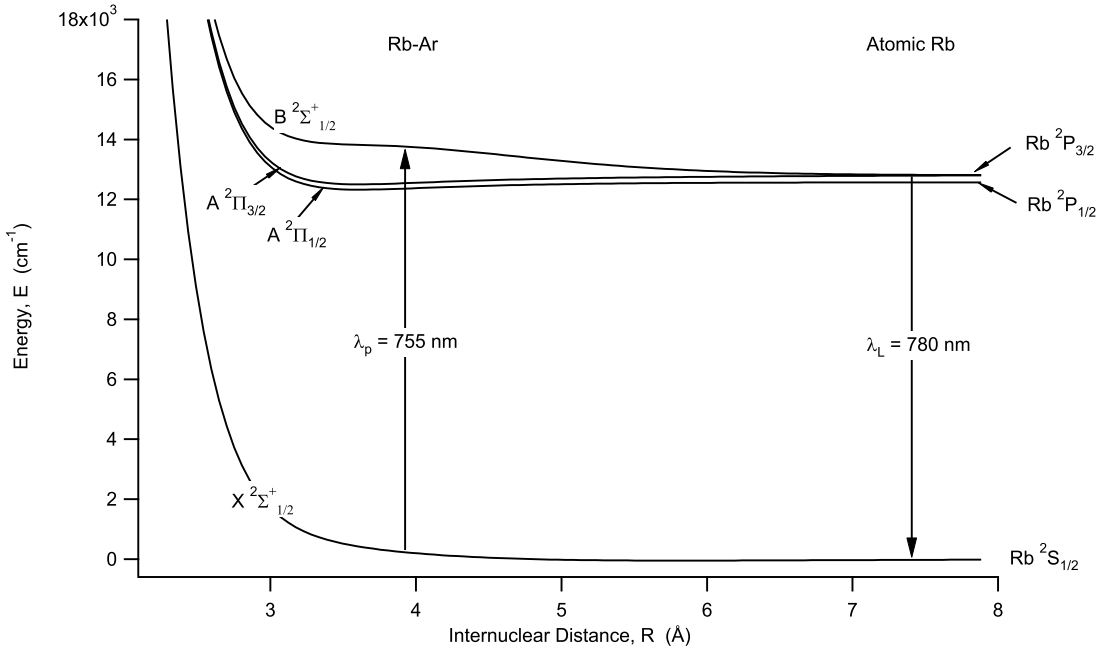

Figure 6. The first four Rb-Ar surfaces calculated by Blank et al. [46].

unstable $B^2\Sigma^+_{1/2}$ state that decayed into the atomic $^2P_{3/2}$ state. The first experiments using this technique had 500 $Torr$ of Argon and 100 $Torr$ of ethane in Cs-Ar-C_2H_6 mixtures [35, 36, 38]. It was reported that this pumping mechanism produced broad spectral linewidths ($\gtrapprox 5\ nm$), and slope efficiencies approaching 10% with absorbed pump energy thresholds of $\approx 40\ \mu J$. This was first done using a pulsed dye laser, driven by the second harmonic of an Nd:YAG system generating $4-5\ ns$ FWHM pulses. With pump energies as large as 6 mJ, the dye laser has a pulse rep rate and nominal linewidth of 10 Hz and $\approx 0.2\ cm^{-2}$ respectively. The alkali cell used in their experiment was made of quartz, had brewster angles and had dimensions of 6.0 cm in length and 2.5 cm in diameter. This XPAL system used five levels to generate the 894.3 nm (the Cs D_1 line) lasing line. The first two of the five levels are the ground and excited states of the Cs-Ar excimer, and the final three levels are the typical three laser levels of the Cs DPAL. In essence, this version of the XPAL simply found a new way to populate the $6^2P_{3/2}$ state in Cs. A temperature of 435^oK was maintained in

these early studies.

In 2009, Readle et al. performed a similar analysis using krypton instead of argon [34]. This time the Nd:YAG pumped dye laser was tuned to 841 nm to pump the blue satellite peak of the Cs-Kr excimer. The Cs-Kr was contained in a Pyrex cell with plane-parallel windows, having a length of 10 cm and diameter of 2.5 cm. The cell contained 500 $Torr$ of Kr and 100 $Torr$ of C_2H_6. The emitted laser energy was detected by calibrated pyroelectric detectors. Three temperatures were used in this experiment, 374 K, 443 K and 468 K. The spectral breadth of the excitation spectrum blue satellite was $\gtrapprox 2$ nm. This is smaller than the Cs-Ar blue satellite, but still 85 times larger than the typical Cs D_2 line in the DPAL system. It was found that parasitic lasing, due to the plane parallel windows, contributed to a decrease in laser performance for larger alkali densities. Three temperatures and their corresponding thresholds were reported; 40 μJ at 444 K (similar to the previous study), 85 μJ at 458 K and 140 μJ at 468 K. It was expected and reported that both the threshold increased and the slope efficiency decreased with increasing alkali number densities.

In 2010, Readle et al. changed two major aspects of the operation of the XPAL system. First they (which caused both changes to occur simultaneously) removed the hydrocarbon from the equation. This was done because of the degrading effect hydrocarbons has on lasing mediums. In addition to a very narrow spectral pump bandwidth, the typical DPAL system suffers from a very significant degradation in laser performance over a short period of time due to the breaking down of the hydrocarbon in the alkali cell. The breaking down of the hydrocarbon creates a "soot" in the lasing medium and drastically increases the loss. By removing the hydrocarbon, population inversion occurs at the $^2P_{3/2}$ state, allowing this particular XPAL to operate in a 4-level system. Test cells containing Cs-Ar and Cs-Ar-Kr mixtures were explored. Like previous studies, 500 $Torr$ of alkali were used in both test cells. In

the case of the Cs-Ar-Kr cell, equal parts of each rare gas were used until 500 $Torr$ was reached. The same Nd:YAG pumped dye laser was used as the pump source and the test cell was 10 cm in length. The breadth of the excitation spectrum decreased slightly from the Cs-Ar-C_2H_6 mixture to $\gtrapprox 3\ nm$. It was also noted here that the spectral width narrows slightly at higher alkali concentrations. Surprisingly the threshold absorbed pump pulse energy at 464 K was $\approx$ 130 μJ, which was very close to the threshold value of the Cs-Kr-C_2H_6 laser at comparable temperature. As in the last study, three temperatures along with their thresholds were reported for the Cs-Ar 4-level system; 130 μJ at 464 K (similar to the 468 K case in previous study), 175 μJ at 475 K and 250 μJ at 485 K. It was noted that although the Cs-Ar-Kr mixture had the same spectral blue satellite width and peak, and nearly identical absorbed pump energy threshold conditions, that the benefit comes by reducing the D_2 laser pump energy threshold significantly (as much as 28%).

In 2011, Palla et al. presented an XPAL model and theory at an SPIE conference [4]. A BLAZE-V model was modified to model the 4-level XPAL system for Cs-Ar pairs. The model was validated against the data taken in the previously reported studies by Readle and then extended to predict the performance for a Rb-Kr mixture. The model suggested that the Rb-Kr variant should have significantly lower required pump intensities than the Cs-Ar cousin.

In 2012, Hewitt et al. used the Cs-Ar 4-level XPAL to explore the effect photoionization has on the dynamics of the laser operations when using pump intensities of up to 3 $\frac{MW}{cm^2}$ [33]. Approximately 500 $Torr$ of argon was used in a 10 cm in length borosilicate cell. Six cell temperatures in the range of 433 to 534 K was analyzed. The following non-linear process was used to determine how significant a role two-photon ionization plays in XPAL kinetics.

$$Cs(6p^2P_{3/2}) + 2\hbar\omega \xrightarrow{\sigma^{(2)}} Cs^+(^1S_0) + e^- + \Delta E \tag{4}$$

Where ΔE is the energy beyond that required for two 836.7 nm to ionize the atom. For a 474 K case, the two-photon ionization cross-section was calculated to be no larger than 8×10^{-26} $\frac{cm^4}{W}$ and therefore determined that photoionization plays only a minor role in the laser process of the XPAL even at these high pump intensities.

This work will continue the investigation of the XPAL by demonstrating performance of the Rb-Ar and Rb-Kr 4-level system in a heat pipe. A heat pipe allows testing the performance at high temperatures and high pressures.

III. The Two-Photon Absorption (TPA) Cross-Section for the $5^2S_{1/2} \longrightarrow 5^2D_{5/2}$ Transition in Naturally Occurring Rb

3.1 Introduction

A new class of diode pumped lasers based on excitation of the D_2 line and subsequent lasing on the D_1 line in alkali atoms is receiving considerable attention [65]. The Diode Pumped Alkali Laser (DPAL) typically requires: (1) high buffer gas pressures, > 1 atmosphere, to match the width of the absorption profile to the spectral lineshape of the diode pump source, and (2) a collision partner such as ethane at pressures of several hundred Torr to relax the population in the pumped $^2P_{3/2}$ to the upper laser $^2P_{1/2}$. The alkali atoms provide high absorption even at low concentration and a single atom may rapidly cycle under intense pump conditions, at rates exceeding 10^{10} $\frac{cycles}{s}$, suggesting high power operation from a small gain volume.

Several additional schemes for optically pumping alkali metals to achieve lasing in the infrared and blue have been developed over the past 40 years [1, 5, 6, 7, 39, 55, 59, 63]. More recently, stimulated emission on the blue $^2P -^2 S$ transitions in Rb and Cs has been achieved by pumping at a single wavelength in the red via two-photon absorption [16]. The $5^2D_{3/2}, 5^2D_{5/2}$, and $7^2S_{1/2}$ states of rubidium and the $7^2D_{3/2}, 7^2D_{5/2}$, and $9^2S_{1/2}$ states of cesium were populated at low pressure by two-photon excitation using a pulsed dye laser. The transition probability for this two-photon transition from the initial ground state $|i\rangle$, or $5^2S_{1/2}$, to the final state $|f\rangle$, or $^25D_{5/2}$, proceeds through a virtual intermediate state $|v\rangle$ as shown in Figure 7. The pump wavelength is $12,851.749\ cm^{-1}$, which is $35.204\ cm^{-1}$ to the blue of the D_2 line. The slope efficiency of 0.5% in Rb is considerably higher than achieved in the prior sequential double resonance experiments [63] and requires only a single wavelength pump source. Cascade lasing on the infrared transition followed by the

blue transition offers no quantum defect and the potential for low heat loads. There would also be no need for a spin-orbit coupling gas, such as ethane, which has caused soot buildup problems in traditional DPAL cells at high temperature [57]. We refer to this blue laser as the Two-photon Pumped Alkali Laser (TPAL).

The blue TPAL is also an example of a rapid non-linear optical process that can populate higher lying states in the alkali atom. This is of interest to the DPAL community when high pump intensities are used. Emission from the second excited P states, and from more than 30 lines including states near ionization have been observed by Jones et al. [41]. If the ionization rate becomes too large, the situation could impose a limit to intensity scaling.

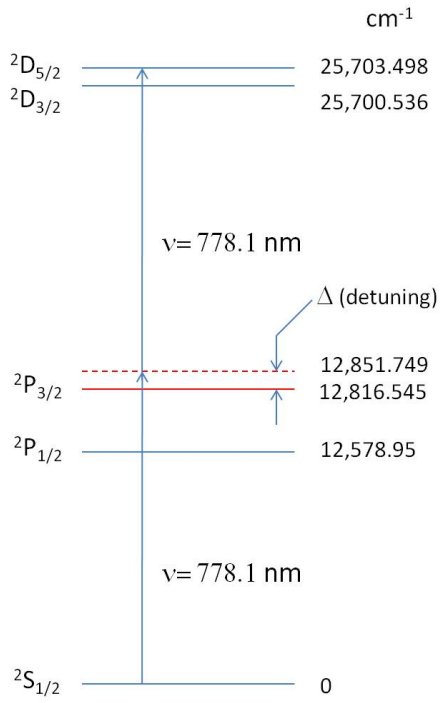

Figure 7. The two-photon absorption cross-section was calculated for this particular transition in Rb.

Few groups have modeled or measured the absorption cross-section for the $5^2S_{1/2} \longrightarrow 5^2D_{5/2}$ transition in Rb. Zapka et al. used Doppler-free, frequency-modulation (FM) spectroscopy to generate the absorption spectra in Rb vapor in 1983 [67]. They

focused a 60 mW single-mode cw dye laser to a beam waist of 70 μm in a ^{87}Rb vapor of 3.3×10^{14} cm^{-3} and observed an absorption of 2.5%. A TPA cross-section $\sigma_{2\phi} = 4 \times 10^{-20}$ $\frac{cm^4}{W}$ for the $5^2S_{1/2}(F = 2) \longrightarrow 5^2D_{5/2}(F = 4)$ hyperfine line in ^{87}Rb was reported.

Collins used Doppler free, differential absorption spectroscopy (DAS) [19] with an external-grating-cavity cw diode laser with $100\frac{W}{cm^2}$ to tune through the $5^2S_{1/2}(F = 2) \longrightarrow 5^2D_{5/2}(F = 0, 1, 2, 3, 4)$ transitions of ^{85}Rb in a 2.54 cm long Pyrex cell containing a ^{85}Rb number density of 6.8×10^{-18} cm^{-3}. Five Gaussians were fit to the weak absorption signals ($\alpha \propto 10^{-6}$) corresponding to the five hyperfine lines to determine a two-photon absorption cross-section for the $5^2S_{1/2} \longrightarrow 5^2D_{5/2}$ transition of $\sigma_{2\phi} = 1.2 \times 10^{-18}$ $\frac{cm^4}{W}$, was two orders of magnitude larger than Zapka's report. In 1994, a theoretical value for the TPA cross-section was calculated (0.57×10^{-18} $\frac{W}{cm^2}$) using reduced absorption rates [49]. Most recently, TPA cross-sections were measured using low powers (1 mW) and low densities in a hollow-core photonic-band-gap fiber (PBGFs) filled with Rb vapor [43]. In this research PBGFs were demonstrated to enhance the light-matter interaction for ultralow powers, mitigating the need for focused beams and high powers. A 1% absorption was determined by detecting 30 nW of output blue flourescence at 420.3 nm with a 1 mW diode pump laser. With this method a direct absorption value was calculated to be 5×10^{-20} $\frac{cm^4}{W}$ for the $5^2S_{1/2} \longrightarrow 5^2D_{5/2}$ in ^{85}Rb.

There has not been any consistency in the values across the four previous groups. Therefore, a more comprehensive study is required to better understand the true value. However, generating the needed high intensity is problematic. Bamford et al. reported a technique using pulsed lasers for determining the two-photon absorption cross-section in atomic oxygen [20]. Peak intensities of 1.8 $\frac{MW}{cm^2}$ were achieved, but a careful determination of both the spatial and temporal profiles was required to

accurately extract a cross-section. Modeling the temporal profile is also cumbersome since the run-to-run variation of the intensity profile is high. Therefore our research chose to use a focused cw approach that varied the Rb number density from $1.61 - 8.52 \times 10^{15} cm^{-3}$, ranged pump powers from $0.32 - 0.99\ W$ (actual power measured at test cell) and used two focal length lenses, 15.24 cm and 20.32 cm, to generate 87 test configurations. It was necessary to develop a model of the spatial profile for the intensity to properly interpret the data. This model consists of a linear combination of the two-photon Beer's Law variant and a Gaussian propagation term to account for the focused beam. The statistical average of the 87 TPA cross-sections for the $5^2S_{1/2} \longrightarrow 5^2D_{5/2}$ transition in naturally occurring Rb will provide a confident value to be used to support work in examining the pump rate for a TPAL system.

3.2 Experimental

Figure 8 illustrates the major elements of the experimental set-up. Although a 2.5 W Sirah Matisse cw Ti:sapphire ring laser was used as the pump source the max output power did not exceed 1.2 W. The Matisse stabilized the output power as it scanned in frequency by $10-15\ GHz$ using a Pound-Drever-Hall waveform technique. Typical scan rates were set at 50 $\frac{MHz}{s}$. About 1% of the power was sent to a HighFinesse WS/7 High Precision wavemeter to determine the frequency to within 60 MHz accuracy on a 300 THz scale. The beam then passed through a mechanical chopper at 2 kHz frequency and then to a high reflector (M1). Another 1% of the beam power is used to monitor the incident power and transmission through a 300 MHz etalon, while the remaining energy is sent through a lens to focus the beam into the alkali test cell. As depicted in Figure 8, two Thor Lab PDA55 photodiodes were used to monitor the incident and transmitted power. After exiting the test cell the beam passed through a nuetral density filter wheel, OD = 0.1-5.0, to prevent detector satu-

ration. The signals from the two detectors, D_1 and D_2, and the etalon each were sent through their own Stanford Research System SR850 lock-in preamplifier triggered by the chopper wheel. Integration times of up to 1 s were used. The raw modulated signals were maintained and packaged into LabView files via a National Instruments USB-6212 BNC multifunction data acquisition (DAQ) module capable of 400 $\frac{kS}{s}$.

The alkali pyrex cell was 15 cm in length and was fixed to a gas handling and vacuum system with an ultimate vacuum of 29 $mTorr$. The alkali cell was enclosed inside a metal oven. The temperature of the oven was kept at about 10 degrees hotter than the finger containing the solid alkali to prevent condensing on the windows. Three temperature zones were controlled and monitored by an Omega Engineering temperature controller. The first two zones are along the length of the test cell (opposite ends) and the third on the finger protruding under the center of the cell.

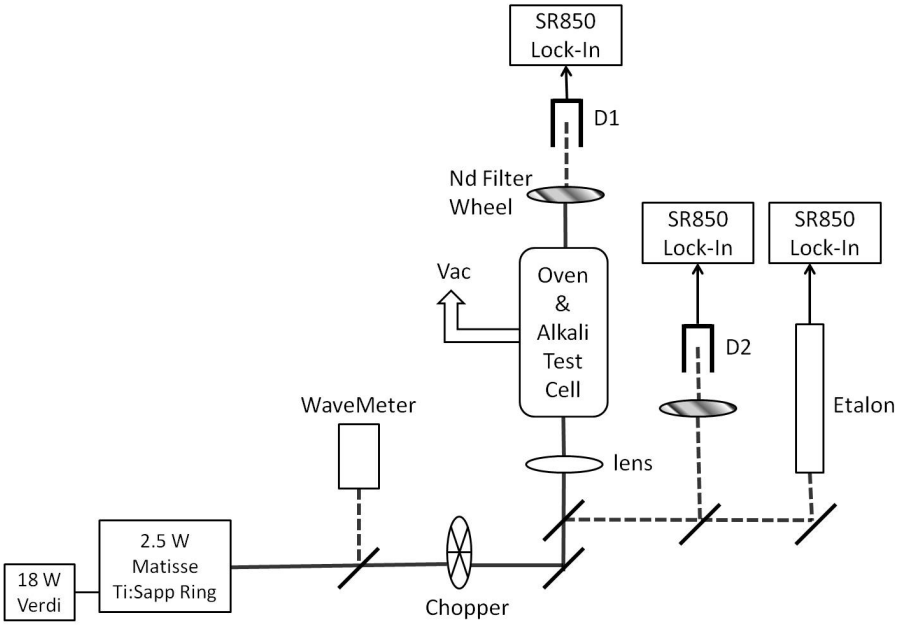

Figure 8. Two-photon cw laser absorption apparatus.

A 300 MHz Coherent Laser Spectrum Analyzer was used to assist in determining the laser frequency. We self calibrated the free spectral range (FSR) at 302.5 MHz using the hyperfine structure of the ground state in Rb.

The power just inside the test cell was measured by placing a Coherent LabMax-TO power meter via the LM-3 HTD power sensor in the optical beam train where the alkali test cell would normally be. An exact replica of the 1" Pyrex glass window was added into this beam train to simulate the the power entering the absorption medium. Transmission issues were encountered in the test cell when operating at temperatures from 280 ^oC to 320 ^oC. Liquid droplets of alkali were observed raining down from the neck to the test cell. This disturbance started to become noticeable at 280 ^oC and quite dominant at temperatures above 300 ^oC. Therefore, all of the TPA scans used in this research were between 230 and 280 ^oC. These temperatures were measured by monitoring the finger temperature of the alkali with an RTD and the Omega Temperature Controller. Since the vapor pressure is very sensitive to the temperature of the alkali finger, care was given to understanding the concentration of the alkali vapor inside the test cell.

Absorption in the wings of the optically thick D_2 transition was used to monitor the Rb concentration. Figure 9 illustrates an example spectrum. The data is represented in blue, while the red line is the model. The first peak contains the three transitions of $5^2S_{1/2}(F''=1) \longrightarrow 5^2P_{3/2}(F'=0)$, $5^2S_{1/2}(F''=1) \longrightarrow 5^2P_{3/2}(F'=1)$ and $5^2S_{1/2}(F''=1) \longrightarrow 5^2P_{3/2}(F'=2)$ of ^{87}Rb. At 85 ^0C, the peak absorbance is very large ($A > 22$). A fit of the full Voigt broadened hyperfine spectra is used to determine the Rb concentration.

$$A = -ln\left(\frac{I}{I_0}\right) = G(\nu, \nu_{F''\rightarrow F'})\left(\frac{g_{J'}}{g_{J"}}\right)\left(\frac{\lambda^2}{8\pi}\right)A_{fi}NL \tag{5}$$

where $G(\nu, \nu_{F''\rightarrow F'}) = \sum_{F'}\sum_{F''}\sum_{iso} g_V(\nu, \nu_{F''\rightarrow F'})S_{F''F'}f_B f_{iso}$ is the hyperfine lineshape function that accounts for the hyperfine transitions $F'' \rightarrow F'$, $S_{F''F'}$ are the line strengths, f_B is the Boltzmann factor, f_{ISO} is the isotopic factor, g_J is the degeneracy, and L is the length of the test cell. Between the two isotopes, there are 12 allowed

hyperfine transitions. The model constrains the known spacing and the relative amplitudes of each hyperfine component. These amplitudes were calculated from the line strengths, $S_{F''F'}$, the Boltzmann factor, $f_B(F'')$, and the isotopic fraction, f_{iso}. Seven parameters were allowed to float; the total Rb concentration, the frequency of the first line, the Doppler width, and 4 parameters for the cubic baseline. In Figures 9 the temperature was measured by the RTD as 85 ^0C, with a pressure that measured at 34 $\mu Torr$.

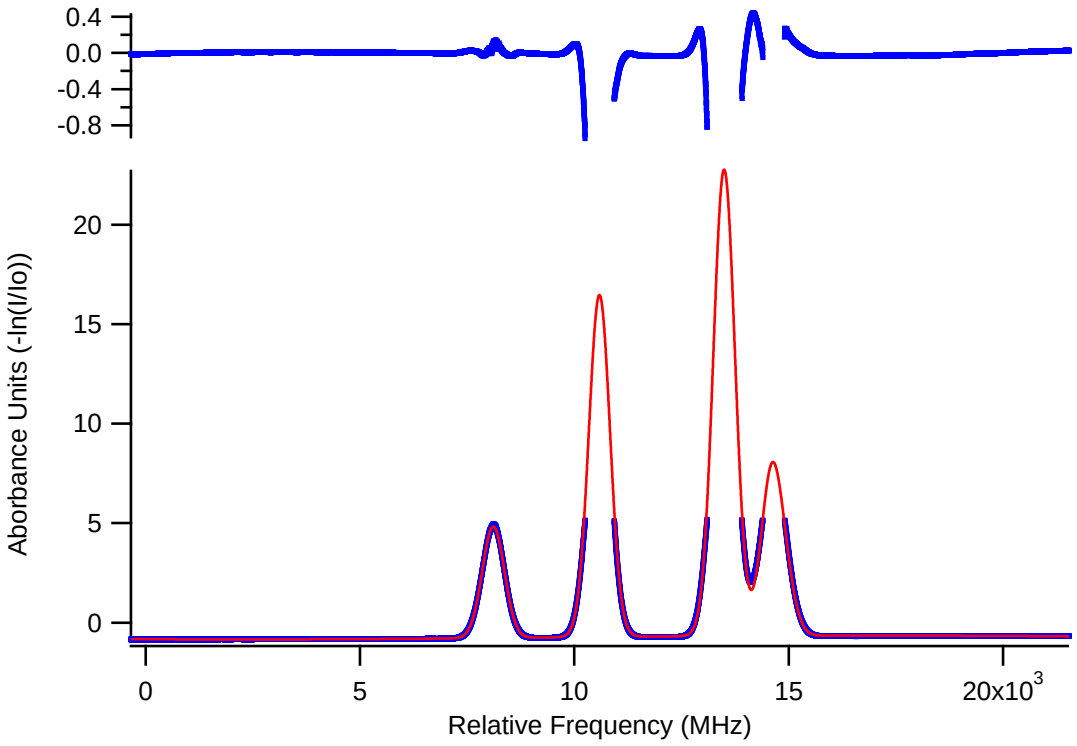

Figure 9. The entire D_2 transition is centered at approximately 384.230 THz. Although the intensity was kept below I_{Sat}, the high temperature caused absorbances to exceed the dynamic range of the SR850 lock-in. The pressure and temperature for this run were measured at 39.1 $mTorr$ and 85 ^oC respectively. The blue line refers to the actual data collected and the red is the Voigt model fitted to the transition.

The spectroscopically determined Rb vapor pressures are compared with a known vapor pressure curve (dotted line) [62] in Figure 10. A curve, using the same parameters from the established vapor pressure curve, was shifted in temperature to overlay our data. This shift in temperature (shown in Figure 10) amounted to about

14 $\pm 0.5\ ^oC$ cooler than measured at the walls of our alkali test cell. The 0.5 ^oC uncertainty in temperature corresponds to an 11% change in alkali concentration.

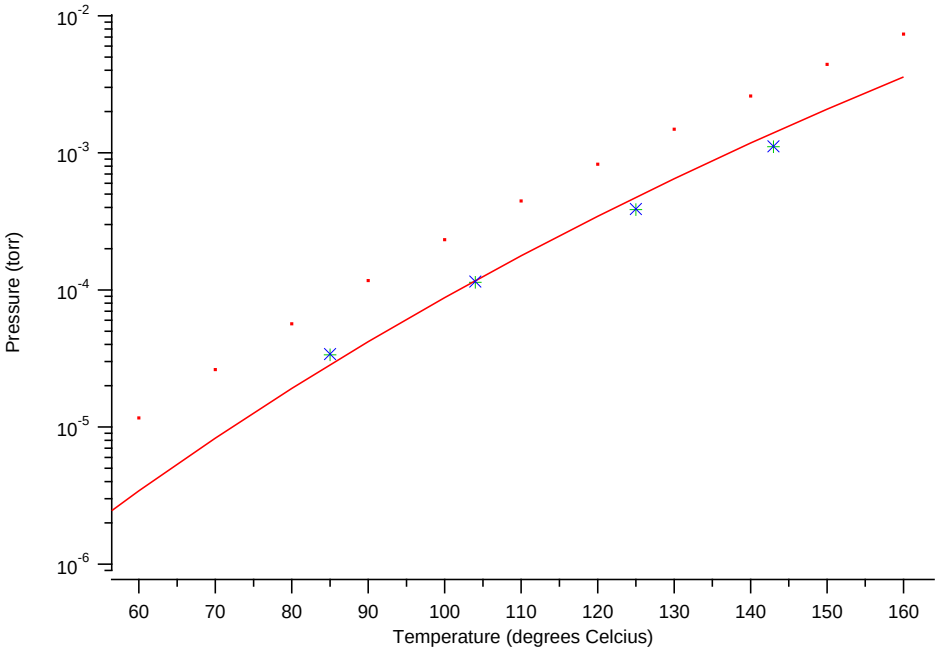

Figure 10. The vapor pressure calibration curve. The temperature inside the alkali test cell was approximately 14 ^oC **cooler than measured on the wall of the cell.**

The beam quality, or M^2, of the laser beam was measured using a ModeMaster by Coherent. A range of powers were used from 1090 mW to 1320 mW (measured at the pump laser aperture), to understand the power dependence on beam quality. A filter wheel would have affected the quality of the beam and was not used. Instead, the pump beam to the Ti:sapphire was adjusted. Referring to Figure 8, M^2 was measured at the location of the alkali test cell. It was observed that over this power range the beam quality stayed fairly consistent, from $1.05 - 1.09\ \pm 0.03$. We chose $M^2 = 1.09$ to be conservative while calculating the final number for $\sigma_{2\phi}$.

A ModeMaster was again placed in the beam train where the test cell would normally be, minus the lens. At 1200 mW the ModeMaster measured both the external beam waist, $\omega_{ext} = 0.547\ mm$, and the distance between the external waist to the ModeMaster position, $z_1 = 60\ cm$. These quantities allowed us to calculate

the beam waist at the focus;

$$\left(\frac{1}{\omega_f}\right)^2 = \frac{1}{\omega_{ext}^2}\left(1-\frac{z_1}{f}\right)^2 + \left(\frac{\pi\omega_{ext}}{f\lambda M^2}\right)^2 \tag{6}$$

Two lenses were used (15.24 cm and 20.32 cm) to investigate the veracity of this work's ability to extract a consistent TPA cross-section number, regardless of a change in intensity due to the beam waist. These lenses were inserted into the beam train such that the focus landed at the center of the alkali test cell. This was done for symmetry purposes that will become clear during the development of the "Governing Equation" which modeled a focused Gaussian beam propagating through a two-photon absorption medium.

3.3 Results

The cw laser absorption spectrum for the $5^2S_{1/2} \longrightarrow 5^2D_{5/2}$ two-photon transition for an intensity at the waist of $I = 3.1\ \frac{kW}{cm^2}$, Rb concentration of $N = 4.07\times10^{15}\ \frac{atoms}{cm^3}$, and the test cell path length of $L = 15\ cm$ is shown in Figure 11.

For a collimated beam, the transmitted intensity decays with propagation distance, z, as:

$$\frac{dI}{dz} = -\sigma_{2\phi}I^2N \tag{7}$$

$$\frac{I_0}{I(L)} - 1 = \sigma_{2\phi}NI_0L = A \tag{8}$$

where $\sigma_{2\phi}$ is the two-photon absorption cross-section ($\frac{cm^4}{W}$) and L is the propagation distance in the context of the length of the test cell. For a focused beam, the I_0 factor in the absorbance might be best interpreted as a weighted average of the intensity. A more complete development of the spatial dependence of the intensity

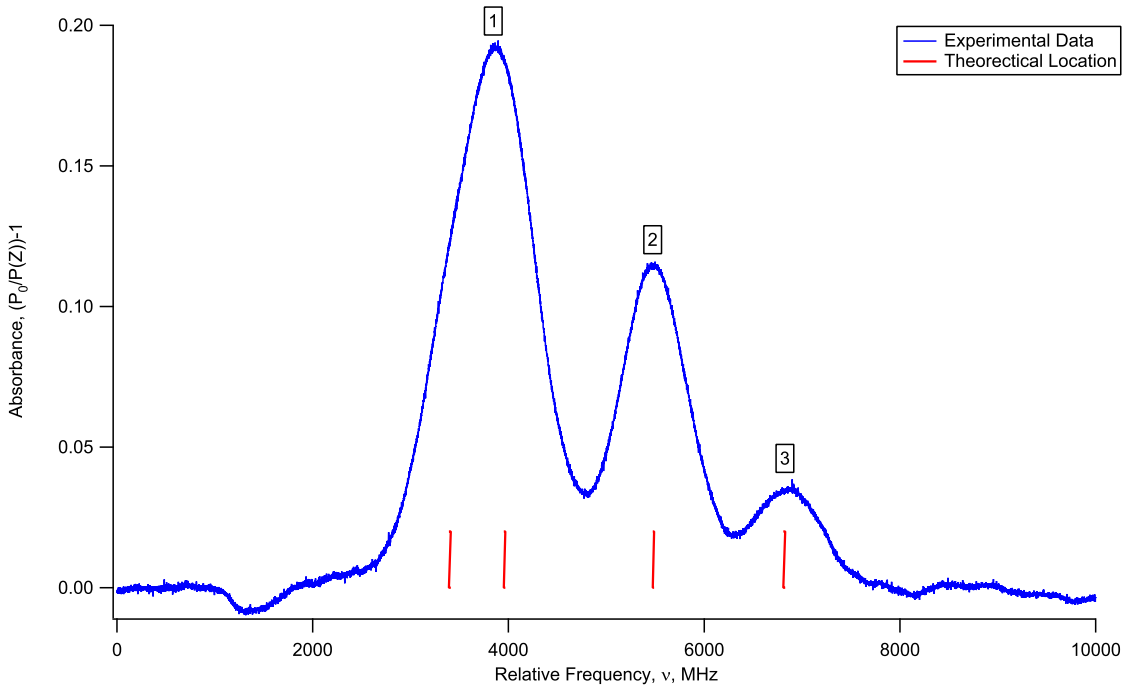

Figure 11. A typical spectra collected in this experiment. Peak (1) includes hyperfine transitions of two isotopes. Peak (2) was used throughout this study to measure the TPA cross-section due to it's independence from other isotopes and relative strength compared to Peak (3). The beam waist was calculated to be $69.7\ \mu m$**. The vertical lines refer to the theoretical positions of the hyper-fine splittings of the ground state of each Rb isotope. The outer two lines are** ^{87}Rb **and the inner two are** ^{85}RB**.**

will be developed below. Integrating the intensity over the detector area yields a signal proportional to the power, P, as presented in Figure 11. A peak absorbance of $A = 0.19$ is observed. The baseline noise is $\approx A = 0.002$, with a longer term baseline variance of up to 0.01.

The hyperfine splitting of the ground $5^2S_{1/2}$ state is ≈ 3.036 and $6.834\ GHz$ for the ^{85}Rb and ^{87}Rb isotopes respectively [62]. The hyperfine splittings for the upper $5^2D_{5/2}$ are smaller than the Doppler width, $2.9 - 9.4$ and $15.9 - 28.8\ MHz$, and unresolved (refer to Figure 12) [3]. The less abundant (27.83%) ^{87}Rb isotope with the larger ground state hyperfine splitting has 7, $F = 2, 1, 0$ allowed transitions in two groups. The more abundant (72.17%) ^{85}Rb isotope with the smaller hyperfine splitting has 10 allowed transitions, with one of the two groups convolved with the

low frequency component for ^{87}Rb. The isotopic shift is small, $\approx 78\ MHz$ [62]. The frequency differences observed in Figure 11 are reduced by a factor of two, due to the two-photon transition.

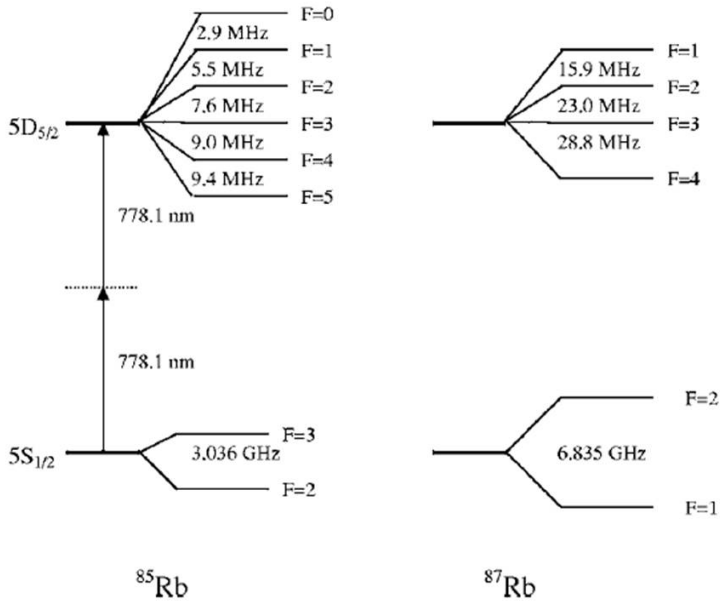

Figure 12. The hyperfine splittings for both isotopes [3].

We chose to report values from the $5^2S_{1/2}(F" = 2) \longrightarrow 5^2D_{5/2}(F' = 0, 1, 2, 3, 4)$ transition in ^{85}Rb due to its signal strength and independence from the other isotope. This transition is labeled as Peak #2 in Figure 11. With the absorbance of this peak equal to be 0.115, we calculate the effective "one-photon" cross-section to be $(\sigma_{2\phi}\ I_0) \approx 1.88 \times 10^{-18}\ cm^2$ from Equation 8. The difficulty, and the focus of this research, is determining with accuracy the intensity through the alkali cell such that the TPA cross-section can be extracted. To do this, both a spatial model of the intensity propagating through the alkali cell and a lineshape model are required.

It is important to understand the TPA cross-section number in the context of the lineshape, because the absorption cross-section is directly proportional to the lineshape. The lineshape model in this experiment consists of a determination of the Boltzmann and isotropic factors, the two-photon signal strengths, the frequency

Table 2. The calculated signal strengths for 85 rubidium where $I = \frac{5}{2}$.

F" \ F'	0	1	2	3	4	5
2	1/36	7/90	1/9	7/60	1/12	0
3	0	1/180	1/36	7/90	1/6	11/36

spacing and a lineshape function. For this transition, two Boltzmann factors were calculated, one for each of the two hyperfine lines of the ground state (F''). These two values were calculated to be $f_{B(F''=2)} = 0.417$ and $f_{B(F''=3)} = 0.583$. The isotopic ratios are, $f_{iso\ ^{85}Rb} = 0.7217$ and $f_{iso\ ^{87}Rb} = 0.2784$. The 17 relative signal strengths, $S_{F''F'}$, for a two-photon transition were calculated using the following equation [24],

$$S_{F",F'} = \frac{(2F"+1)(2F'+1)\begin{Bmatrix} J' & 2 & J" \\ F" & I & F' \end{Bmatrix}^2}{(2I+1)}, \tag{9}$$

Tables 2 and 3 list the 17 signal strengths calculated from Equation 9. Finally, the frequency separation was determined from data provided by both Steck and Olsen [3, 62]. Figure 11 shows the theoretical line spacings, however the F spacings are unresolvable on that scale. We chose an area normalized Voigt function to model the absorption lineshapes due to the need to model the Doppler and homogeneous linewidth. We discovered that there was no preferred function used to model a two-photon transition from previous studies [2, 10, 19, 21, 43, 45]. Although we used a Voigt function, the Doppler width is approximately 100 times larger than the homogeneous width, so the Gaussian lineshape is dominant.

Before applying a lineshape model to the data in Figure 11, a non-linear transformation of the y-axis from absorbance units to cross-section units is performed. A full interpretation of the spectra to determine a best estimate of the two-photon cross-

Table 3. The calculated signal strengths for 87 rubidium where $I = \frac{3}{2}$.

F' / F"	1	2	3	4
1	9/80	7/48	7/60	0
2	1/80	1/16	7/40	3/8

section requires an analysis of the focused beam propagation. Figure 13 illustrates the intensity propagation for a focused beam.

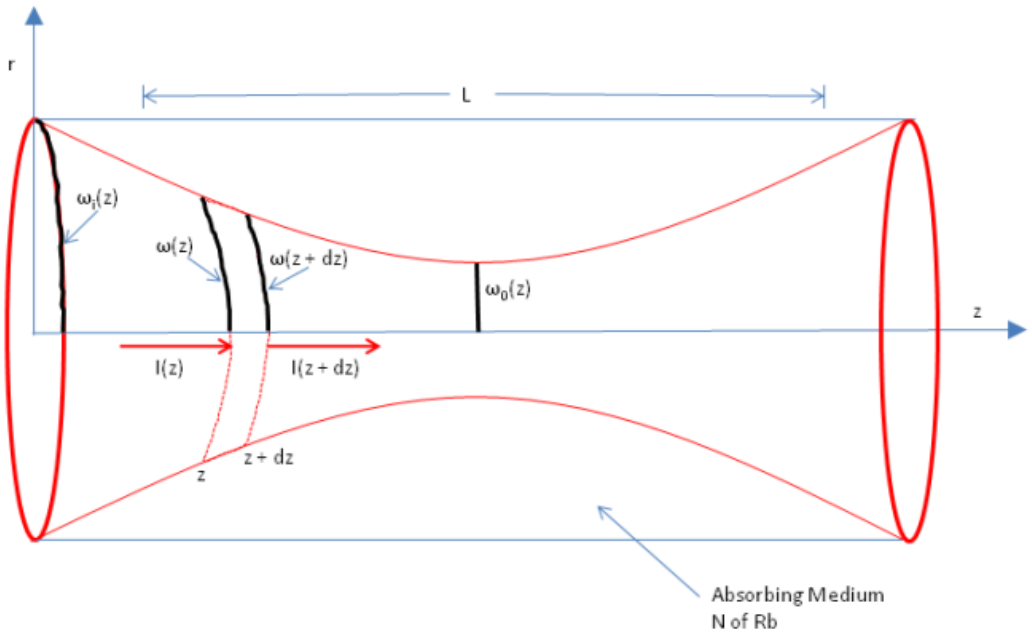

Figure 13. The laser beam passes through a focus as it travels through the Rb Vapor. An accurate calculation of the TPA cross-section requires a model of I(z).

In differential form, this propagation is modeled by the following equation,

$$\frac{dI}{dz} = -\sigma N I^2 + F(z)I \tag{10}$$

where the Gaussian beam propagation term is:

$$F(z) = \frac{2}{\omega(z)}\left(\frac{r^2}{\omega^2(z)} - 1\right)\frac{d\omega}{dz} \tag{11}$$

where,

$$\omega(z) = \omega_0^2 \left[1 + \alpha^2 (z - \frac{L}{2})^2\right] \tag{12}$$

and the parameters are define as:

$$\alpha = \frac{M^2 \lambda}{\pi \omega_0^2} \tag{13}$$

$$\omega_0 = beam\ waist = 69.7 - 94.4\ \mu m \tag{14}$$

$$M^2 = beam\ quality\ factor = 1.09 \tag{15}$$

The solution to Equation 10 follows from Bernoulli's approach, such that:

$$I(L) = I_0 \frac{e^{[I_1(L) - I_1(0)]}}{1 + \sigma_{2\phi} N I_0 \left[I_2(L) - I_2(0)\right] e^{-I_1(0)}} \tag{16}$$

where

$$I_1(L) = \int \frac{2\alpha^2 (L - H)}{1 + \alpha^2 (L - H)^2} \left(\frac{r^2}{\omega_0^2 \left[1 + \alpha^2 (L - H)^2\right]} - 1 \right) dL \tag{17}$$

and,

$$I_2(L) = \int e^{I_1(L)} dL \tag{18}$$

Unfortunately, the integral I_2 is not analytic and a numerical approach is required. We choose to cast the solution in the form of Equation 8:

$$I(L) = \frac{I_0}{1 + \sigma_{2\phi} I_0 \eta(\alpha, r) N L} \tag{19}$$

where the longitudinally averaged intensity is developed from the factor:

$$\eta(\alpha, r) = \frac{1}{L}\left(\int_0^L \left[\frac{e^{-\frac{r^2}{\omega_0^2}\left(\frac{1}{1+\alpha^2(z-\frac{L}{2})^2}\right)}dz}{1+\alpha^2(z-\frac{L}{2})^2}\right]\right)(1+\frac{\alpha^2L^2}{4})e^{\frac{r^2}{\omega_0^2}\left(\frac{1}{1+\frac{\alpha^2L^2}{4}}\right)} \tag{20}$$

A more complete development of Equations 16−20 is found in Appendix A. The average intensity for two Gaussian beams is shown as a function of radial position in Figure 14. As the beam becomes more collimated, $\alpha \longrightarrow 0$, the solution becomes less sensitive to radial position and the solution of Equation 8 is recovered.

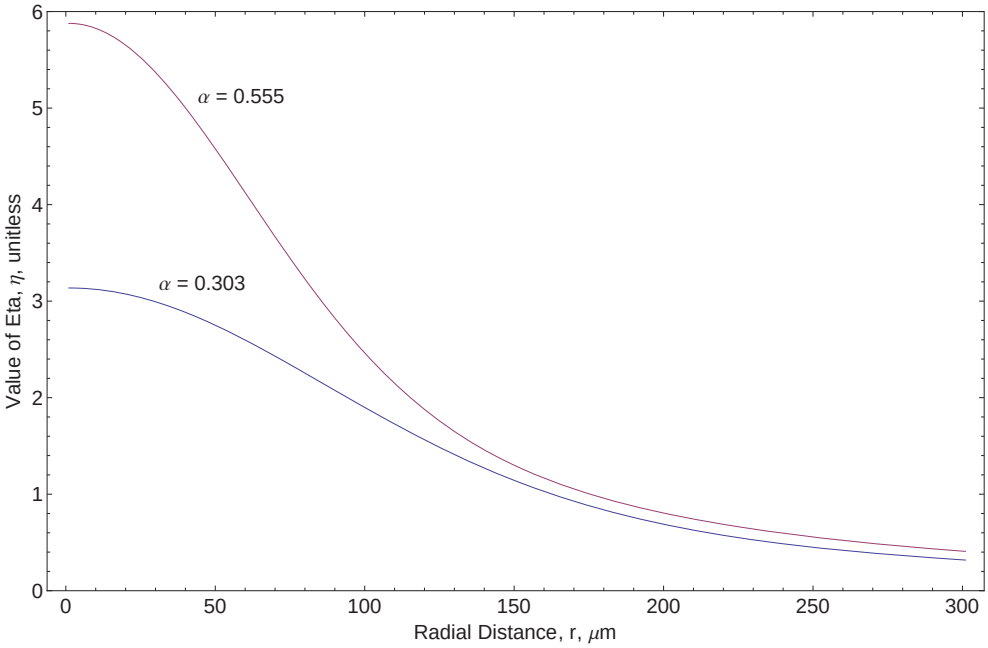

Figure 14. The intensity varies as a function of $\eta(r)$ in the radial direction. As the beam waists decreases, or $\alpha \to \infty$, the η function plays a more significant role in the intensity equation.

Figure 15 illustrates the longitudinal intensity distribution on axis for several TPA cross-sections. The first is an unattenuated case, or $\sigma = 0$, to set the baseline and contrast the effects of TPA. The next three are in powers of ten, $\sigma = 10^{-21}, 10^{-20}$ and 10^{-19}. The location of the peak intensity shifts to the left with increasing TPA cross-section. This suggests that the TPA term in Equation 10 dominates the focusing term for certain values of $\sigma_{2\phi}$.

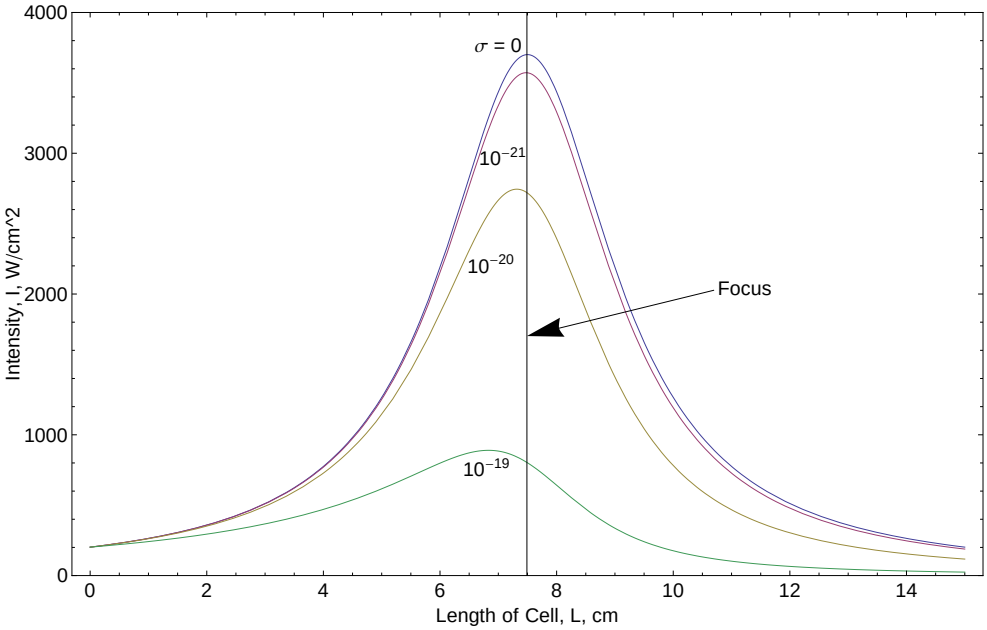

Figure 15. Using Equation 19, this plot depicts four intensity profiles corresponding to four different TPA cross-section values. Since the first value is zero, we find that the equation returns a symmetric Guassian as expected. Please note that as the cross-section increases, that the intensity at the end of the test cell ($L = 15\ cm$) decreases and the peak of the intensity profile increasingly shifts to the left of the focus.

Figure 16 illustrates three methods for modeling the absorbance value. The y-axis is the typical Beers Law relation for the absorbance, $-ln\frac{I}{I_0}$, where three methods have been fit to this form. The three methods represented on this plot are the One-Photon Beers Law (Equation 21), the two-photon Beers Law (Equation 22) and the two-photon Beers law with a focused Gaussian beam (Equation 23).

$$-ln\frac{I}{I_0} = \sigma_{2\phi} I_0 N L \tag{21}$$

$$-ln\frac{I}{I_0} = ln(1 + \sigma_{2\phi} I_0 N L) \tag{22}$$

$$-ln\frac{I}{I_0} = ln(1 + \sigma_{2\phi}\eta(\alpha, r) I_0 N L) \tag{23}$$

Each method is plotted against the two-photon absorbance, $A_{2\phi} = \sigma_{2\phi} I_0 N L$, along the x-axis. Comparing the One-Photon Beers Law (1) to the two-photon Beers Law

(2), we discover that as the absorbance increases, the One-Photon Beers Law overestimates the value for the TPA cross-section. Finally, we see in Figure 16 how the model for the two-photon Beers Law with a focused Gaussian beam (3) compares to the two-photon Beers Law (2) for two beam waists ($\alpha = 0.303$ and 0.555). Interestingly, for the smaller beam waist, both the One- and two-photon Beers Laws underestimate the value of the TPA cross-section for low values of absorbance and then overestimates by an increasing amount for larger values of absorbance. We see that for $\alpha = 0.555$, the two-photon Beers Law is a good approximation for $\sigma_{2\phi} I_o N L < 0.23$. Figure 16 also shows that for larger beam waists (*i.e.* $\alpha = 0.303$) and larger absorbance values, there is greater divergence between the two-photon Beers law model and the numerical model developed in this work. This divergence points to the need to properly model the pump beam going through a focus to more accurately predict the absorbance value for a given TPA cross-section.

A key step to developing a function that transforms absorbance data from Figure 11 to TPA cross-sectional units, is to first perform a radial integral to the intensity model shown in Figure 15 and Equation 19. This radial integral, solved numerically, illustrates the power transmitted through the alkali cell. This integral was solved multiple times for a given range of TPA cross-section values. Next, we calculate a two-photon absorbance value from the computed range of powers. Plotting these calculated absorbance values (i.e. the predicted absorbance) against the range of TPA cross-sections yields the curve in Figure **??**. A 4th-order polynomial is then fitted over this curve to extract the function that will convert (or transform) the absorbance values along the y-axis in Figure 11 to TPA cross-section values. This transformation was performed on all 87 test configurations.

After transforming the data in Figure 11, the y-axis now represents the absolute two-photon absorption cross-section which takes into account the hyperfine structure

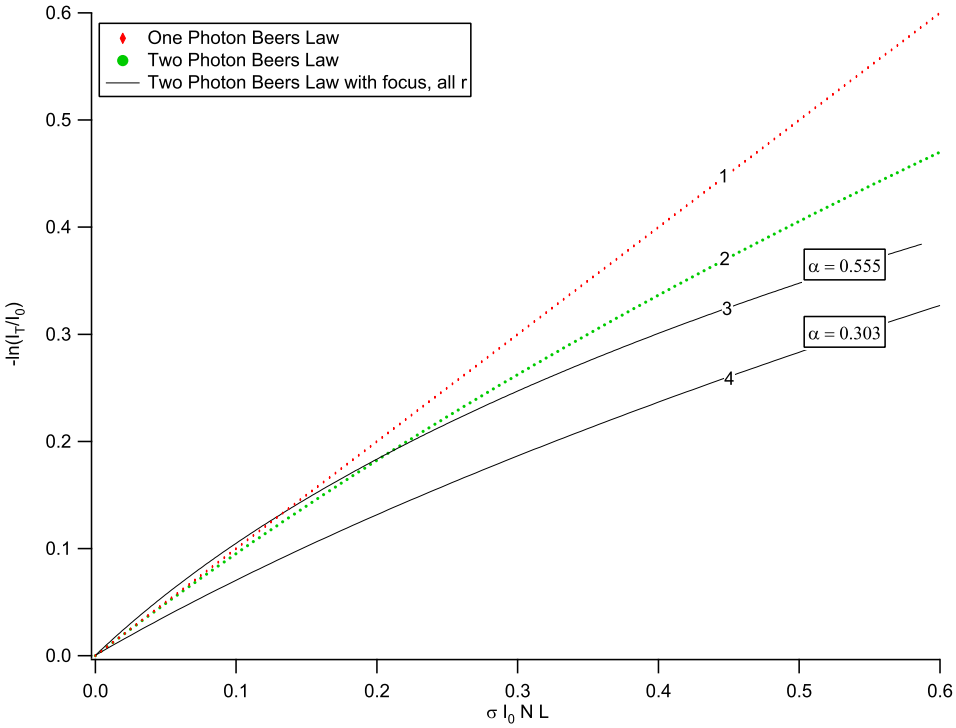

Figure 16. Three models for the intensity plotted against the two-photon absorbance. (1) Models the intensity using the one-photon Beers Law standard model. This model was baselined by forcing the other two models to equal $-ln\left(\frac{I}{I_0}\right)$ This is why this model appears as a perfect 45^o line. (2) This is the two-photon Beers law model. (3) and (4) are both the complete numerical method, taking into account the focused Gaussian beam and integrating over all of the radial length. Two curves appear because two different beam waists were used in this experiment. All 4 curves were generated from Equations 21 to 23.

of the transitions, $\sigma_{2\phi}^{HF}$. Using the following definition for the one-photon absolute absorption cross-section,

$$\sigma_{1\phi}(\nu) = \left(\frac{g_{J'}}{g_{J''}}\right)\frac{\lambda_p^2}{8\pi}A_{fi}g(\nu,\nu_{F''\rightarrow F'}) \tag{24}$$

the one-photon absolute cross-section that accounts for the hyperfine structure, $\sigma_{1\phi}^{HF}$, can be written using the hyperfine lineshape function defined in Equation 5,

$$\sigma_{1\phi}^{HF}(\nu) = \left(\frac{g_{J'}}{g_{J''}}\right)\frac{\lambda_p^2}{8\pi}A_{fi}G(\nu,\nu_{F''\rightarrow F'}) \tag{25}$$

Therefore, applying Equation 73 to Equation 25, the hyperfine cross-section in terms of the cross-section is now,

$$\sigma_{1\phi}^{HF}(\nu) = \sigma_{1\phi}(\nu)\frac{G(\nu, \nu_{F''\rightarrow F'})}{g(\nu, \nu_{F''\rightarrow F'})} \tag{26}$$

At line center, ν_0, Equation 26 can be further simplified to

$$\sigma_{1\phi}^{HF}(\nu_0) = \sigma_{1\phi}(\nu_0)\sum_{F'}\sum_{F''}\sum_{iso} S_{F''F'} f_B(F'') f_{iso} \tag{27}$$

Equation 74 is directly applied to the two-photon case by making the following substitutions, $\sigma_{1\phi}^{HF}(\nu_0) \longrightarrow \sigma_{2\phi}^{HF}(\nu_0)$ and $\sigma_{1\phi}(\nu_0) \longrightarrow \sigma_{2\phi}(\nu_0)$. A Voigt model (based on Equation 74) was developed to fit over the data collected in this experiment as shown in Figure 17. After the y-axis has been transformed to TPA units, the amplitude of the Voigt function in the model (at line center) yields the hyperfine cross-section, $\sigma_{2\phi}^{HF}(\nu_0)$. The hyperfine independent TPA cross-section at line center, $\sigma_{2\phi}(\nu_0)$, is being defined as

$$\sigma_{2\phi}(\nu_0) = \left(\frac{g_3}{g_1}\right)\frac{\lambda_p^4}{64\pi^2 h}\gamma_{fi}^{2\phi}\frac{g(\nu_0)}{\Delta^2} \tag{28}$$

Where λ_p is the pump wavelength ($\lambda_p = 778.104\ nm$), h is Planck's constant in $[J - s]$, Δ is the detuning of the virtual state from the $5^2P_{3/2}$ state in $[1/s]$ (as depicted in Figure 7) and $\gamma_{fi}^{2\phi}$ is an effective decay rate. Selection rules dictate this transition (D-S) is forbidden for a single photon, so this decay rate term does not describe a photon from the D-level decaying down to the ground state. It is rather a convenient collection of terms that include the two dipole moments (μ_{32} and μ_{21})

that significantly contribute to the transition,

$$\gamma_{fi}^{2\phi} = \frac{64}{3}\frac{\pi^4\nu_0^5}{\epsilon_0^2 c^6 h^2}\mu_{32}^2\mu_{21}^2 \tag{29}$$

With these terms defined, the y-axis transformed and the Voigt model developed, a final analysis is now done of the data. An example of this final fit is shown in Figure 17.

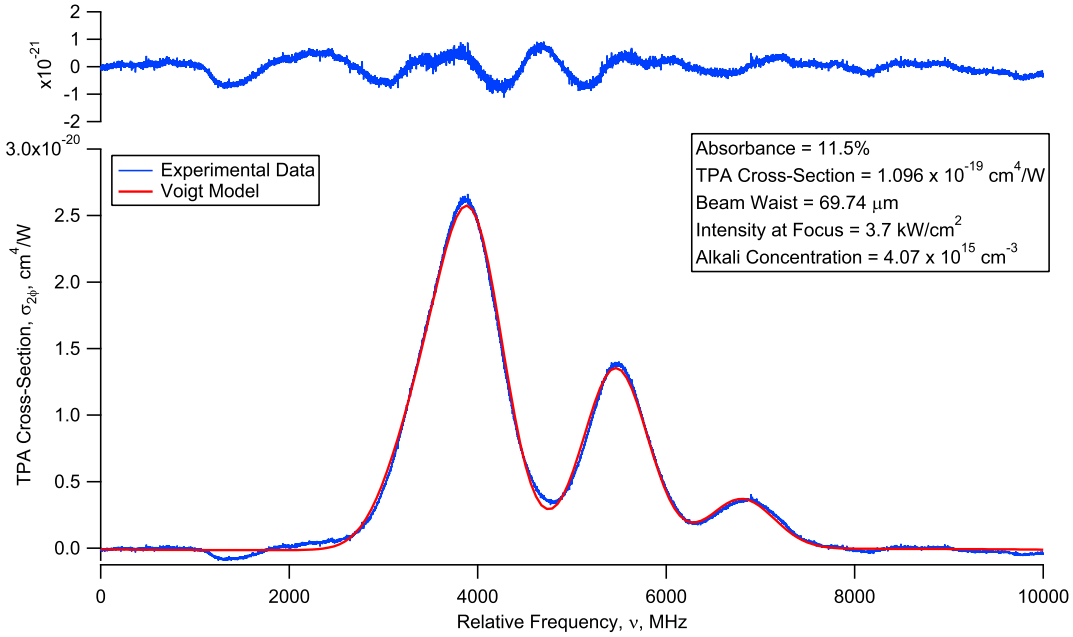

Figure 17. An example of the Voigt model fit over the TPA spectra. The amplitude of the Voight was extracted to determine the TPA cross-section.

This final fit was done on all 87 test configurations, allowing 87 TPA cross-sections to be extracted. These TPA cross-section values are displayed in Figure 18 and compared against two historical values, as well as the value calculated from Equation 74. This work reports an average experimental value for the hyperfine broadened TPA cross-section for the $5^2S_{1/2} \longrightarrow 5^2D_{5/2}$ transition in natural rubidium, weighted against the error of each test case, to be $6.75 \times 10^{-21}\ \frac{cm^4}{W}$. We also report a standard deviation of $3.61 \times 10^{-21}\ \frac{cm^4}{W}$. The theoretical value, which accounts for the dipole

transition moments (Equation 74) is 2.50×10^{-21} $\frac{cm^4}{W}$.

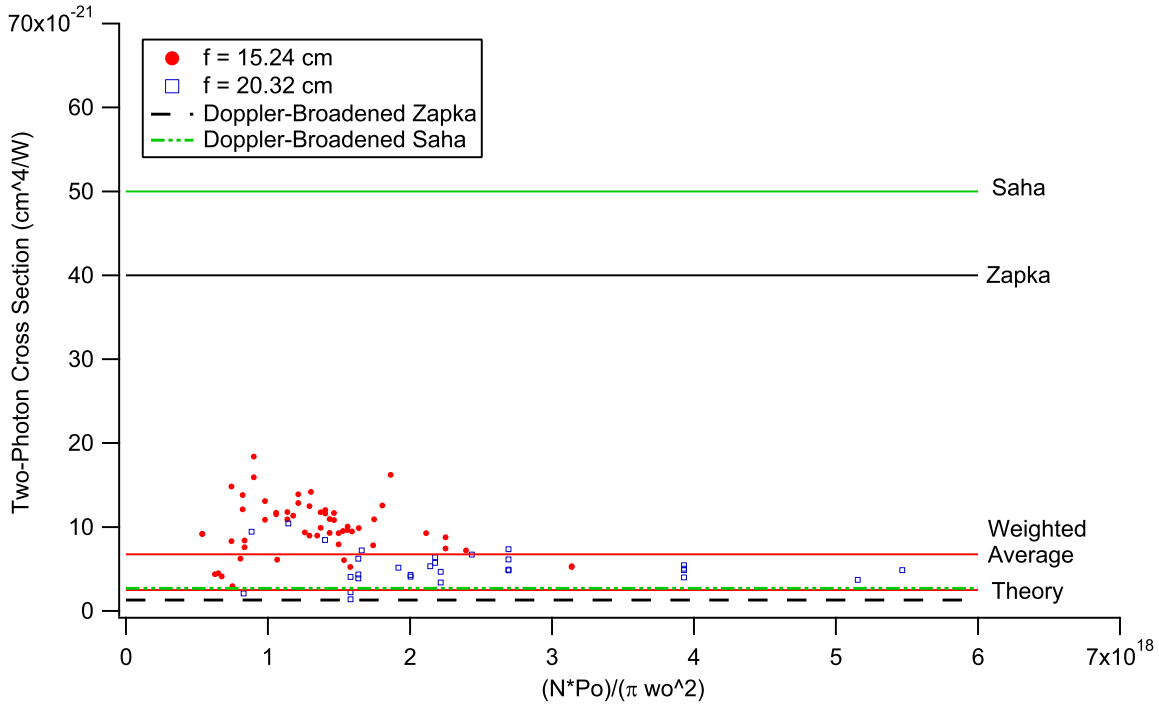

Figure 18. All 87 TPA cross-section values compared against historical values. Zapka et al. [67] and Saha et al. [43] are within a factor of 10 higher in cross-section, while Marinescu et al. ($\sigma_{2\phi} = 5.7 \times 10^{-17} \frac{cm^4}{W}$) [49] and Collins et al ($\sigma_{2\phi} = 1.2 \times 10^{-18} \frac{cm^4}{W}$) [19] are off the chart. Also displayed is the weighted average computed in this work, along with the value computed by the dipole moment dependent equation derived from theory (Equation 28).

3.4 Discussion

There are two main areas that contribute to significant error in our number. The first is the measurement of the alkali vapor pressure curve. It was determined that the true alkali concentration was $14 \pm 0.5\ ^oC$ cooler than what was measured by the RTD on the finger. We also chose to simplify the result by assuming no significant temperature gradients existed inside the alkali test cell. We felt that this was a reasonable approximation due to the small volume of the test cell. A second significant factor in the error of the final TPA cross-section value was the determination of the spot size. The primary method of measuring the beam size was to use a ModeMaster

to measure the beam size at the lens position, ω_{ext}, and the beam quality, M^2. The beam size was measured to an accuracy of $\pm$ 0.15 mm and the beam quality to within $\pm$ 0.4.

The numbers calculated in this experiment and the historical values must be compared only in the context of their respective lineshape functions. All previous experiments utilized sub-Doppler techniques to extract a TPA cross-section value. First of all, the values determined by Collins and Marinescu are greater than 8000$\times$ and 175$\times$ our reported value, respectively. Although it is difficult to know why these two groups differ so greatly, it is probable that the source of the error lies in the assumptions made for the intensity profile and the ability to know the alkali concentration. Collins et al. also did not do a direct absorption measurement of the transition. Curves generated from his work were collected from a side-viewing PMT, so an incomplete picture may have resulted from not being able to compare the initial to transmitted intensity properly. Marinescu's work centers the theory around reduced absorption rates. A completely divergent method from the rest of the studies. The values reported by Zapka and Saha are only 6$\times$ and 7$\times$ our reported value, respectively. We believe that the difference between the line widths, and ultimately the lineshapes, are what accounts for the dissimilarity in TPA cross-sections. To prove this theory, we first computed the natural lineshape based on the widths provided in their studies. Dividing their reported value for the cross-section by these lineshapes and then multiplying by our Doppler lineshape of similar conditions, we calculate numbers that nearly match our reported weighted average value. This is displayed in both Figure 18 and in Table 4. In an effort to further compare our value with those reported in the literature, we then applied our intensity model to the conditions under which Zapka et al. observed their spectra. We chose to use Zapka's reported conditions primarily because they were the most similar to our testing conditions.

Table 4. Comparing the previously reported values to our weighted average value for the Two-Photon Absorption (TPA) cross-sections measured for the $5^2S_{1/2} \longrightarrow 5^2D_{5/2}$ Transition in Rb.

Doppler-Free $\sigma_{2\phi}$ $\left(\frac{cm^4}{W}\right)$	Reference	Year	Type	Isotope	Doppler-Broadened $\sigma_{2\phi}$ $\left(\frac{cm^4}{W}\right)$
4×10^{-20}	Zapka *et al* [67]	1983	E	^{87}Rb	1.30×10^{-21}
1.2×10^{-18}	Collins *et al* [19]	1993	E	^{85}Rb	5.58×10^{-20}
0.57×10^{-18}	Marinescu *et al* [49]	1993	T	^{85}Rb	N/A
6.5×10^{-20}	Saha *et al* [43]	2011	T	^{85}Rb	3.51×10^{-21}
5×10^{-20}	Saha *et al* [43]	2011	E	^{85}Rb	2.70×10^{-21}
N/A	This Work	2013	E	^{85}Rb	6.78×10^{-21}

Both experiments employed a cw laser and a lens that resulted in a beam waist of $\approx 70\ \mu m$. Due to the similarity of the set-up presented in his work, we decided to apply our numerical model to the conditions Zapka reported. Our model calculated a TPA cross-section of $3.5 \times 10^{-20}\ \frac{cm^4}{W}$, which was within 12% of his reported number of $4.0 \times 10^{-20}\ \frac{cm^4}{W}$. This result not only proved greater confidence in our model, but also in the accuracy of Zapka's reported result. Next, we applied the theoretical equation presented in Equation 74 to calculate a TPA cross-section using the 50 MHz Lorentzian line width reported in the Saha et al. work. That number came to within a factor of 2 to Saha's reported value. Although Saha et al. was the first to use a PBGF to detect this weak transition using ultra-low powers, many similarities existed such as focusing the beam down to a small beam waist ($\approx 6\mu m$, $10\times$ smaller than Zapka and ours) and collecting an input and output intensity signal with a photodiode. For a complete list of the historical values, as reported in the literature, please refer to Table 4.

Having the TPA cross-section known for this particular transition allows for an approximation to be made about the pump intensity threshold condition for a potential TPAL. Using Figure 19 we arrive at the laser rate equations listed in Equation 30.

Quenching rates are not a significant process since the pump level ($5^2D_{5/2}$) is also the upper laser level to the 5.2 μm laser. This laser then populates the upper laser level of the blue laser.

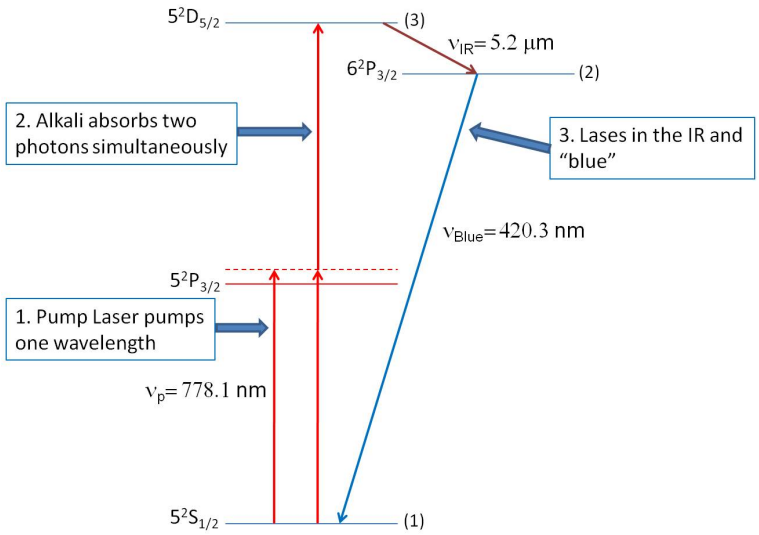

Figure 19. The 3-level TPAL system. The pump laser need only pump to the virtual state, as second order absorption sends population to the $5^2D_{5/2}$ state. An IR laser then sends population to the upper laser level of the blue TPAL.

$$\frac{dn_3}{dt} = \sigma_{2\phi}\frac{I_P^2}{h\nu_P}n_1 - \Gamma_{IR}n_3 \tag{30}$$

$$\frac{dn_2}{dt} = \Gamma_{IR}n_3 - A_{21}n_2 \tag{31}$$

where Γ_{IR} is the branching ratio for the first laser transition and A_{21} is the spontaneous emission for the upper laser level. Applying a steady state condition to Equation 30, we can define an approximation to the laser threshold condition to be,

$$I_{th} = \sqrt{(h\nu_P)\frac{A_{21}}{\sigma_{2\phi}}\left(\frac{n_2}{n_1}\right)} \tag{32}$$

Assuming that we have no losses in the system, $\alpha \longrightarrow 0$, we can define the population ratio in Equation 32 to be 2. Equation 32 now shows the importance

of knowing the TPA cross-section as a first step in developing a TPAL. For a TPA cross-section of 6.75×10^{-21} $\frac{cm^4}{W}$, the calculated threshold intensity is $I_{th} = 26.0$ $\frac{kW}{cm^2}$. This is about 26 times higher than a typical DPAL value for threshold. This value indicates a difficulty in developing a TPAL laser at higher alkali concentrations for a cw pump source. However, a pulsed dye laser has sufficient pump intensities to realize a TPAL laser. Under typical laser operations Doppler widths must be accounted for, which is why our value for the TPA cross-section is the most practical.

IV. XPAL

4.1 Introduction

The Diode Pumped Alkali Laser (DPAL) and its cousin, the Exciplex Pumped Alkali Laser (XPAL), have received considerable attention for high power applications. The DPAL system is optically pumped in the core of the D_2 absorption line of K, Rb, or Cs and lases on the D_1 line after collisional fine structure mixing between the excited $^2P_{3/2,1/2}$ states [17, 28, 56, 65]. In contrast, the XPAL system is pumped in the blue satellite wing of the D_2 line and lases either on the D_2 or D_1 line [34, 35, 36, 37, 38]. A pulsed XPAL was first demonstrated in 2009 by pumping atomic cesium in a mixture of 500 $Torr$ of argon to induce the satellite blue peak near 837 nm and 100 $Torr$ of ethane to collisionally relax the dissociated Cs $^2P_{3/2}$ population to the upper laser level, $^2P_{1/2}$ [35]. Lasing on the $^2P_{1/2} \longrightarrow ^2 S_{1/2}$ D_1 line at 894.3 nm is achieved across a broad band, $\approx$ 3 nm of pump wavelengths, in this five-level version on the XPAL system. Threshold was observed at $40-120$ $J/pulse$ and slope efficiencies of up to 5% were achieved, depending on cesium concentration [34, 35, 38]. More recently, a four-level version of the XPAL was demonstrated with high quantum efficiency, $>$ 98%, and no requirement for hydrocarbons [36, 37]. The four-level Cs-Ar system exhibits a threshold at $130-250$ J in a 4 ns pulse with an efficiency of about 1% and has been scaled in pump rate to $2-3$ times threshold [4, 36, 37]. Lasers operating at 852.1 nm in alkali-rare gas mixtures of Cs-Ar, Cs-Ar/Xe, and Rb-Ar at pressures of 500 $Torr$ have also been demonstrated at higher pump energy, $<$ 40 mJ, and longer pulse durations, $6-11$ ns [33]. The threshold is higher, $1.5-12$ $mJ/pulse$, and slope efficiency less, $\approx$ 0.4%, presumably due to a larger pump spot size. In the present work, we seek to extend the four-level Rb-Ar XPAL performance characterization to higher pressures (2500 $Torr$), scale the pump rate to $>$ 8 times threshold, investigate

the laser dynamics, compare static gain cells with heat pipes, and demonstrate a Rb-Kr XPAL variant.

The potential energy surfaces for several alkali metal vapor-rare gas pairs have recently been computed at the spin-orbit multi-reference configuration interaction level [46]. The Rb-Ar surfaces for the lowest electronic states are illustrated in Figure 20. In the separated atom limit the $X^2\Sigma^+_{1/2}$ surface corresponds to the $^2S_{1/2}$ ground state energy level of the alkali, the $A^2\Pi_{1/2}$ surface corresponds to the $^2P_{1/2}$ energy level, and the $A^2\Pi_{3/2}$ and $B^2\Sigma^+_{1/2}$ surfaces correspond to the $^2P_{3/2}$ energy level. The $X^2\Sigma^+_{1/2}$ surface is mostly repulsive, with a shallow well (49 cm^{-1}) in the region of $R \approx 0.58$ nm. The $B^2\Sigma^+_{1/2}$ surface also exhibits a shallow well (7.3 cm^{-1}) in the asymptotic limit of $R \approx 10.5$ nm, as well as a shoulder on the repulsive wall at smaller values of R. Dipole allowed transitions of the Rb-Ar collision pairs from the ground state to the dissociative $B^2\Sigma^+_{1/2}$ surface produces a satellite on the blue side of the D_2 atomic line. The blue wing for the Rb-Ar system has been experimentally observed at 755.5 or 754 nm [18]. Lasing emission on the Rb D_2 line occurs at 780.2 nm.

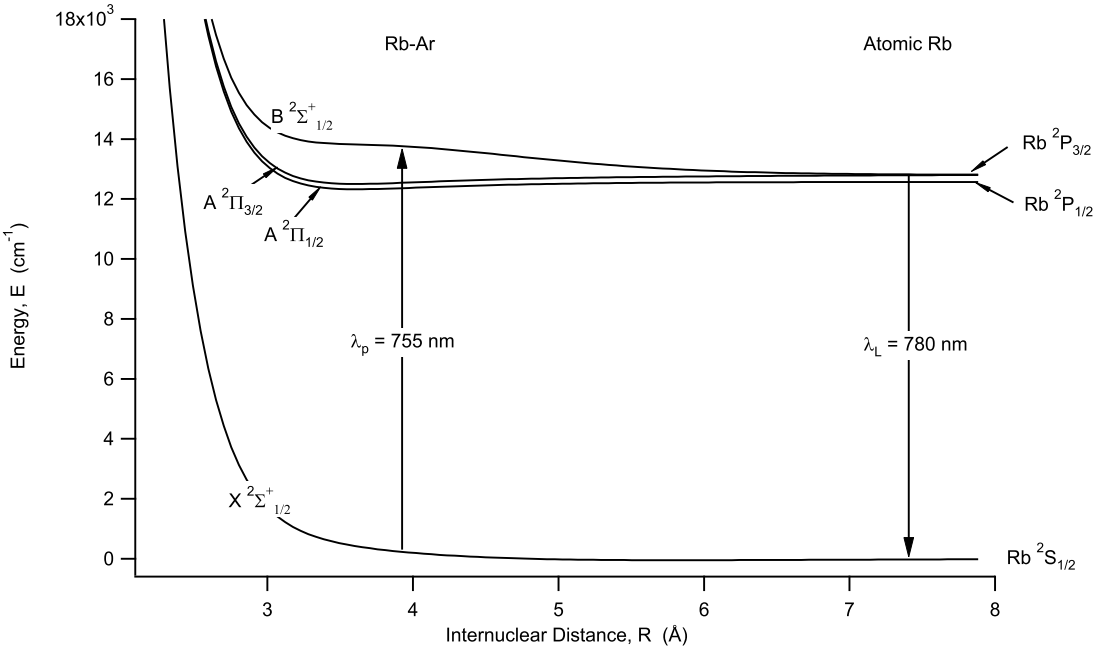

Figure 20. The first four Rb-Ar surfaces and three lowest atomic Rb states [46].

Most DPAL and all XPAL lasers have previously employed static gas cell at a fixed, near atmospheric pressure for the gain medium. Heat pipe configurations offer higher alkali concentrations, variable buffer gas pressures, and avoid alkali condensation on cell windows [30]. A 3 atm, hydrocarbon free heat pipe was used to scale pulsed pump intensities in a K-He DPAL to greater than 10 MW/cm^2 while retaining greater than 10% slope efficiency [31]. Stimulated Raman and multi-photon excitation processes have been observed at these very high pump intensity conditions [42]. The utility of the heat pipe configurations for XPAL devices are explored in the present work.

4.2 Experimental

A schematic diagram of the experimental set-up is shown in Figure 21a. Unlike previous studies demonstrating the XPAL system [4, 33, 34, 35, 36, 37, 38], this study used a glass cell connected to a gas handling system or a heat pipe [30] to evaluate high pressure conditions. In previous studies, a sealed cell with a fixed amount of rare gas and a few micro-grams of alkali was employed [4, 33, 34, 35, 36, 37, 38]. The glass cell used in the current experiment has a vertical "finger" located on the bottom of the cell and centered between the windows with about a gram of Rb. Heat tape was wrapped around this finger, monitored with a resistance temperature detector and maintained to 1 ^0C by an Omega temperature controller. The vapor pressure of Rb at $T = 453 - 513\ K$ yields concentrations of $0.34 - 3.3 \times 10^{15}\ \frac{atoms}{cm^3}$. The 17 cm long glass cell rests in a stainless steel oven at $5 - 10\ ^0C$ above the finger temperature to prevent window condensation. Vacuum ($\approx 1\ Torr$) and buffer gas handling was controlled through a valve and glass-to-metal interface on the top the cell.

The stainless steel heat pipe illustrated in Figure 21c was substituted for the glass cell for several experiments [30]. About 2 g of Rb was loaded using a nitrogen purged glove box. A stainless steel oven is clamped around the center of the heat pipe. Two

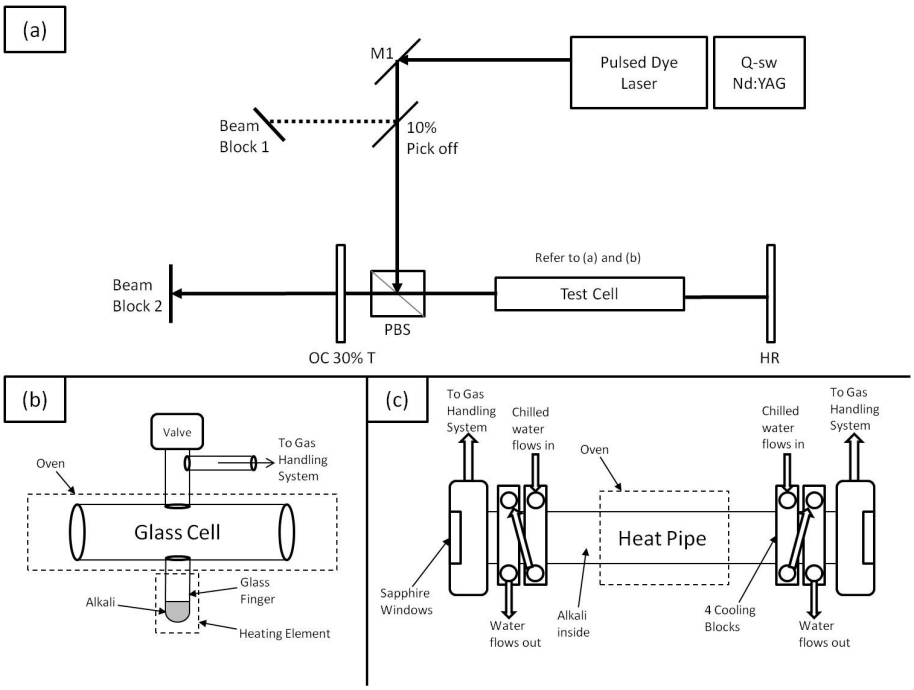

Figure 21. The Rb-Ar apparatus. Panel (a) display the optical path and important elements of the beam train. Panel (b) describes the geometry of the glass test cell used for part of the experiments. Panel (c) explains the geometry and important features of the heat pip configuration used for the majority of the results.

water-cooled (20 ^0C) jackets towards the ends of the pipe condense the alkali and a wire mesh inside the heat pipe wicks the liquid alkali back to the center. Although the heat pipe is 38 cm long, the active gain medium between the cooling jackets measures about 24 cm in length. Heat pipe temperature of $398 - 448$ K yields alkali concentrations of $0.22 - 2.76 \times 10^{14}$ $\frac{atoms}{cm^3}$. The rare gas purity was 99.998% and the maximum pressure was 2500 $Torr$. Pressure was measured using an MKS model 626A13TAE capacitance manometer. The alkali used was natural isotopic abundance rubidium.

A Q-switched Quanta Ray Nd:YAG laser pumped a Sirah model PRSCD18 pulsed dye laser to produce up to 23.5 mJ in a $8.3 - 9.7$ ns pulse at 10 Hz. Exciton LDS 765 dye in propylene carbonate and methanol provided a tuning range of $735 - 795$ nm, with a peak at about 762 nm. The spot size was determined by capturing burn

images of the incident pump pulse prior to entering the test cell. For energies ranging from $0.35 - 21.2\ mJ/pulse$ spot sizes ranged from $0.13 - 0.20\ cm^2$. A fast ($1\ ns$) Si photodetector and 3 GHz oscilloscope monitored pump and XPAL laser pulses. A 780 nm notch filter, with a 10 nm bandwidth, was used to filter out the pump wavelength. An Ocean Optics spectrometer was used to analyze the pump and XPAL wavelengths. Average output power was recorded on a Coherent FieldMax-TO power meter.

The pump beam enters the XPAL cavity by way of a Polarizing Beam Splitter. The cavity mirrors consisted of a 25 cm high reflector and a flat, 30% transmission output coupler, spaced by 53 cm. The cavity round trip time is 3.5 ns. Sapphire windows at normal incidence were used on the ends of the heat pipe. Insertion of the heat pipe and beam splitter into the cavity introduces a large loss of $\approx 60 - 70\%$ per pass for a HeNe 632.8 nm probe. The heat pipe loss increases significantly at pressures above 1500 $Torr$, particularly at high temperature (448 K), as discussed below.

4.3 Results

The current laser demonstrations were conducted using the four level variant of the XPAL system. Figure 22 illustrates the spectrum of the XPAL power using the heat pipe at 500 $Torr$ of argon at a cell temperature of 494 K. The pump source is tuned to 755.5 nm in the far blue wing of the D_2 line and significant pump energy is transmitted through the cell. Strong lasing is observed on the Rb $5^2P_{3/2} \longrightarrow 5^2S_{1/2}$ transition near 780 nm. No laser emission is observed on the $5^2P_{1/2} \longrightarrow 5^2S_{1/2}$ transition near 795 nm. A 780 nm notch filter, with a 10 nm bandwidth, was used to filter out the pump wavelength in subsequent measurements.

The dependence of the XPAL output energy on the pump wavelength is shown

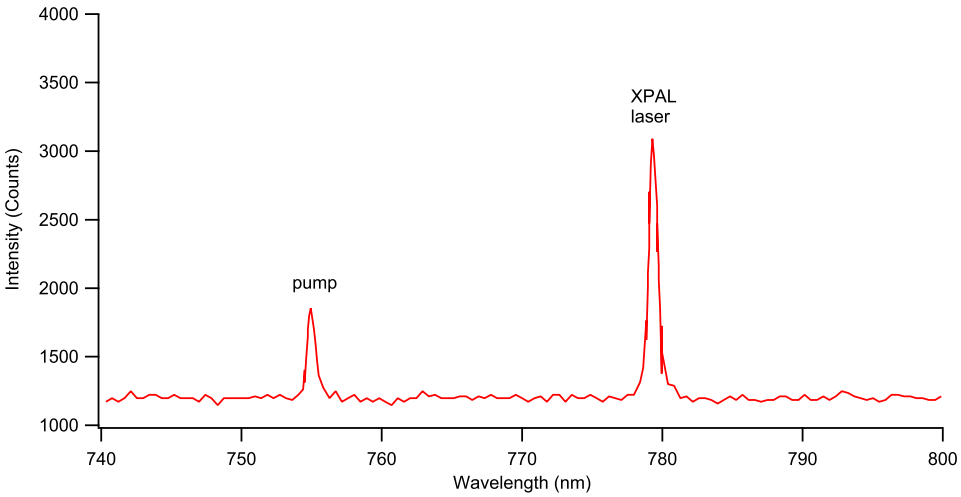

Figure 22. An Ocean Optics Spectrometer was used to verify emission of the laser level.

in the excitation spectra of Figure 23. Despite the $\approx$ 20% pulse-to-pulse variation in both pump and XPAL output energy, the peaks at $755.0 \pm 0.5\ nm$ for the Rb-Ar system and $759 \pm 0.3\ nm$ for Rb-Kr are clearly evident. Lasing threshold for the Rb-Ar system is observed on the blue side at $752.3\ nm$ where the absorption cross-section is reduced by a factor of $3.3 - 4.6$ from the peak, depending on temperature [18]. Lasing is sustained for pump wavelengths longer than $760\ nm$ where the absorption reaches a minimum before extending into the core of the D_2 line. In contrast, the lower pressure Rb-Kr system supports lasing in a narrow range of $757.1 - 760.4\ nm$. The reduced performance for the Rb-Kr system in Figure 23 reflects the lower pressure conditions rather than the relative merit of the collision partner. Comparing Ar and Kr performance at common $500\ Torr$ and $398\ K$ conditions, yields output energies of 0.92 and 3.2 J, respectively. This is qualitatively consistent with the observed absorption cross-section for Kr being about 70% greater than for Rb-Ar [18].

The scaling of output energy with absorbed pump energy for the heat pipe configuration is explored using two approaches in Figure 24. First, the energy per pulse as measured by the power meter and inferred from the 10 Hz repetition rate is

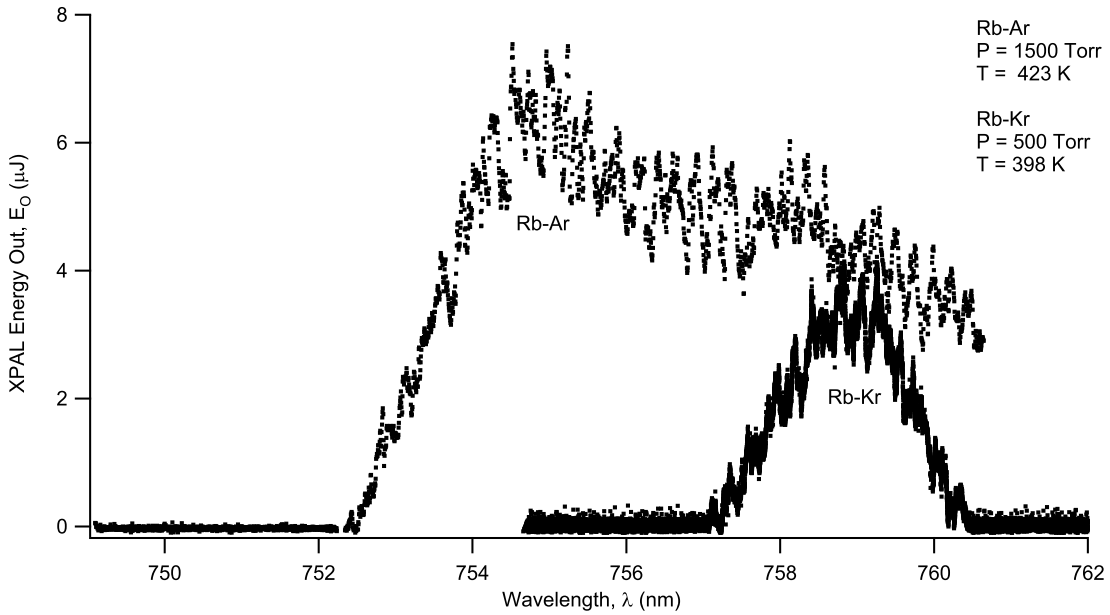

Figure 23. Excitation spectra of both the Rb-Ar and Rb-Kr pair. These peaks centered at $755.0 \pm 0.5\ nm$ and $759 \pm 0.3\ nm$ respectively. The Rb-Ar laser excitation curve is taller and wider than the Rb-Kr curve because of the conditions (temperature and pressure) by which they were observed.

measured for both the pump and XPAL lasers. The fraction of the incident pump energy absorbed by the Rb vapor is determined by comparing the transmitted power at the peak of the blue wing feature at $\lambda = 755\ nm$ and the off-resonance at $\lambda = 750\ nm$. For 1500 $Torr$ of argon and $T = 423\ K$ the fraction absorbed ranges from $0.804 - 3.24\ mJ/pulse$ as the incident pump energy is scaled from $5.4 - 21.8\ mJ/pulse$. A linear fit to this data is shown in Figure 24 and yields a threshold of $0.38 \pm 0.02\ mJ/pulse$ of absorbed energy or $2.55\ mJ/pulse$ incident energy. For the 10 ns pulse focused to an area of $0.01\ cm^2$, this corresponds to an average pump intensity of 25.5 $\frac{MW}{cm^2}$. The fit slope efficiency is 0.236 ± 0.003 %.

A second approach to developing the results of Figure 24 employs the full temporal dependence of the pump and XPAL output pulses. Using the fast photodiode and normalizing the temporally integrated pulse area to the observed average energy provides the instantaneous intensity curves in Figure 24. For an incident pump en-

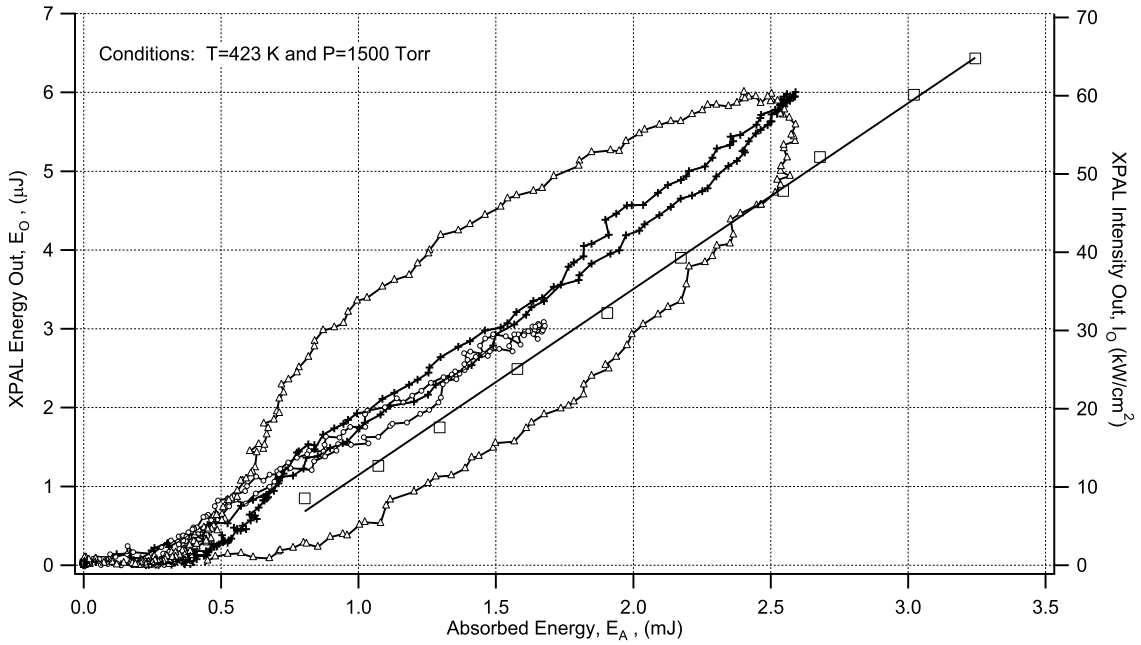

Figure 24. Two methods for obtaining the slope efficiency are shown. The data with the linear fit was collected by the common method of measuring the absorbed pump energy and output laser energy at certain intervals of pump intensity. The more non-traditional method is to use a single laser pulse to sketch out all needed energies. A photon build-up time was determined from the geometry of the set-up. When factored out, the hysteresis collapses to a steady state condition. The discrepancy in intercepts is probably due to the different methods in collecting the data. Only the slope efficiency was collected from this method in this study.

ergy of 21.8 $mJ/pulse$, the instantaneous intensity traces an oval shape propagating counter-clockwise as time progresses. The full temporal dynamics of the two pulses can be organized by a simple temporal delay between the pump and XPAL pulses of about $\tau_b \cong 3\ ns$, which can be attributed to the photon buildup time. Introducing this delay reduces the hysteresis to a single linear relationship, consistent with the average energy measurements. A pump pulse with lower energy of 12.8 $mJ/pulse$ yields similar results. Thus, the full scaling relationship can be interrogated from a single, high energy pulse. It is worth noting that some nonlinear behavior is observed near threshold in all the plots of Figure 24, consistent with the upward curvature (increasing slope efficiency) observed in the earlier XPAL demonstrations [34, 35, 38].

The photo build-up times observed in the glass cell for all the argon pressures and

cell temperatures are provided in Figure 25. The delay decreases from 3.7 to 2.8 ns as the Rb concentration increases by a factor of 9.7 (achieved by changing the cell temperature from $453-513\ K$) The photon build-up time is inversely proportional to the gain, and the XPAL inversion depends on both the rubidium concentration and the argon pressure (due to the increased blue wing absorption) [4]. Indeed, Figure 25 demonstrates an approximately linear relationship. The gain is clearly large and is estimated as $\gamma \approx \frac{20}{c\ \tau_b} = 18 - 24\frac{\%}{cm}$, where the factor of 20 is a typical value for well saturated lasers. Delays using the heat pipe configuration at higher argon pressures (less than 2500 $Torr$) and longer active region are even less, $1.0 - 1.9\ ns$.

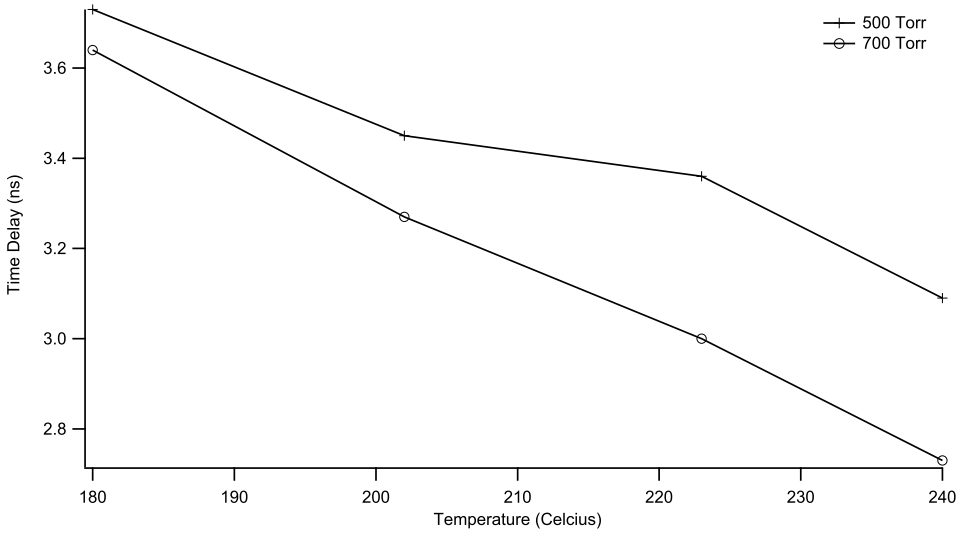

Figure 25. The photon build-up time in the glass cell configuration was shown to decrease with increasing alkali concentration as expected.

The observed slope efficiencies increase as the Rb and Ar concentrations increase, as shown in Figure 26. The absorption of the pump photons in the blue wing of the D_2 line depends on both the alkali and rare gas concentrations [4, 35, 37, 38, 48]. An analytic model for the standard DPAL system, predicts a slope efficiency which depends exponentially on the absorbance, A: [28]

$$\eta_s = \eta_0(1 - e^{-A}) \tag{33}$$

A fit of Equation 33 to the data in Figure 26 yeilds an effective absorption cross-section of $A = \sigma\ n\ L$ of $\sigma = 8.16 \pm 1.8 \times 10^{-17}\ cm^2$ at argon pressures of 500 and 700 $Torr$, which is approximately linearly dependent on buffer gas pressure. This is about 10^{-4} of the peak D_2 cross-section, consistent with prior asymmetric lineshape observations [33, 35, 37, 38, 48]. The efficiency in the heat pipe configuration is dramatically higher, despite the lower Rb concentration. However, at high pressure and temperature efficiency becomes quite poor, as discussed below. These lower efficiency conditions are not included in the plot of Figure 26. The current Rb-Ar slope efficiencies are lower than previously reported for the Cs-Ar system of $\approx 1\%$ [4], consistent with the qualitative observations reported by Readle [35, 36, 37, 38].

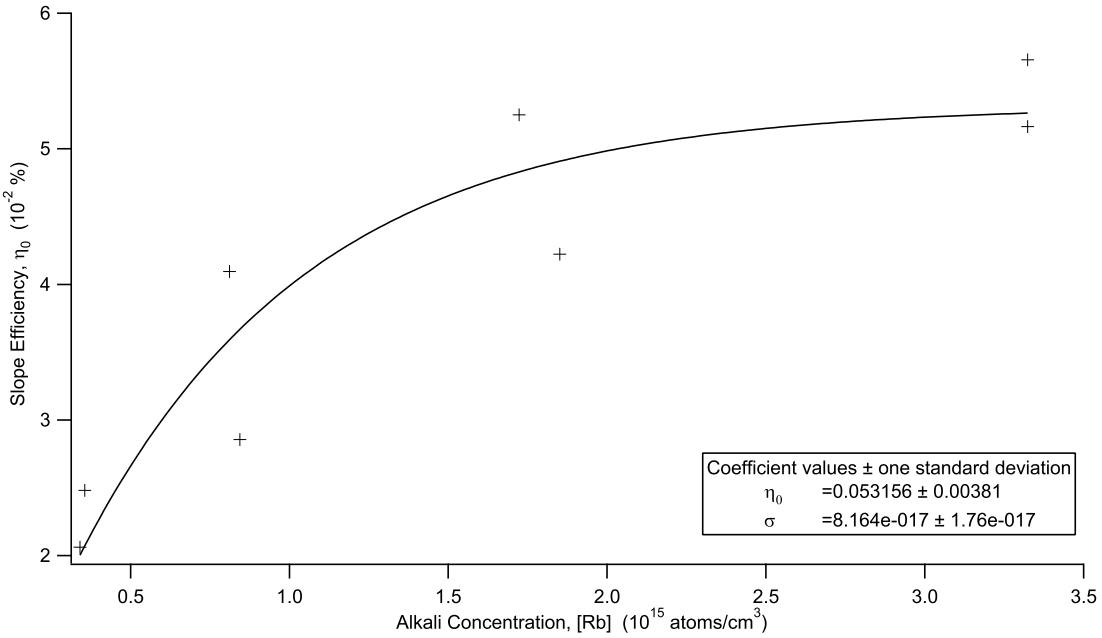

Figure 26. We extract an effective absorption cross-section by fitting the function derived by Hager. [28]

The number of pump photons per pulse is high, 8.29×10^{16} photons at $21.8\ mJ/pulse$. The number of available Rb atoms in the pumped volume of the glass cell is lower, 2.22×10^{13} to 2.76×10^{14} $atoms$, depending on the cell temperature. The number of Rb-Ar pairs is lower still and can be estimated from the potential surfaces [46].

This effect is accounted for when considering the reduced cross-section when pumping in the blue wing. The fraction of the incident photons absorbed is low and the optical-to-optical efficiency suffers from the highly bleached conditions.

We anticipated improved performance as both Rb and Ar density increased further and the heat pipe provided capability to extend the range to $T < 800\ K$ and $P < 2500\ Torr$. The slope efficiencies observed for the heat pipe configuration are provided in Figure 27. Surprisingly, no lasing was achieved in this configuration for $T > 448\ K$. Slope efficiencies increase initially with pressure and temperature, but degrade rapidly above 428 K and 2000 $Torr$.

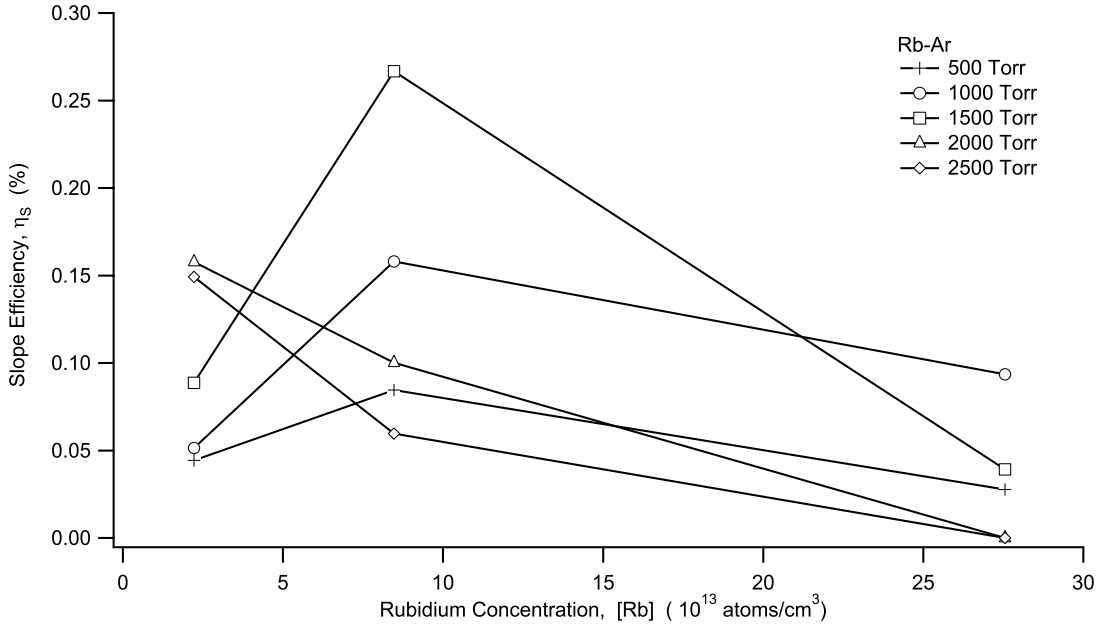

Figure 27. Slope efficiencies for the various test conditions performed with the heat pipe. An obvious degradation in performance is shown for high pressures and temperatures. We don't believe this is a real XPAL effect, but rather a consequence of not fully understanding the heat pipe operational conditions.

We visually observed condensation of alkali vapor and the production of suspended aerosols in the heat pipe at the higher pressures and temperatures, only when the pump laser was incident on the medium. Figure 28 illustrates the optical transmission for a low power HeNe laser (632.8 nm) as a function of HeNe pump energy for several

heat pipe conditions. The transmission is high and independent of HeNe pump energy for the lower pressures and temperatures. However, the transmission is very poor at elevated pressure and temperature for incident pump energies exceeding 0.5 μJ. Indeed, there is an abrupt, unstable transition to low transmission when the heat pipe is illuminated for more than 5 seconds, as illustrated in Figure 29. Apparently, the heat load induced by the pump beam induces a phase change in the heat pipe at higher operating pressures and temperatures, limiting further scaling.

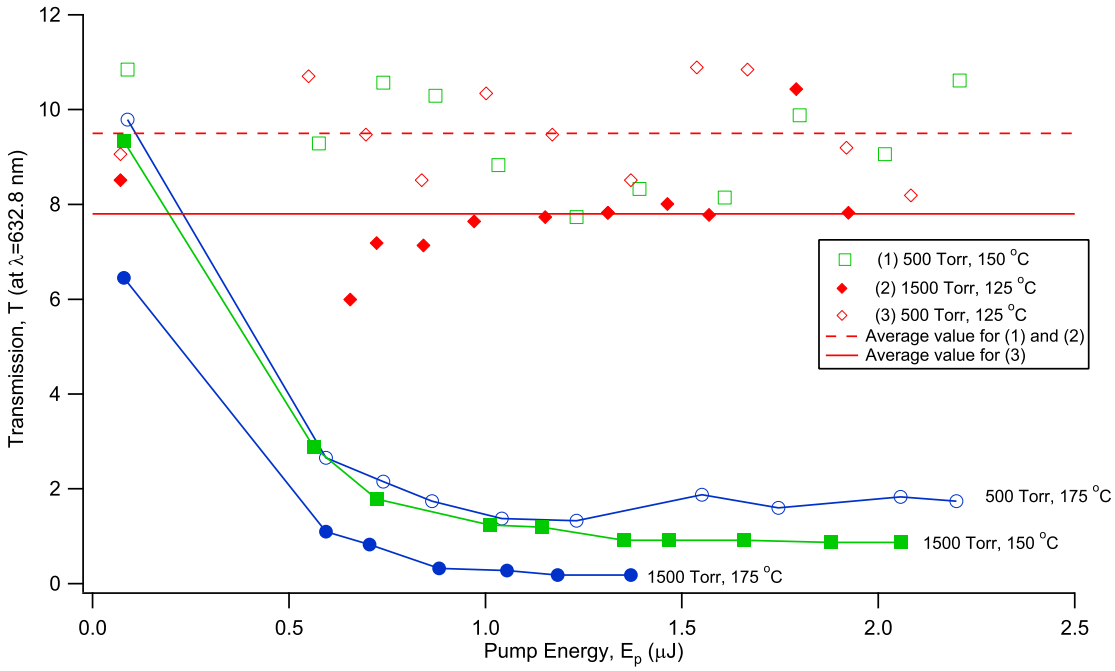

Figure 28. Transmission of a low power HeNe laser down the optical axis of the heat pipe as a function of pump energy, alkali concentration and pressure. Each curve is labeled with the condition the data was collected under.

Finally, a Rb-Kr XPAL system was demonstrated using the heat pipe configuration. The instantaneous slope efficiencies for the Kr buffer gas are provided in Figure 30. Unfortunately, no lasing was observed for the higher pressure and temperature conditions. However, the production of aerosols for Kr system appears to occur more readily and is likely the explanation for the degraded performance. Indeed, the Rb-Kr system exhibits improved slope efficiencies over the Rb-Ar system for the

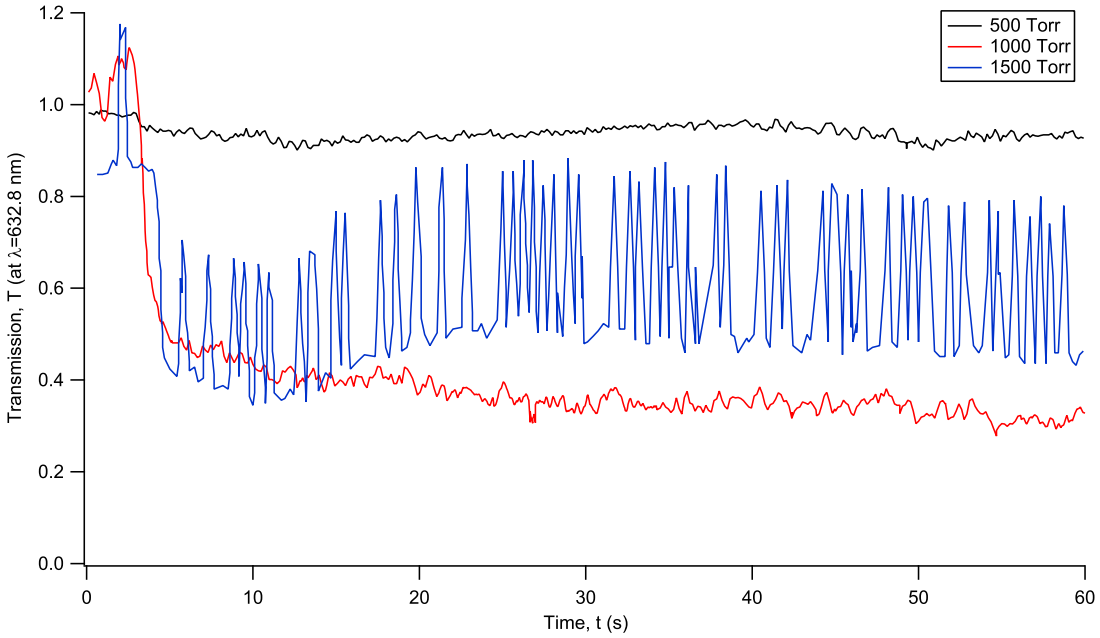

Figure 29. Transmission of a low power HeNe laser down the optical axis of the heat pipe as a function of time. This shows the degrading mechanism to have a time dependent function that increases with pressure.

lowest pressures and temperatures.

4.4 Conclusion

The performance characterization of the exciplex pumped alkali laser, XPAL, has been extended to pressure above 1 atmosphere and pump intensities exceeding 15 $\frac{MW}{cm^2}$ in the present work. Threshold is observed at about 0.5 mJ absorbed energy (3 $mJ/pulse$ incident energy) and the system has been scaled to greater than 8$\times$ threshold. The laser dynamics are consistent with quasi-cw behavior, requiring only a photon build-up time of $1-3$ ns to explain the temporal nature of the output. However, a cw XPAL demonstration remains elusive, due to the high pump intensities required. Extending performance to higher pressures and temperatures using a heat pipe will require control of condensation induced by laser heating. The first XPAL system using Rb-Kr pairs was presented with performance potentially exceeding the

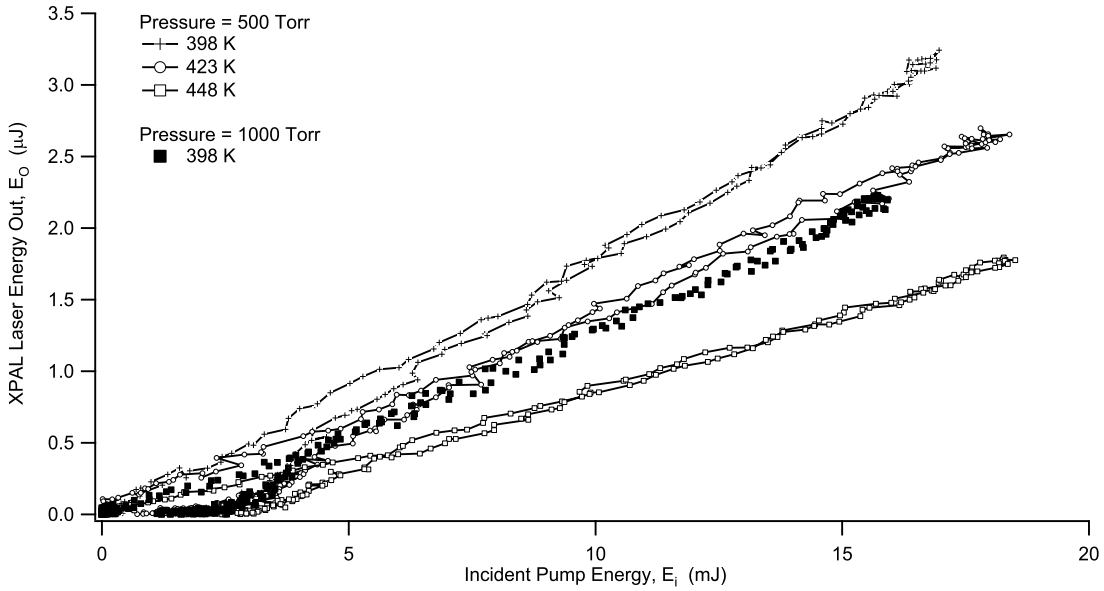

Figure 30. Slope efficiencies for the Rb-Kr XPAL.

Rb-Ar system.

V. Conclusion

This work has demonstrated for the first time a measurement of the Doppler-broadened TPA cross-section for the $5^2S_{1/2} \longrightarrow 5^2D_{5/2}$ transition in naturally occurring Rb using direct absorption methods. Our reported statistical average hyperfine broadened TPA cross-section is 7.6×10^{-21} $\frac{cm^4}{W}$. This work also provides an intensity model that accounts for the Gaussian propagation term and the TPA cross-section absorbing term, which allows for absorbance values to be converted into TPA cross-section units of $\frac{cm^4}{W}$. Although the values calculated by Zapka et al. and Saha et al. were 5 and 6.5 times our calculated value respectively, we believe that this discrepancy is largely accounted for in the lineshape. Both of their experiments used a sub-Doppler technique, whereas our direct absorption method and Voigt model used the Doppler widths at high temperatures to generate sufficient alkali concentrations. The values calculated by Marinescu et al. and Collins, however, were orders of magnitude different and it is believed they incorporated subtle errors into their work. The calculated TPA cross-section in this work indicates a required pump intensity threshold that is approximately 25 times greater than a typical DPAL system. Although these intensities are achievable using pulsed lasers, the likelihood of developing a cw TPAL system is greatly decreased. The value calculated in this work becomes the most practical reported number when considering the feasibility of a TPAL system because the lineshape dependence of the cross-section. In typical laser operations the Doppler width must be accounted for.

In the area of XPALs, this work was the first to develop a working Rb-Ar and Rb-Kr XPAL in a heat pipe configuration. These particular XPALs optically pumped the blue satellite of the D_2 line from the ground Rb-Ar or Rb-Kr collision pair to the dissociative, $B^2\Sigma^+_{1/2}$ state produce laser emission at 780.2 nm. We achieved lasing for a band of pump wavelengths of $752.6 - 760.0$ nm for the Rb-Ar system and

$757.7 - 759.8\ nm$ for the Rb-Kr system. This work was also the first to characterize XPAL laser operation at pressures above 1 atmosphere and pump intensities exceeding 15 $\frac{MW}{cm^2}$. Threshold was observed at about 0.5 mJ absorbed energy (3 $mJ/pulse$ incident energy) and the system has been scaled to greater than 8 times threshold. This is significantly less than the values calculated for the Cs-Ar systems by Readle et al., which ranged from 40 μJ at 444 K to 140 μJ at 468 K. Our operating temperatures and pressures were limited by a condensation of the alkali due to the heat pipe configuration. This effect was exacerbated by laser induced heating and increased alkali vapor pressures. The laser dynamics are consistent with quasi-cw behavior, requiring only a photon build-up time of $1 - 3\ ns$ to explain the temporal nature of the output. However, a cw XPAL demonstration remains elusive, due to the high pump intensities required. Extending performance to higher pressures and temperatures using a heat pipe will require control of condensation induced by laser heating. Finally, slope efficiencies increased with both Rb and Ar concentrations and exceed 0.25% using the heat pipe configuration.

5.1 Contributions

The TPA cross-section leads to efforts in developing an efficient TPAL system. This laser system has the potential to benefit Naval communications for submarines in shallow water. The 420 nm wavelength is able to penetrate further than most optical wavelengths through the water absorbing bands. Pumping to other two-photon transitions in Rb will allow access to other micron-range laser systems, which could also benefit advanced IR countermeasure technology.

The XPAL research provides important data to the growing laser community seeking for the next non-chemical high-power laser system. The results from this work suggests exciting areas to explore using the heat pipe configuration, and provides

lessons learned from the unexpected results presented.

5.2 Future Work

Many areas have been identified as potential research areas throughout the course of this research in the TPA cross-section. First of all, it was the intention of this research to calculate the pressure broadening rates by extracting Lorenztian linewidths from a series of pressure broadened TPA transitions in Rb. This will greatly enhance the understanding of the contributing factors of a lineshape resulting from a TPA process. The next obvious step, after calculating the broadening rates, is to build a TPAL cavity and test various designs while monitoring and modeling the performance. The most interesting aspect of this transition is the simultaneous emission of two laser wavelengths. This fact alone could drive varying ideas of cavity configuration. Glass cells were used in the measuring of the TPA cross-section, but considering the use of a heat-pipe is also very promising. A heat-pipe configuration would not experience the degradation in performance at high temperatures that this research encountered. Using a heat-pipe, one could even redo much of this work and then extend to higher temperatures and pressures.

For the XPAL work, demonstrating and reporting the adequate operating conditions for the heat pipe configuration would be very useful for analyzing high pressure XPAL performance. Avoiding large temperature gradients is a challenge when working at high temperatures in a heat pipe. Understanding the proper setting of the cooling jackets may have a significant contribution. Once the heat-pipe operation is better understood, it is recommended that various alkali-rare gas combinations are tested and analyzed for performance.

Appendix A. Developing the General Equation and the Numerical Solution

The intensity modeled by Equation 19 is the result of developing a relationship that accounts for the two competing processes found within the alkali test cell. The first process describes the intensity increasing due to the decreasing beam waist, and the second describes the intensity attenuated through the absorption medium. Figure 31 illustrates the processes needed to develop a model for the intensity profile in the test cell. As the shaded region travels in the z-direction, the intensity increases linearly in I as it approaches the beam waist and decreases quadratically in I as the flux of photons increases and invokes stronger TPA.

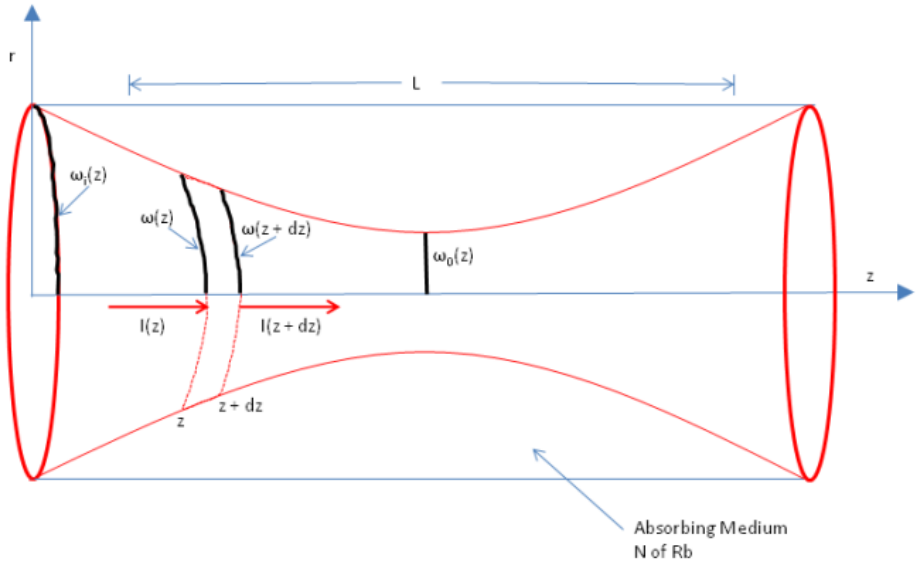

Figure 31. The laser beam passes through a focus as it travels through the Rb Vapor. An accurate calculation of the TPA cross-section requires a model of $I(z)$.

The first process is a result of a Gaussian beam propagating through a focus and the second arises from the two-photon version of the Beer-Lambert Law. The general equation describing the behavior of these processes can be written as,

$$I(z+dz) = I(z) - \sigma_{2\phi} N I^2(z) dz + F(z) I(z) dz. \tag{34}$$

$I(z)$ is a known intensity at some point z and $I(z+dz)$ is the intensity at a later point dz away. The second term is the TPA model and the third term is the focusing behavior of the Gaussian beam propagating through free space, which was derived from Equation 11. It is necessary to subtract a factor of $\frac{L}{2}$ from the propagation distance, z, in the Gaussian term in order to linearly add the two-photon term to the Gaussian term. Using Equations 11 and 34, along with careful algebra, we arrive at the following equation which this work refers to as the "Governing Equation".

$$\frac{dI(L)}{dL} = -\sigma_{2\phi} N I^2(L) + \left[\frac{2}{\omega(L)}\frac{d\omega(L)}{dL}\left(\frac{r^2}{\omega^2(L)} - 1\right)\right] I(L) \tag{35}$$

where,

$$\omega(L) = \omega_0^2\left[1 + \alpha^2(L-H)^2\right] \tag{36}$$

and,

$$\frac{d\omega(L)}{dL} = \frac{\omega_0 \alpha^2 (L-H)}{\left[1 + \alpha^2(L-H)^2\right]^{1/2}} \tag{37}$$

Substituting the relations of Equations 36 and 37 into Equation 35, yields the differential equation that is a function of α and L.

$$\frac{dI(L)}{dL} = -\overbrace{\sigma_{2\phi} N}^{a_2} I^2(L) + \overbrace{\left[\frac{2\alpha^2(L-H)}{1+\alpha^2(L-H)^2}\left(\frac{r^2}{\omega_0^2\left[1+\alpha^2(L-H)^2\right]} - 1\right)\right]}^{g(L)} I(L) \tag{38}$$

$$\frac{dI(L)}{dL} = -a_2 I^2(L) + g(L) I(L) \tag{39}$$

We take a moment to divert from the full development in order to find a definition

for $I_1(L)$ from Equation 17. We do this by forcing a one-photon approximation to Equation 39, by setting $a_2 I^2(L) \longrightarrow \overbrace{a_2 I_0}^{a_1} I(L)$, such that

$$\frac{dI(L)}{dL} = -a_1 I(L) + g(L)I(L) = (-a_1 + g(L))I(L) \tag{40}$$

Now we have,

$$\int \frac{dI(L)}{I(L)} = \int (-a_1 + g(L))dL \tag{41}$$

and,

$$\int \frac{dI(L)}{I(L)} = -a_1 L + \overbrace{\int g(L)dL}^{I_1(L)} + C \tag{42}$$

This is how we arrive at our definition for $I_1(L)$ in Equation 17. This integral is analytic and will be useful to solve here. First, let us further set $\beta = \frac{r^2}{\omega_0^2}$ and perform a $u - substitution$ such that $u = 1 + \alpha^2(L - H)^2$.

$$\int \frac{\beta du}{u^2} - \int \frac{du}{u} = \beta \int u^{-2} du - \int \frac{du}{u} \tag{43}$$

$$= \beta \frac{u^{-1}}{-1} - ln(u) = -\frac{\beta}{u} - ln(u) \tag{44}$$

Substituting u back into Equation 44, we get the final answer for $I_1(L)$.

$$I_1(L) = -\frac{\beta}{1 + \alpha^2(L - H)^2} - ln\left(1 + \alpha^2(L - H)^2\right) \tag{45}$$

It is interesting to note that this integral is analytic and is defined under a one-photon approximation. We could have arrived at this same definition by simply carrying out the Bernoulli Solution, but understanding the one-photon approximation

Table 5. Definitions to Bernoulli's form.

Bernoulli Coefficient	Governing Equation
y	I(L)
x	L
P(x)	- g(L)
Q(x)	- a_2
n	2

is more enlightening. Equation 35 must be solved using Bernoulli's Solution since it has the same differential form as

$$\frac{dy}{dx} + P(x)y = Q(x)y^n \tag{46}$$

The next logical step is to rearrange Equation 39 to match the elements in Equation 46.

$$\frac{dI(L)}{dL} - g(L)I(L) = -a_2 I^2(L) \tag{47}$$

The relationships defined in Table 5 is a result of aligning Equation 47 with Equation 46.

Next we use Bernoulli's solution in Equation 48 to solve for $I(L)$.

$$y^{1-n} e^{(1-n)\int P(x)dx} = (1-n)\int Q(x) e^{(1-n)\int P(x)dx} dx + C \tag{48}$$

$$I(L)^{-1} e^{(-1)\int -g(L)dL} = (-1)\int -a_2 e^{(-1)\int -g(L)dLdL} + C \tag{49}$$

Rearranging terms and substituting the definition for $I_1(L)$ we now can define $I_2(L)$,

$$\frac{1}{I(L)} e^{I_1(L)} = a_2 \overbrace{\int e^{I_1(L)} dL}^{I_2(L)} + C \tag{50}$$

Now our solution has a form simple enough to solve for the constant of integration.

$$\frac{1}{I(L)}e^{I_1(L)} = a_2 I_2(L) + C \tag{51}$$

The initial condition occurs at the start of the test cell, or when L=0.

$$\frac{1}{I(0)}e^{I_1(0)} = a_2 I_2(0) + C \tag{52}$$

So,

$$C = \frac{1}{I(0)}e^{I_1(0)} - a_2 I_2(0) \tag{53}$$

Inserting Equation 53 into Equation 51, we have the start of the complete solution.

$$\frac{1}{I(L)}e^{I_1(L)} = a_2 I_2(L) + \frac{1}{I(0)}e^{I_1(0)} - a_2 I_2(0) \tag{54}$$

The next several steps is simply algebra forming Equation 54 into the form of Equation 8.

$$\frac{1}{I(L)}e^{I_1(L)} = a_2(I_2(L) - I_2(0)) + \frac{1}{I(0)}e^{I_1(0)} \tag{55}$$

$$\left[\frac{1}{I(L)}e^{I_1(L)} - \frac{1}{I(0)}e^{I_1(0)} = a_2(I_2(L) - I_2(0))\right] I_0 e^{-I_1(0)} \tag{56}$$

$$\frac{I_0}{I(L)}e^{I_1(L)}e^{-I_1(0)} - 1 = a_2\left[I_2(L) - I_2(0)\right] I_0 e^{-I_1(0)} \tag{57}$$

$$\frac{I_0}{I(L)}e^{I_1(L)-I_1(0)} = 1 + a_2 I_0\left[I_2(L) - I_2(0)\right] e^{-I_1(0)} \tag{58}$$

$$\frac{I(L)}{I_0}e^{-[I_1(L)-I_1(0)]} = \frac{1}{1+a_2 I_0\left[I_2(L)-I_2(0)\right]e^{-I_1(0)}} \tag{59}$$

And finally, we get back Equation 60.

$$I(L) = \frac{I_0 e^{[I_1(L)-I_1(0)]}}{1+\sigma_{2\phi}NI_0\left[I_2(L)-I_2(0)\right]e^{-I_1(0)}} \tag{60}$$

There are only a few steps more until we are able to define the eta term, $\eta(\alpha, r)$. Since $I_1(L)$ has been solved in Equation 45, it is only a matter of algebra to get the following relation:

$$I_1(L)-I_1(0) = -\beta\left(\frac{1}{1+\alpha^2H^2}-\frac{1}{1+\alpha^2(L-H)^2}\right)+ln\left[\frac{1+\alpha^2H^2}{1+\alpha^2(L-H)^2}\right] \tag{61}$$

Substituting Equation 61 into Equation 60 yields,

$$I(L) = \frac{I_0\left(\frac{1+\alpha^2H^2}{1+\alpha^2(L-H)^2}\right)e^{\beta\left(\frac{1}{1+\alpha^2H^2}-\frac{1}{1+\alpha^2(L-H)^2}\right)}}{1+\sigma_{2\phi}NI_0\left[I_2(L)-I_2(0)\right](1+\alpha^2H^2)e^{\beta\left(\frac{1}{1+\alpha^2H^2}\right)}} \tag{62}$$

When we invoke the symmetry property of the experiment, $H = \frac{L}{2}$, Equation 62 reduces to,

$$I(L) = \frac{I_0}{1+\sigma_{2\phi}NI_0\left[I_2(L)-I_2(0)\right]\left(1+\frac{\alpha^2L^2}{4}\right)e^{\beta\left(\frac{1}{1+\frac{\alpha^2L^2}{4}}\right)}} \tag{63}$$

We can now complete the solution by inserting the definition for $I_2(L)$ in Equation 50

$$I_2(L) = \int e^{I_1(L)}dL = \int e^{-\beta\left(\frac{1}{1+\alpha^2(L-H)^2}\right)-ln\left(1+\alpha^2(L-H)^2\right)}dL \tag{64}$$

and

$$I_2(L) = \int e^{I_1(L)} dL = \int \frac{e^{-\beta\left(\frac{1}{1+\alpha^2(L-H)^2}\right)}}{1+\alpha^2(L-H)^2} dL \tag{65}$$

Finally, we can express the complete numerical method as:

$$I(L) = \frac{I_0}{1 + \sigma_{2\phi} N I_0 L \underbrace{\frac{1}{L}\left[\int \frac{e^{-\beta\left(\frac{1}{1+\alpha^2(L-H)^2}\right)}}{1+\alpha^2(L-H)^2} dL\right]\left(1+\frac{\alpha^2 L^2}{4}\right) e^{\beta\left(\frac{1}{1+\frac{\alpha^2 L^2}{4}}\right)}}_{\eta(\alpha,r)}} \tag{66}$$

This eta term can then be conceptually defined as a multiplicative factor to the intensity. Now that we have a better understanding of the Method used to describe the intensity profile, we must now use that function to transform the y-axis in Figure 11 to the TPA unit of $\frac{cm^4}{W}$. This is done by integrating Equation 66 over all r in order to properly model the transmitted power, P_T. The difficulty is the integral that can not be solved analytically. The way we integrated this equation, was by taking the "sum under the curve". This operation was performed in Mathematica and was written as,

$$P_T = 2\pi \int_{-\infty}^{\infty} I(L, r) r dr \tag{67}$$

In essence, the Mathematica code does the same operation to the intensity profile as Equation 67. Specifically however, the code did the following. First of all you will notice that there is an additional $(2\pi r 0.001)$ term. The number is the dr that appears in Equation 67 as well. Next, the $NIntegrate$ command numerically integrates the $I_2(L)$ relation over a span of z from 0 to L. Now, the order of operation is such that the Sum performs a calculation for every value of r from 0 to 0.1 microns in steps of 0.001 microns. This step is the dr that was talked about above. To get the integral over all r, this calculation is performed over a range of r's and is added together

and multiplied by the $2\pi r 0.001$ term. Everytime a calculation is done for an r value, the numerical integral is performed over the range 0 to L in z. Finally, this sum is done for a range of predefined cross-sections, from 0 to 4×10^{-20} $\frac{cm^4}{W}$ in steps of 1×10^{-22} $\frac{cm^4}{W}$. Hundreds of PowerE's are calculated.

The predicted Absorbance, A_{pred}, can now be determined using the two-photon variant of Beer's Law, $A_{pred} = \frac{P_0}{PowerE} - 1$. Where P_0 is simply the power measured just before the test cell. A range of cross-sections were chosen such that the computed range of absorbance values would include the largest absorbance value measured in the experimental data. The range of cross-sections were then plotted against the predicted absorbance values to generate the curve in Figure 32.

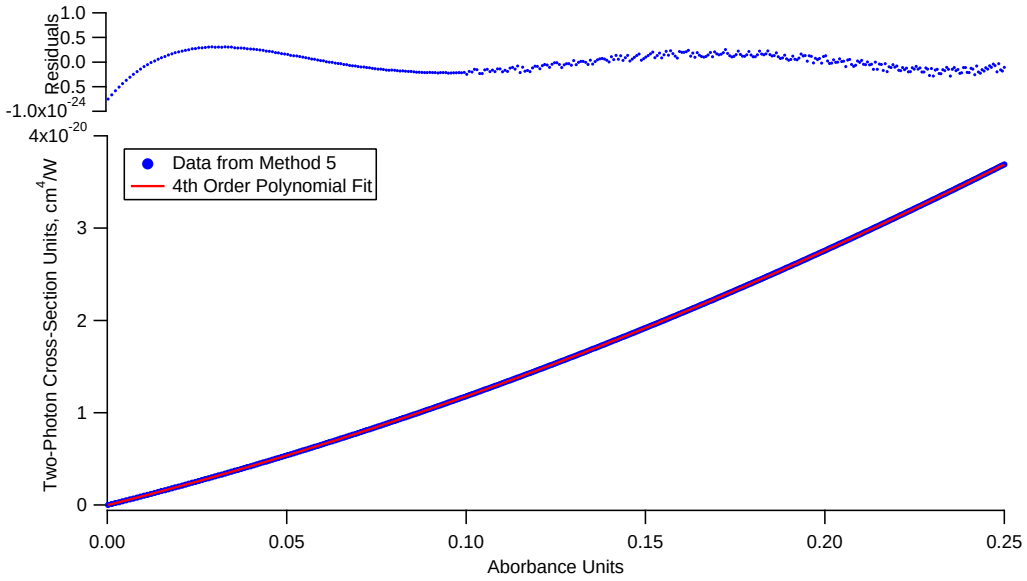

Figure 32. This plot provides the information necessary to generate the function that will transform the experimental absorbance values into two-photon cross-section units.

The resulting function from the fit to this data provided the conversion necessary for the y-axis in Figure 11 to be transformed into TPA cross-section units. The y-axis is now in the proper units, so that the Voigt fit that we have developed will be able to extract the TPA cross-section as the amplitude to the data. This entire process was performed 87 times. Each transformation curve generated from the Mathematica

code was unique for each of the 87 cases. Table 6 lists the five parameters of the fit function for 6 different test cases for comparison.

Table 6. Fit parameters t_x and test conditions for 6 of 87 test cases.

Case	$t_0(10^{-23})$	$t_1(10^{-20})$	$t_2(10^{-20})$	$t_3(10^{-20})$	$t_4(10^{-20})$	N $(10^{15}\frac{atoms}{cm^3})$	P (mW)	f (cm)
1	-2.0866	9.7517	0.2061	-1.335	-3.254	4.066	680	15.24
2	-2.7912	0.1279	0.2690	-94.72	-6.107	1.554	1200	15.24
3	-1.3108	6.5865	0.1405	-1.557	-1.027	4.066	930	15.24
4	-1.4442	4.3683	5.3007	20.22	-35.72	3.123	1200	20.32
5	-0.4894	2.2202	2.7547	-212.5	-846.3	6.124	1200	20.32
6	-2.1502	6.2500	7.5389	43.23	-67.32	4.199	700	20.32

Appendix B. Development of Other Methods to Model the Intensity

Five methods for modeling the intensity were explored. This research first derived the more complete model which was described in Appendix A. However, to better understand the behavior of the two-photon absorption process with a focused beam, and also to provide a logical check to the TPA cross-section extracted from this method, 4 other lower fidelity models were derived.

Model 1: The One-Photon Model.

The first model is using the one-photon Beers Law equation and inserting the relation, $\sigma_{eff} = \sigma_{2\phi} I_0$, to determine the effect on the transmitted intensity. Here σ_{eff} is the effective "one-photon" cross-section in units of cm^2. This method assumes that the pump beam is collimated and is only attenuated by the absorption medium. This is shown in Equation 68 below.

$$Method\ 1: \quad I(L) = I_0 e^{\sigma_{2\phi} I_0 N L} \tag{68}$$

$$dI(z) = \sigma_{1\phi} N I(z) dz \tag{69}$$

$$I(z) = I_0 e^{\sigma_{1\phi} N L} \tag{70}$$

$$dI(z) = \sigma_{2\phi} N I^2(z) dz \tag{71}$$

$$A = \frac{P_0}{P_T} - 1 \tag{72}$$

$$\frac{1}{3}h\nu \tag{73}$$

$$\sigma^{HF}_{1\phi,2\phi}(\nu_0) = \sigma_{1\phi,2\phi}(\nu_0) \sum_{F'} \sum_{F''} \sum_{iso} S_{F''F'} f_B f_{iso} \tag{74}$$

Obviously the more familiar absorbance equation, $-ln\left(\frac{I}{I_0}\right)$, is derived from this form.

Model 2: Two-Photon, No Focus Model.

The second method uses the two-photon Beers Law variant, which originates from the differential form in Equation 10, and assumes a collimated beam. Method 2, then, is just the solution to this differential equation.

$$Method\ 2: \quad I(L) = \frac{I_0}{1 + \sigma_{2\phi} I_0 N L} \tag{75}$$

The next two methods include a model for the focused Gaussian beam.

Model 3: Two-Photon, Focused Beam, $\beta = 0$ Model.

Recall from Appendix A that $\beta = \frac{r^2}{\omega_0^2}$. This model simplifies the complete numerical model from Equation 66 by solving for the intensity only along the optical axis, $r = 0$, or $\beta = 0$. When this is done, the exponential terms disappear and the integral in the denominator becomes analytical.

$$I(L) = \frac{I_0}{1 + \sigma_{2\phi} N I_0 \left[\int \frac{1}{1+\alpha^2(L-H)^2} dL\right] \left(1 + \frac{\alpha^2 L^2}{4}\right)} \tag{76}$$

From any table of integrals, one can find the following integral,

$$\int \frac{1}{ax^2+bx+c}dx = \frac{2}{\sqrt{4ac-b^2}} \arctan\left(\frac{2ax+b}{\sqrt{4ac-b^2}}\right) \tag{77}$$

Therefore, the integral in Equation 76 becomes,

$$\int \frac{1}{1+\alpha^2(L-H)^2}dL = \frac{2}{\sqrt{4(\alpha^2)(\alpha^2H^2+1)-(-2\alpha^2H)^2}} \times \\ \times \arctan\left(\frac{2\alpha^2L+(-2\alpha^2H)}{\sqrt{4(\alpha^2)(\alpha^2H^2+1)-(-2\alpha^2H)^2}}\right) \tag{78}$$

After simplification, we have:

$$I_2(L)^{\beta=0} = \frac{1}{\alpha}\arctan\left[\alpha(L-H)\right] \tag{79}$$

And,

$$I_2(0)^{\beta=0} = \frac{1}{\alpha}\arctan\left[-\alpha H\right] \tag{80}$$

Invoking the symmetry of the experiment ($H = L/2$) we finally have a model for Method 3,

$$Method\ 3: \quad I(L)^{\beta=0} = \frac{I_0}{1+\sigma_{2\phi}NI_0\underbrace{\left\{\frac{2}{\alpha}\left[\arctan\left[\frac{\alpha L}{2}\right]\right]\right\}(1+\frac{\alpha^2L^2}{4})}_{\eta_3(\alpha)}} \tag{81}$$

Model 4: Two-Photon, Unfocused Beam, Average Intensity Model.

A fourth method was chosen to explore the idea that knowing the average intensity through the cell would provide the simplest accurate answer. We start with

Equation 66 from Appendix A. We start by first verifying that the following relation is true:

$$P_T = 2\ \pi \int_0^\infty I(L,r) r\ dr \tag{82}$$

Logically, this statement is true if we can prove the following is also true,

$$P_0 = 2\ \pi \int_0^\infty I(0,r) r\ dr \tag{83}$$

It follows that for a focused Gaussian beam, the intensity behaves as,

$$I(0,r) = \frac{P_0}{\pi\omega^2(0)} e^{-\frac{r^2}{\omega^2(0)}} \tag{84}$$

Therefore,

$$P_0 = 2\ \pi \left(\frac{P_0}{\pi\omega^2(0)}\right) \int_0^\infty e^{-\frac{r^2}{\omega^2(0)}} r\ dr \tag{85}$$

From integral tables we find that,

$$\int_0^\infty x^m e^{-ax^2} dx = \frac{\Gamma\left(\frac{m+1}{2}\right)}{2a\left(\frac{m+1}{2}\right)} \tag{86}$$

Such that,

$$P_0 = 2\ \pi \left(\frac{P_0}{\pi\omega^2(0)}\right) \left(\frac{1}{2\left(\frac{1}{\omega^2(0)}\right)}\right) \tag{87}$$

And finally,

$$P_0 = P_0 \tag{88}$$

Returning to Equation 82, we insert the relation we have for $I(L,r)$ from Equation 66 to get,

$$P_T = 2\ \pi \int_0^\infty \frac{I(0,r)\ r\ dr}{1 + \underbrace{\sigma_{2\phi} NL\ I(0,r) \frac{[I_2(L) - I_2(0)]}{L} e^{-I_1(0)}}_{F}} \tag{89}$$

$$P_T = 2\ \pi \int_0^\infty \frac{1}{1+F}\ I(0,r)\ r\ dr \tag{90}$$

For small σNL, $\frac{1}{1+F} = 1 - F$, so

$$\begin{aligned} P_T &= 2\ \pi \int_0^\infty (1-F)\ I(0,r)\ r\ dr & (91) \\ &= \underbrace{2\ \pi \int_0^\infty I(0,r)\ r\ dr}_{P_0} - 2\ \pi \int_0^\infty F\ I(0,r)\ r\ dr & (92) \end{aligned}$$

Substituting F back in,

$$P_T = P_0 - 2\ \pi \int_0^\infty \left[\sigma_{2\phi} NL\ I(0,r) \frac{[I_2(L) - I_2(0)]}{L} e^{-I_1(0)} \right]\ I(0,r)\ r\ dr \tag{93}$$

Some algebra,

$$\frac{P_T}{P_0} = 1 - \underbrace{\frac{2\ \pi}{P_0} \int_0^\infty \sigma_{2\phi} NL\ I^2(0,r) \frac{[I_2(L) - I_2(0)]}{L} e^{-I_1(0)}\ r\ dr}_{G} \tag{94}$$

Reversing the approximation, $1 - G \approx \frac{1}{1+G}$,

$$\frac{P_T}{P_0} = \frac{1}{1 + \sigma_{2\phi} N L \underbrace{\left\{ \frac{2\ \pi}{P_0} \int_0^\infty I^2(0,r) \frac{[I_2(L) - I_2(0)]}{L} e^{-I_1(0)}\ r\ dr \right\}}_{\bar{I}}} \tag{95}$$

We now turn to solving for $\bar{I}$. This is the average intensity. The average intensity consists of an I^2 term, which we already defined above in Equation 84. With this substitution and expanding out the definition for I_2, we have

$$\bar{I} = \left(\frac{2\pi}{P_0}\right) \left(\frac{P_0^2}{\pi^2 \omega^4(0)}\right) \int_0^\infty e^{-2\left(\frac{r^2}{\omega^2(0)}\right)} \left[\int_0^L \frac{\omega_0^2}{\omega^2(L)} e^{-\frac{r^2}{\omega^2(L)}} \frac{dL'}{L} \right] \frac{\omega^2(0)}{\omega_0^2} e^{\frac{r^2}{\omega^2(0)}}\ r\ dr \tag{96}$$

Combining the exponents, switching the order of integration and careful algebra leads to the following relation for the average intensity,

$$\bar{I} = \frac{P_0}{\pi \omega^2(0)} \int_0^L \frac{1}{2 + \alpha^2 (L - H)^2} \frac{dL'}{L} \tag{97}$$

If we let $y^2 = \alpha^2 (L - H)^2$, then we can arrive at the following,

$$\bar{I} = \frac{P_0}{\pi \omega^2(0)} \frac{1}{\alpha\ L} \int_{-\frac{\alpha\ L}{2}}^{\frac{\alpha\ L}{2}} \frac{dy}{2 + y^2} \tag{98}$$

This integral can now be solved and we arrive at our final form for the average intensity,

$$\bar{I} = \frac{P_0}{\pi \omega^2(0)} \frac{\sqrt{2}}{\alpha\ L} \left[\arctan\left(\frac{\alpha\ L}{2\sqrt{2}} \right) \right] \tag{99}$$

Inserting Equation 99 into Equation 95,

$$P_T = \frac{P_0}{1 + \sigma_{2\phi} N L \underbrace{\frac{P_0}{\pi\omega^2(0)}}_{I_0} \frac{\sqrt{2}}{\alpha\ L} \left[\arctan\left(\frac{\alpha\ L}{2\sqrt{2}}\right)\right]} \tag{100}$$

We simply divide both sides by the area, $\pi\omega^2(0)$, to put this in terms of intensity and arrive at the fourth and final intensity model:

$$Method\ 4: \quad I(L) = \frac{I_0}{1 + \sigma_{2\phi} N L\ I_0 \underbrace{\frac{\sqrt{2}}{\alpha\ L}\left[\arctan\left(\frac{\alpha\ L}{2\sqrt{2}}\right)\right]}_{\eta_4(\alpha)}} \tag{101}$$

The average intensity accounts for the focused beam by averaging the intensity profile to one value throughout the length of the test cell. Although this averaging allows for an analytical form that can be easily visualized, this model sorely underestimates the absorbance value which in turn underestimates the TPA cross-section value. This is clearly shown in Figures 33 and 34.

Comparing Methods.

Figures 33 and 34 are much like Figure 16, but now we include Methods 3 and 4. The two figures share the same trends, except for when Method 5 crosses above and then below Methods 1 and 2 for the $\alpha = 0.555$ case in Figure 33. We see in both figures that Method 3 grossly overestimates the cross-section. Recall that this method only solves for the intensity along the optical axis ($\beta = 0$), so it uses only the max value for the intensity all along the test cell. There is no point at which this method is a good approximation. It was surprising that this method was so divergent from the rest, although since the second-order absorption term goes as I^2, we can understand where the sensitivity in I comes from. Method 4 was the average intensity model. Here we see that the model grossly underestimates the TPA cross-

section. For very low absorbance values (For A less than 0.03), this method is a crude yet acceptable approximation, however, it quickly diverges as absorbance increases. This analysis proves the importance of having an accurate model of the spatial profile for the intensity.

It is also important to note that as $\alpha \longrightarrow 0$, i.e. as the beam becomes more collimated, Methods 1,2,4 & 5 diverge more greatly. Perhaps the radial component of the intensity profile becomes a more significant factor in these limits.

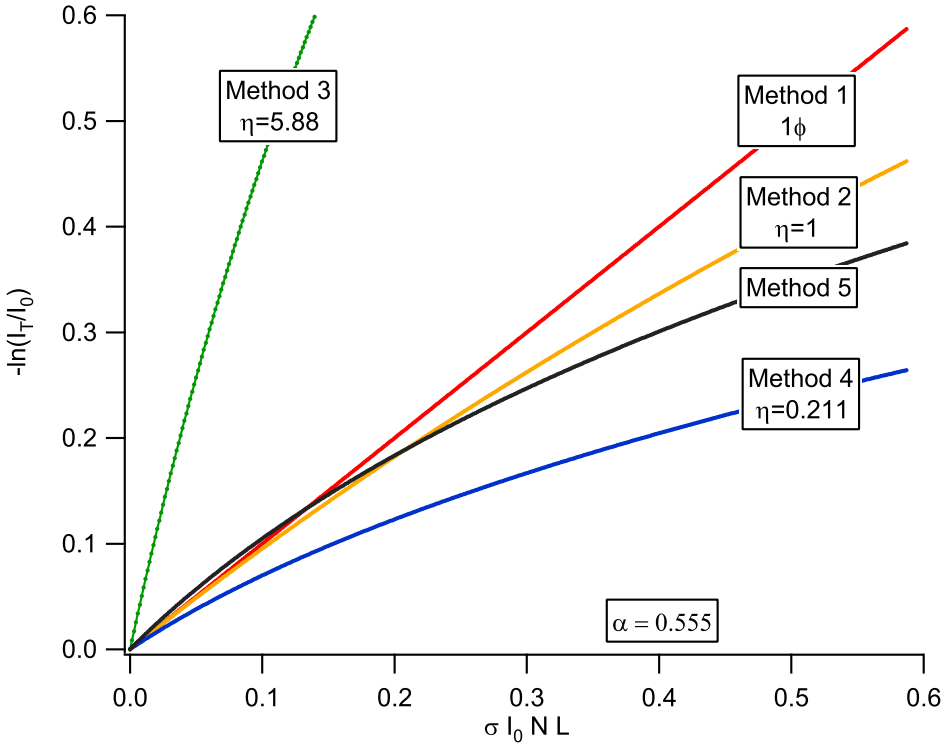

Figure 33. The five methods compared against Method 1, the one-photon Beer's Law description of the two-photon absorption process.

Table 7 lists the eta factors for each of the TPA models. Two focal lengths were used in the experiment and so two beam waists ($\omega \sim \frac{1}{\alpha}$) yielded two values for α.

Finally, Figure 35 is similar to Figure 18 but includes the average intensity prediction for the TPA cross-section. It is important to note that the more complete numerical method has less of a statistical scatter than the average intensity method.

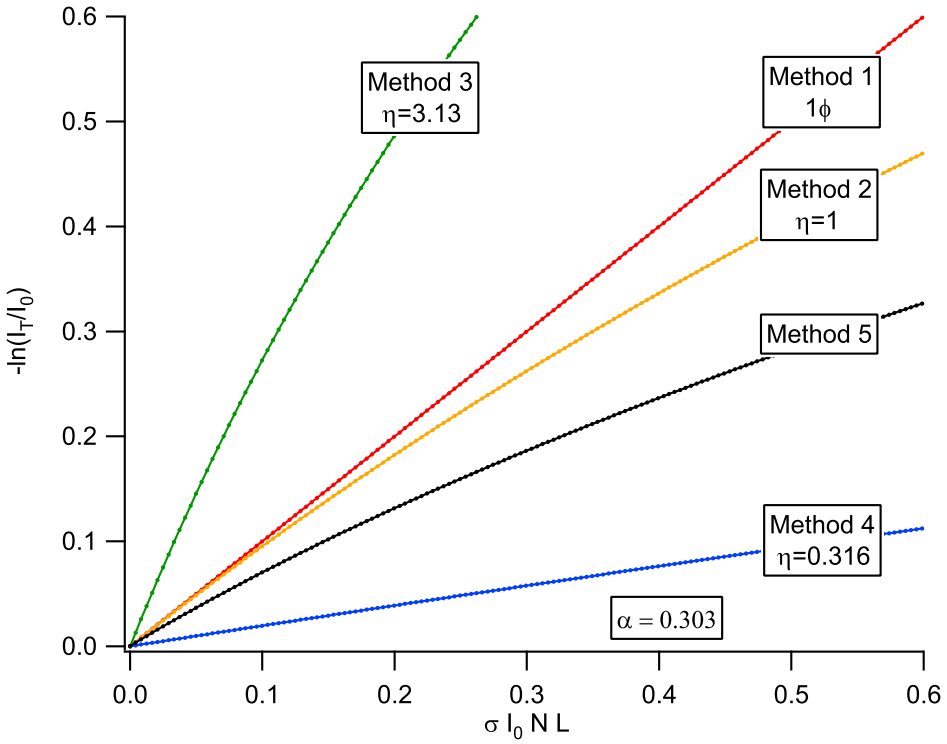

Figure 34. The five methods compared against Method 1, the one-photon Beer's Law description of the two-photon absorption process.

This provided another benchmark pointing to the accuracy of our numerical method.

Table 7. Comparing the η's from the different methods.

Method	Symbol	Relation	$\alpha = 0.555$	$\alpha = 0.303$
2	$\eta_2(\alpha)$	$\eta_2(\alpha)$	1	1
3	$\eta_3(\alpha)$	$\left[\frac{2}{\alpha L} ArcTan\left(\frac{\alpha L}{2}\right)\right]\left(1+\frac{\alpha^2 L^2}{4}\right)$	5.88	3.13
4	$\eta_4(\alpha)$	$\frac{\sqrt{2}}{\alpha L} ArcTan\left(\frac{\alpha L}{2\sqrt{2}}\right)$	0.211	0.316
5	$\eta_5(r,\alpha)$	$\frac{1}{L}\left(\int \frac{e^{-\frac{r^2}{\omega_0^2}\left(\frac{1}{1+\alpha^2(z-\frac{L}{2})^2}\right)}}{1+\alpha^2(z-\frac{L}{2})^2}\right)(1+\frac{\alpha^2 L^2}{4}) e^{\frac{r^2}{\omega_0^2}\left(\frac{1}{1+\frac{\alpha^2 L^2}{4}}\right)}$	See Figure 14	

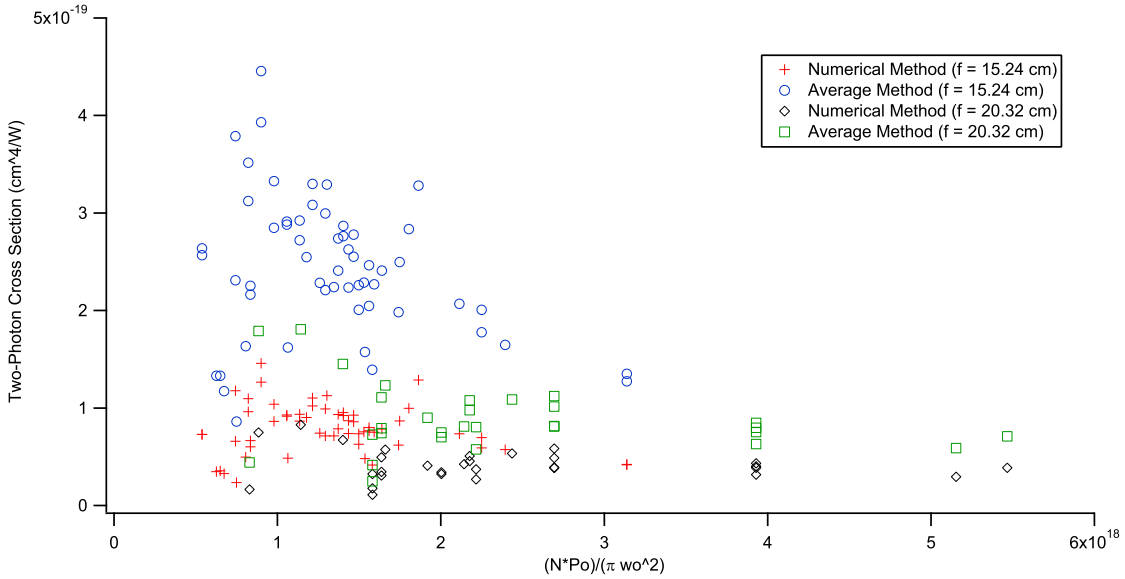

Figure 35. All 87 cross-section values for both the numerical method and the average intensity method. It is clear that the complete numerical method generates a more accurate result. The statistical spread for the average intensity model is about twice as large as the numerical method.

Appendix C. All 87 Test Results

This study collected data from 87 test configurations by varying alkali concentration, pump laser power and beam waist. Table 8 displays all of the doppler-broadened cross-sections, it's error bound, the alkali concentration, the pump power measured just before entering the optical beam train and the beam waist. The right-most column references the corresponding figure that displays the transformed data that was fitted with the Voigt model further below in this appendix.

Table 8. All of the 87 Doppler-Broadened Two-Photon Absorption Cross-Sections Measured for the $5^2S_{1/2} \longrightarrow 5^2D_{5/2}$ Transition in Rb.

$\sigma_{2\phi}$ $\times 10^{-21}$ $\frac{cm^4}{W}$	Error $\pm \times 10^{-23}$ $\frac{cm^4}{W}$	N $\times 10^{15}$ $\frac{atoms}{cm^3}$	P_0 mW	ω_0 μm	Figure
2.29	0.56	1.86	1200	69.7	36
6.05	0.66	3.81	1200	69.7	37
5.23	0.52	3.81	1230	69.7	38
7.81	0.99	4.20	1230	69.7	39
5.25	1.02	7.57	1230	69.7	40
5.32	0.99	7.57	1230	69.7	41
4.49	0.45	1.61	1200	69.7	42
4.37	0.64	1.55	1200	69.7	43
4.12	0.73	1.67	1200	69.7	44
6.24	0.89	2.00	1200	69.7	45
8.39	1.40	2.07	1200	69.7	46
7.58	0.91	2.07	1200	69.7	47
11.4	2.89	2.92	1200	69.7	48
14.2	0.84	3.23	1200	69.7	49
9.35	1.14	3.13	1200	69.7	50

12.6	1.07	4.48	1200	69.7	51
10.9	2.58	4.34	1200	69.7	52
16.2	1.31	4.62	1200	69.7	53
7.22	2.09	5.94	1200	69.7	54
9.27	2.26	5.25	1200	69.7	55
7.44	0.65	5.58	1200	69.7	56
8.77	1.02	5.58	1200	69.7	57
6.11	1.04	2.64	1200	69.7	58
8.98	1.17	3.34	1200	69.7	59
9.89	1.13	4.07	1200	69.7	60
9.47	1.56	4.07	1170	69.7	61
9.66	1.51	4.07	1150	69.7	62
10.1	1.31	4.07	1150	69.7	63
9.52	1.34	4.07	1130	69.7	64
7.93	1.51	4.07	1110	69.7	65
9.26	1.36	4.07	1110	69.7	66
11.7	1.55	4.07	1090	69.7	67
10.8	1.74	4.07	1090	69.7	68
10.9	1.59	4.07	1070	69.7	69
9.28	2.22	4.07	1070	69.7	70
11.6	1.45	4.07	1050	69.7	71
12.0	1.54	4.07	1050	69.7	72
9.92	1.35	4.07	1030	69.7	73
11.8	2.58	4.07	1030	69.7	74
12.5	1.26	4.07	980	69.7	75
8.99	1.59	4.07	980	69.7	76

13.9	1.34	4.07	930	69.7	77
12.9	1.40	4.07	930	69.7	78
11.8	1.27	4.07	880	69.7	79
10.9	1.37	4.07	880	69.7	80
11.5	1.56	4.07	830	69.7	81
11.7	1.35	4.07	830	69.7	82
10.9	1.30	4.07	780	69.7	83
13.1	1.54	4.07	780	69.7	84
18.4	2.34	4.07	730	69.7	85
15.9	5.14	4.07	730	69.7	86
13.8	1.59	4.07	680	69.7	87
12.1	1.46	4.07	680	69.7	88
14.8	2.22	4.07	630	69.7	89
8.31	1.35	4.07	630	69.7	90
9.19	1.60	4.07	500	69.7	91
9.19	1.47	4.07	500	69.7	92
1.39	0.31	2.46	1200	94.4	93
4.06	0.41	2.46	1200	94.4	94
2.23	0.34	2.46	1200	94.4	95
3.38	0.42	3.45	1200	94.4	96
4.68	0.40	3.45	1200	94.4	97
4.83	0.57	4.20	1200	94.4	98
4.93	0.73	4.20	1200	94.4	99
6.14	0.63	4.20	1200	94.4	100
4.87	0.49	6.12	1200	94.4	101
3.99	0.76	6.12	1200	94.4	102

5.45	0.76	6.12	1200	94.4	103
5.05	0.34	6.12	1200	94.4	104
4.86	0.32	8.52	1200	94.4	105
3.72	0.61	8.03	1200	94.4	106
2.09	0.80	1.29	1200	94.4	107
6.21	2.34	2.55	1200	94.4	108
4.35	0.85	2.55	1200	94.4	109
3.88	0.58	2.55	1200	94.4	110
4.28	0.51	3.12	1200	94.4	111
4.08	0.76	3.12	1200	94.4	112
5.33	0.84	3.34	1200	94.4	113
7.35	0.59	4.20	1200	94.4	114
6.72	0.53	4.20	1200	94.4	115
6.39	1.14	4.20	1200	94.4	116
5.73	0.92	4.20	1200	94.4	117
5.16	0.83	4.20	1200	94.4	118
7.22	1.13	4.20	1200	94.4	119
8.47	1.15	4.20	1200	94.4	120
10.4	1.99	4.20	1200	94.4	121
9.44	1.71	4.20	1200	94.4	122

The following are the 87 absorption features with transformed y-axis and Voigt model fits. Please note that the order of the peaks is dependent on whether the pump laser scanned up or down in frequency. As an example, Figures 36 and 37 have peak #1 (please refer back to Figure 11) in different locations. Since this work was not concerned with absolute frequency position, no care was taken to standardize the

plots in this regard.

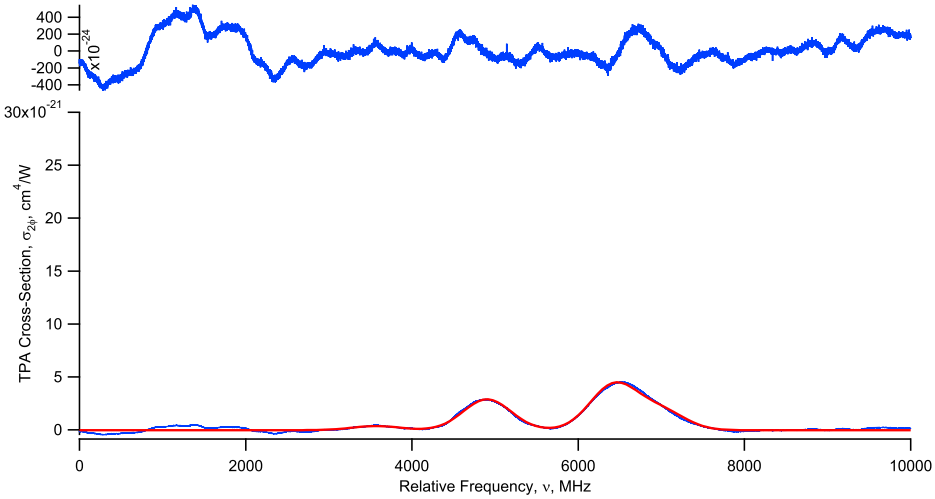

Figure 36. $\sigma_{2\phi} = 2.96 \times 10^{-21} \frac{cm^4}{W}$.

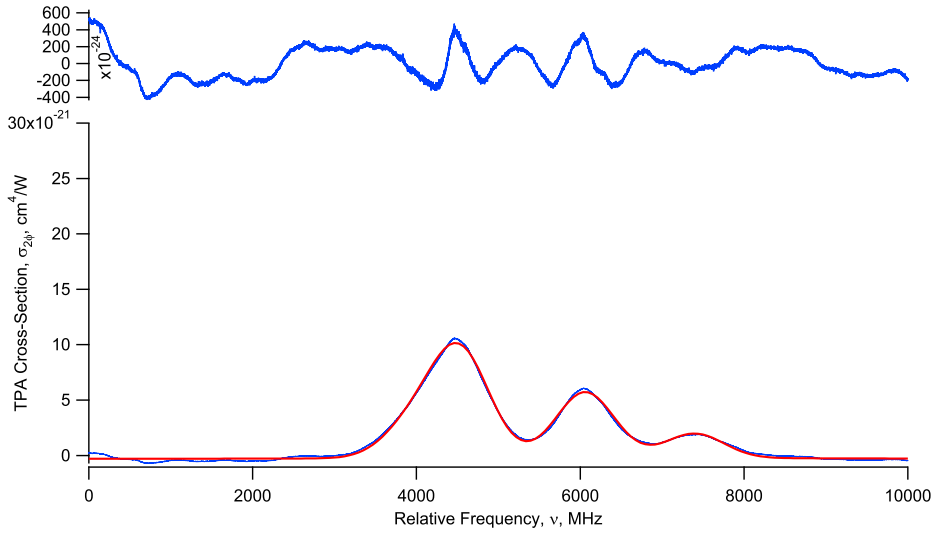

Figure 37. $\sigma_{2\phi} = 6.05 \times 10^{-21} \frac{cm^4}{W}$.

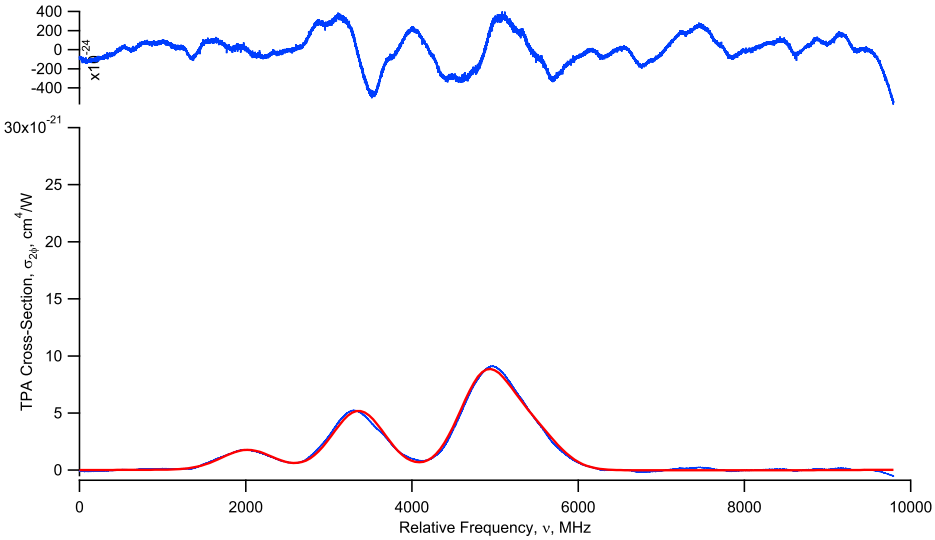

Figure 38. $\sigma_{2\phi} = 5.23 \times 10^{-21} \frac{cm^4}{W}$.

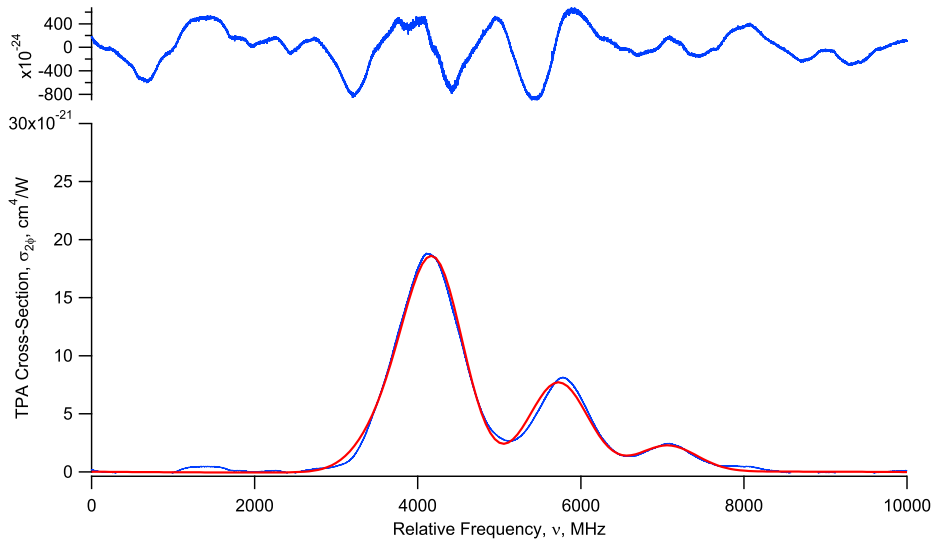

Figure 39. $\sigma_{2\phi} = 7.81 \times 10^{-21} \frac{cm^4}{W}$.

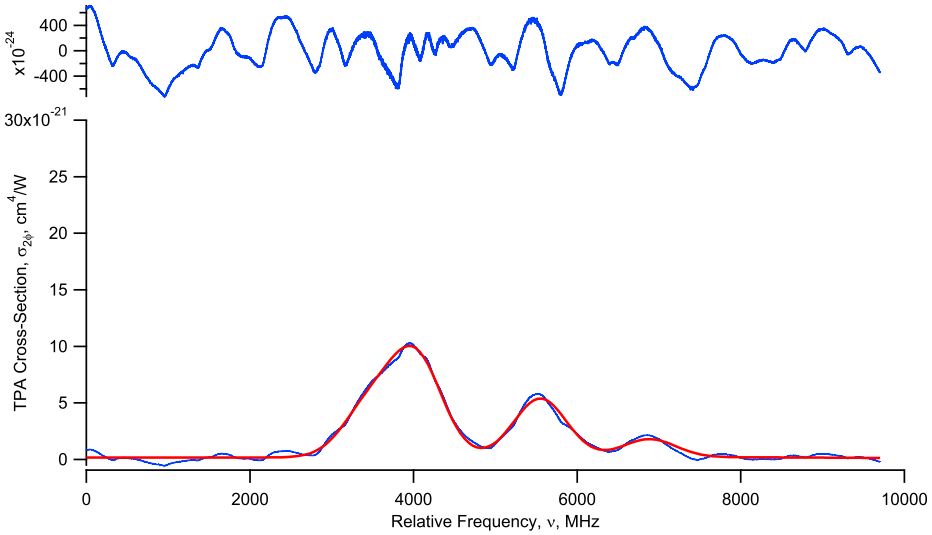

Figure 40. $\sigma_{2\phi} = 5.25 \times 10^{-21} \frac{cm^4}{W}$.

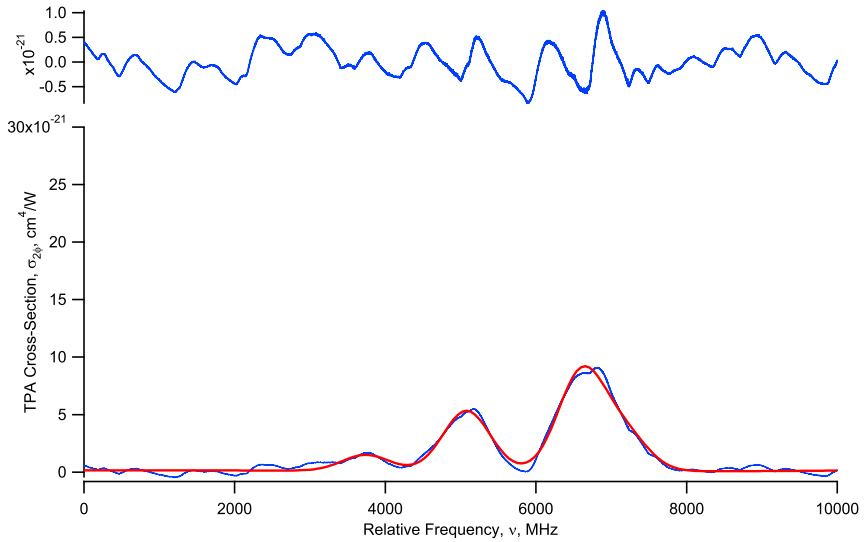

Figure 41. $\sigma_{2\phi} = 5.32 \times 10^{-21} \frac{cm^4}{W}$.

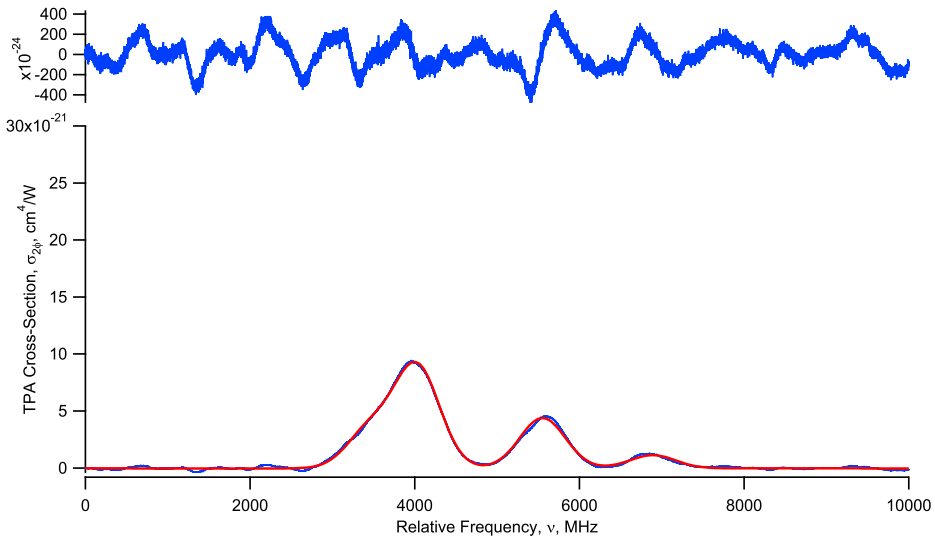

Figure 42. $\sigma_{2\phi} = 4.49 \times 10^{-21} \frac{cm^4}{W}$.

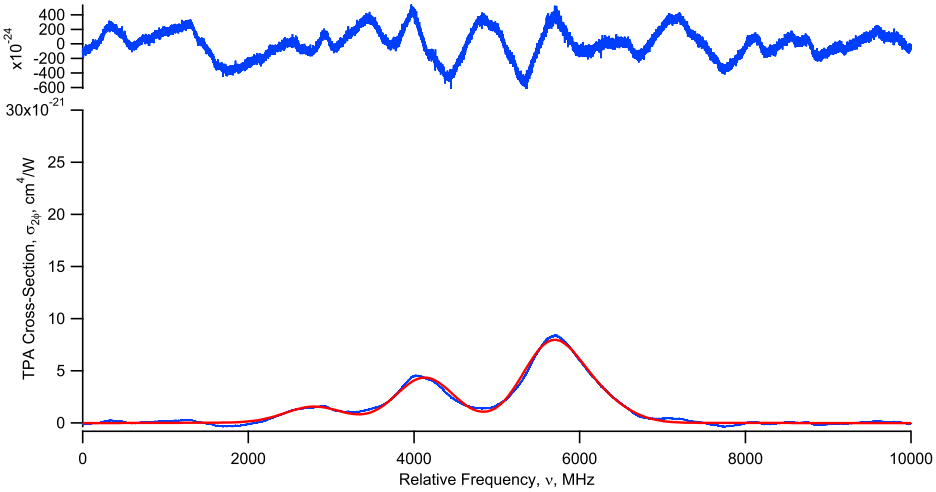

Figure 43. $\sigma_{2\phi} = 4.37 \times 10^{-21} \frac{cm^4}{W}$.

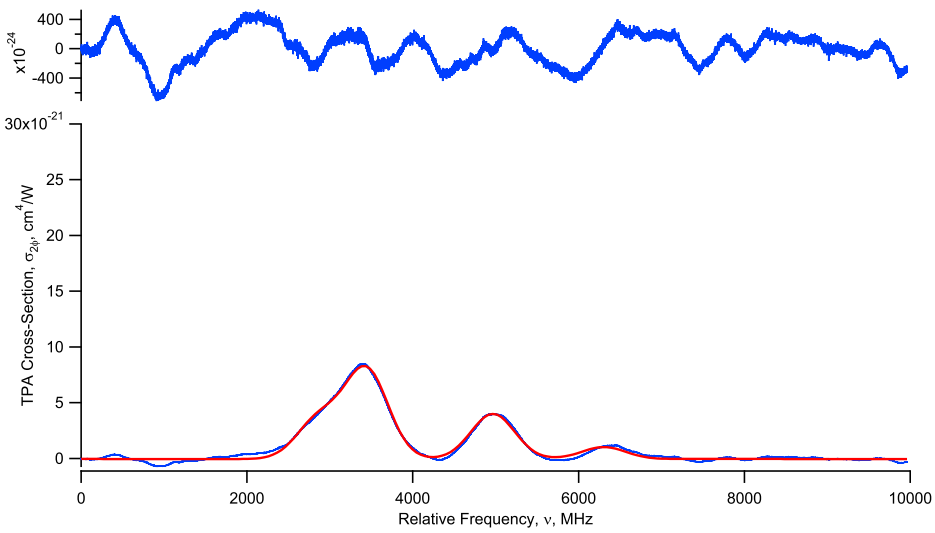

Figure 44. $\sigma_{2\phi} = 4.12 \times 10^{-21} \frac{cm^4}{W}$.

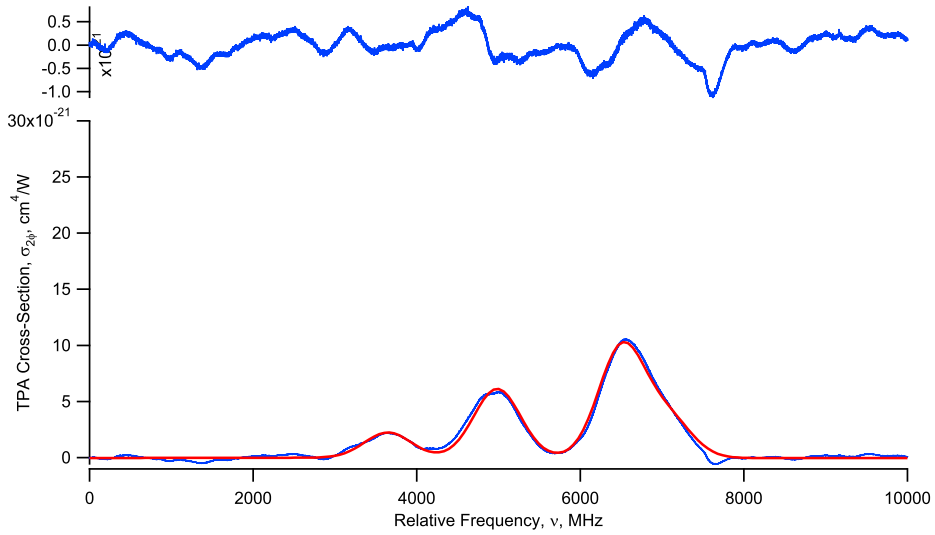

Figure 45. $\sigma_{2\phi} = 6.24 \times 10^{-21} \frac{cm^4}{W}$.

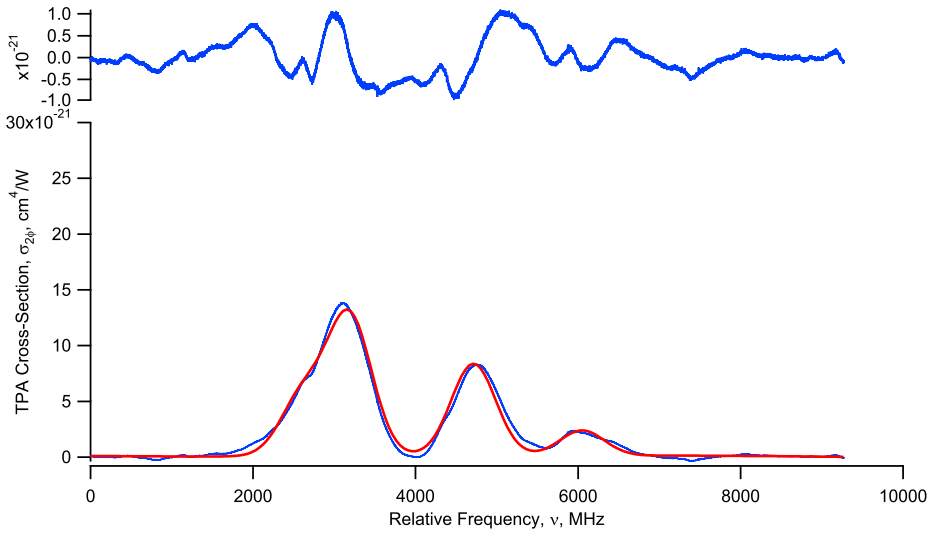

Figure 46. $\sigma_{2\phi} = 8.39 \times 10^{-21} \frac{cm^4}{W}$.

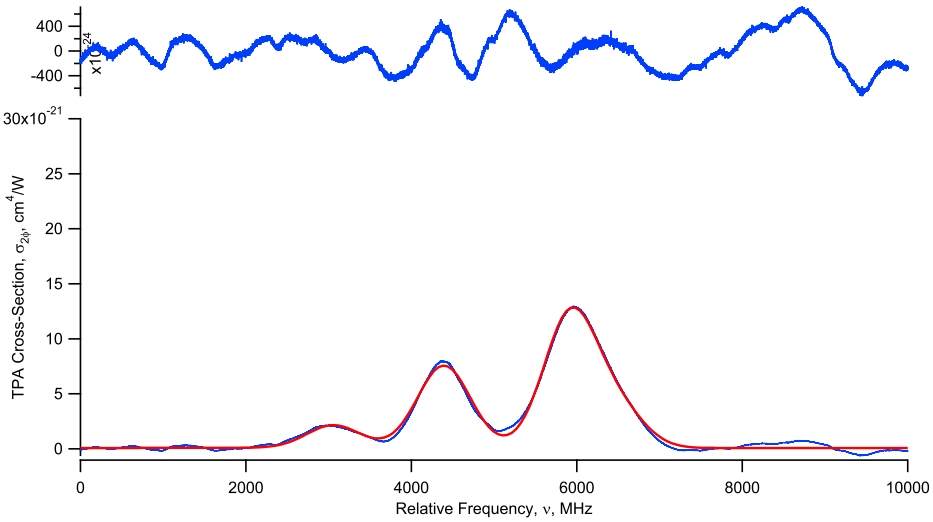

Figure 47. $\sigma_{2\phi} = 7.58 \times 10^{-21} \frac{cm^4}{W}$.

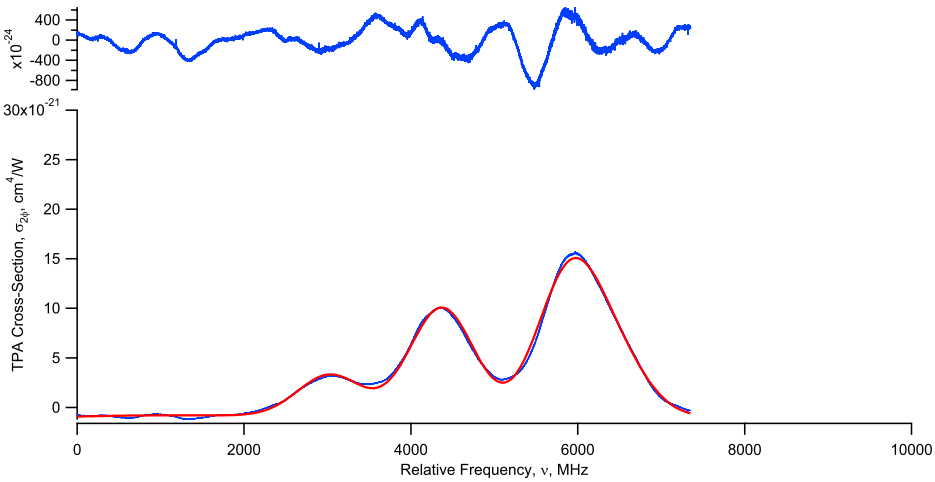

Figure 48. $\sigma_{2\phi} = 1.14 \times 10^{-20} \frac{cm^4}{W}$.

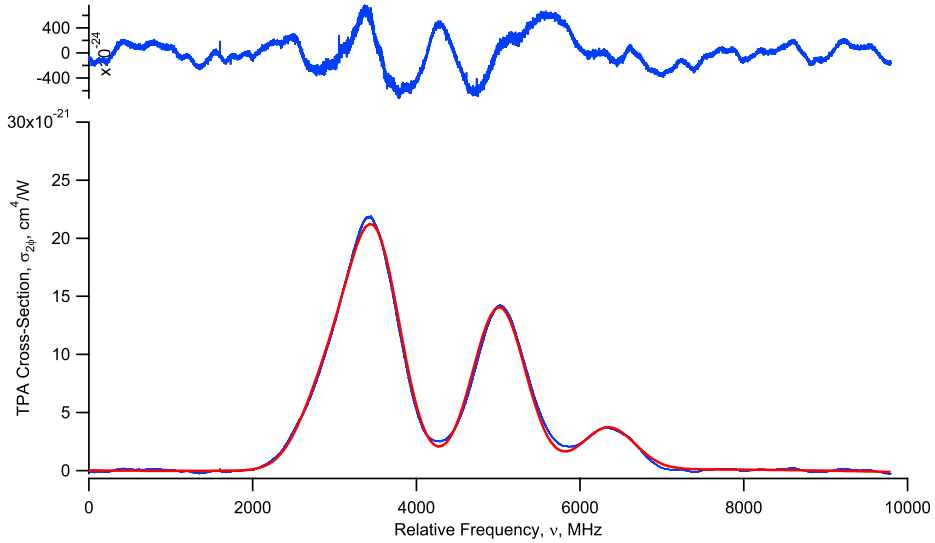

Figure 49. $\sigma_{2\phi} = 1.42 \times 10^{-20} \frac{cm^4}{W}$.

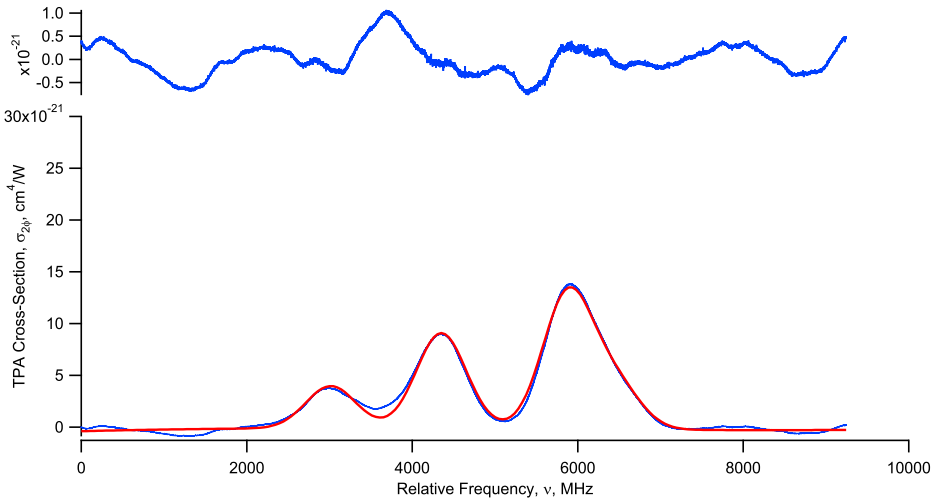

Figure 50. $\sigma_{2\phi} = 9.35 \times 10^{-21} \frac{cm^4}{W}$.

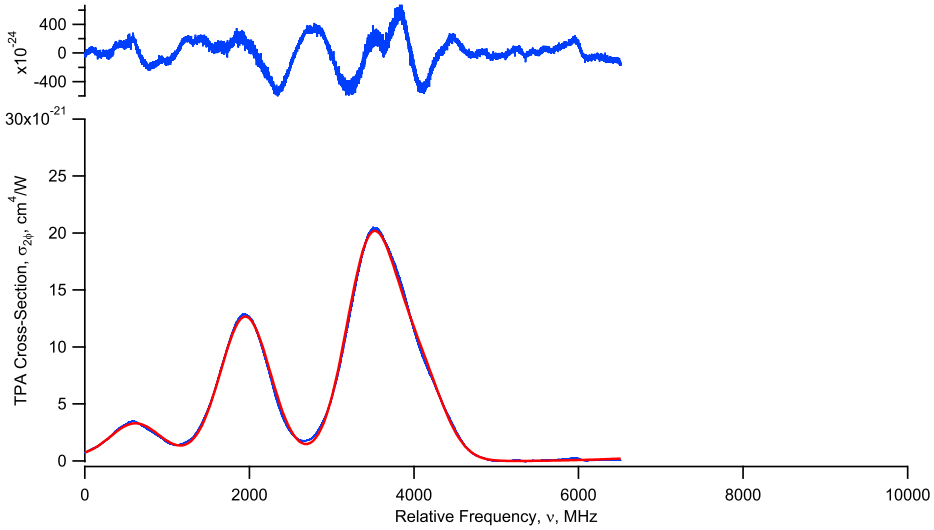

Figure 51. $\sigma_{2\phi} = 1.26 \times 10^{-20} \frac{cm^4}{W}$.

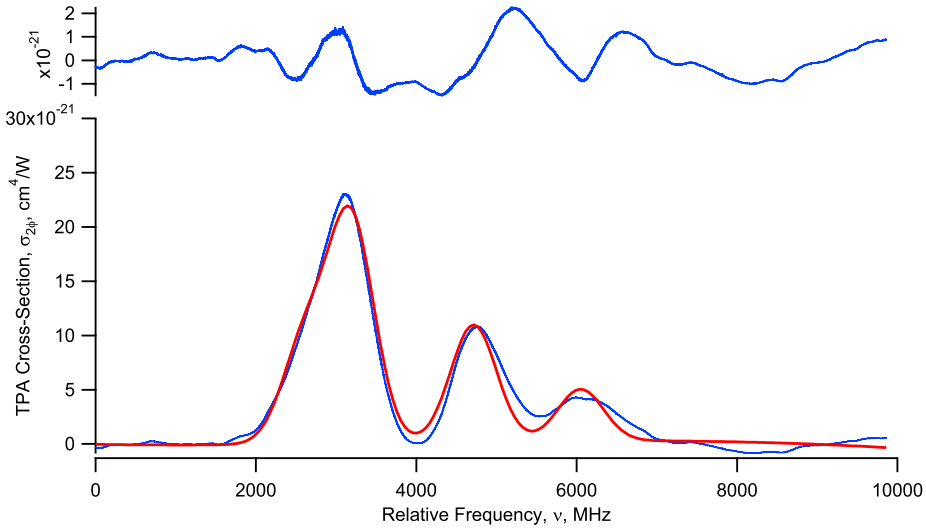

Figure 52. $\sigma_{2\phi} = 1.09 \times 10^{-20} \frac{cm^4}{W}$.

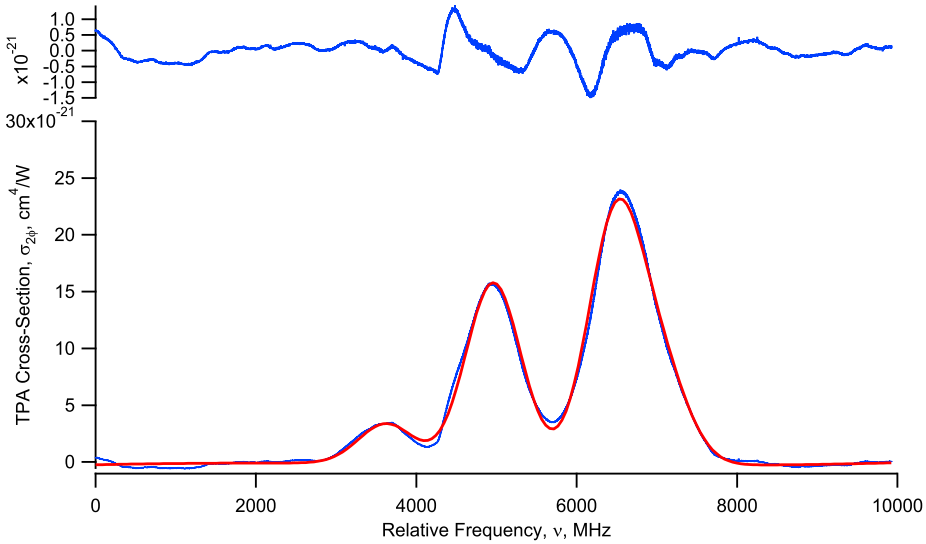

Figure 53. $\sigma_{2\phi} = 1.62 \times 10^{-20} \frac{cm^4}{W}$.

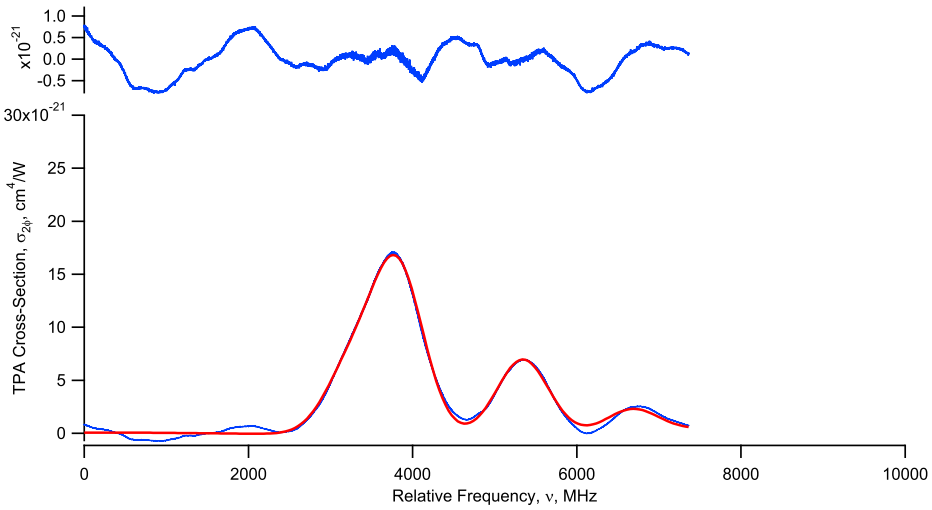

Figure 54. $\sigma_{2\phi} = 7.22 \times 10^{-21} \frac{cm^4}{W}$.

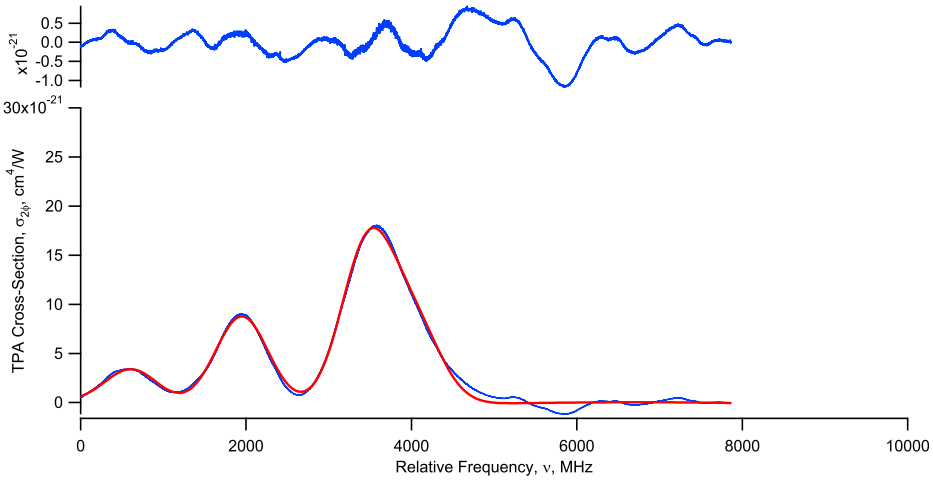

Figure 55. $\sigma_{2\phi} = 9.27 \times 10^{-21} \frac{cm^4}{W}$.

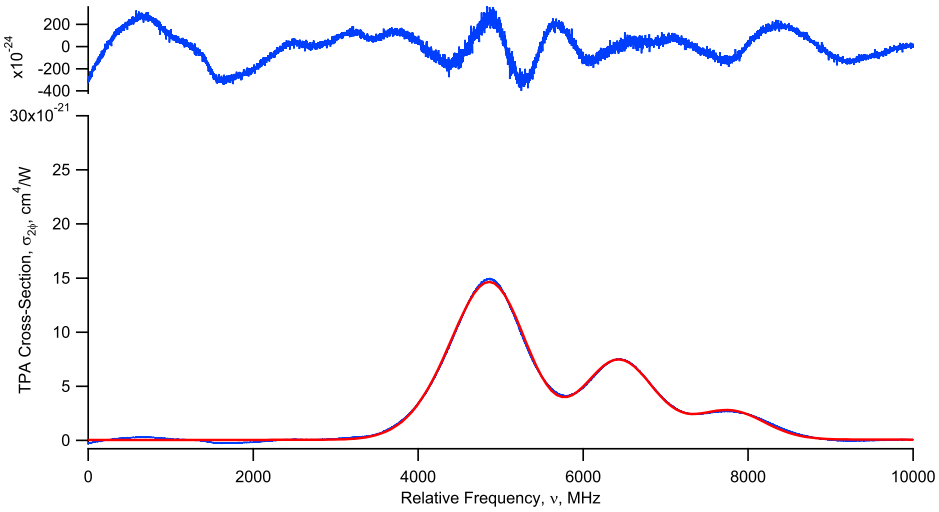

Figure 56. $\sigma_{2\phi} = 7.44 \times 10^{-21} \frac{cm^4}{W}$.

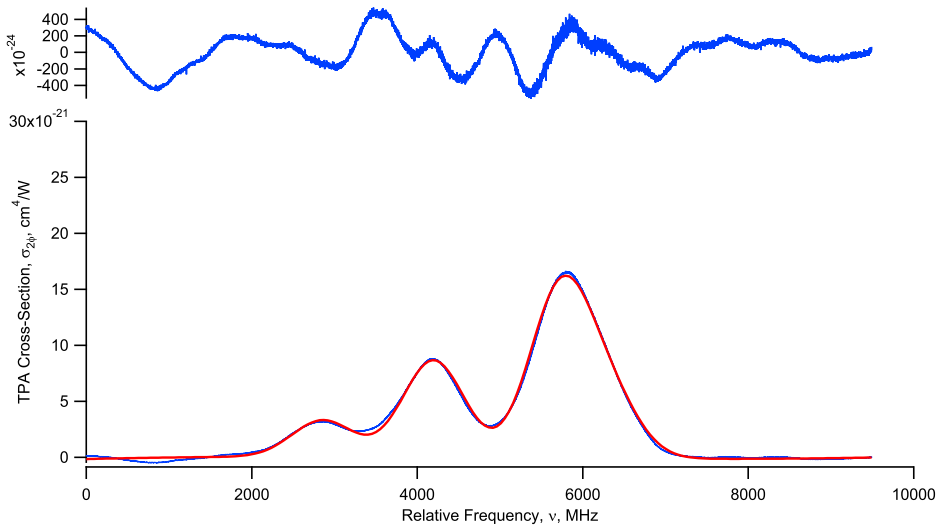

Figure 57. $\sigma_{2\phi} = 8.77 \times 10^{-21} \frac{cm^4}{W}$.

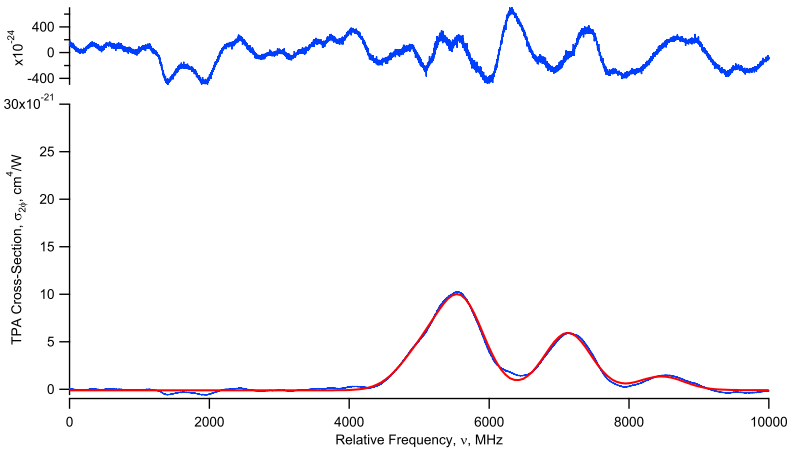

Figure 58. $\sigma_{2\phi} = 6.11 \times 10^{-21} \frac{cm^4}{W}$.

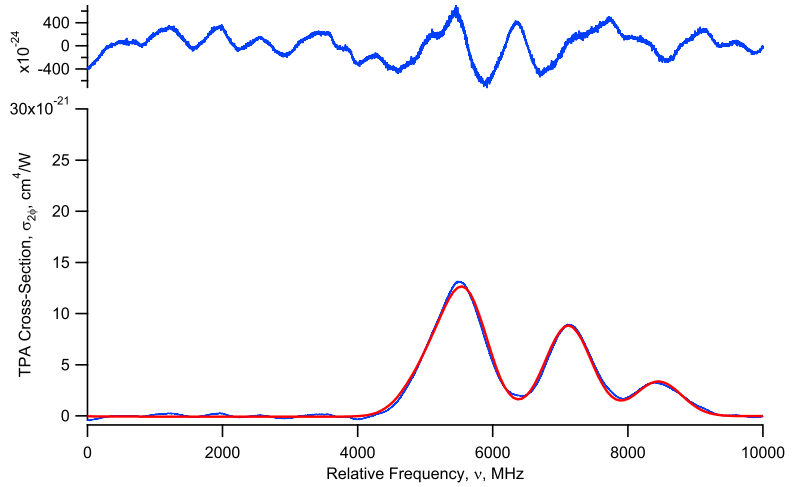

Figure 59. $\sigma_{2\phi} = 8.98 \times 10^{-21} \frac{cm^4}{W}$.

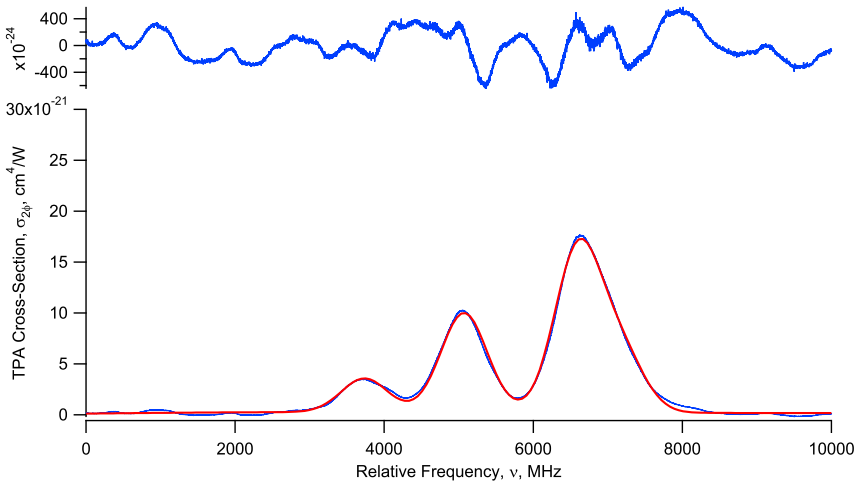

Figure 60. $\sigma_{2\phi} = 9.89 \times 10^{-21} \frac{cm^4}{W}$.

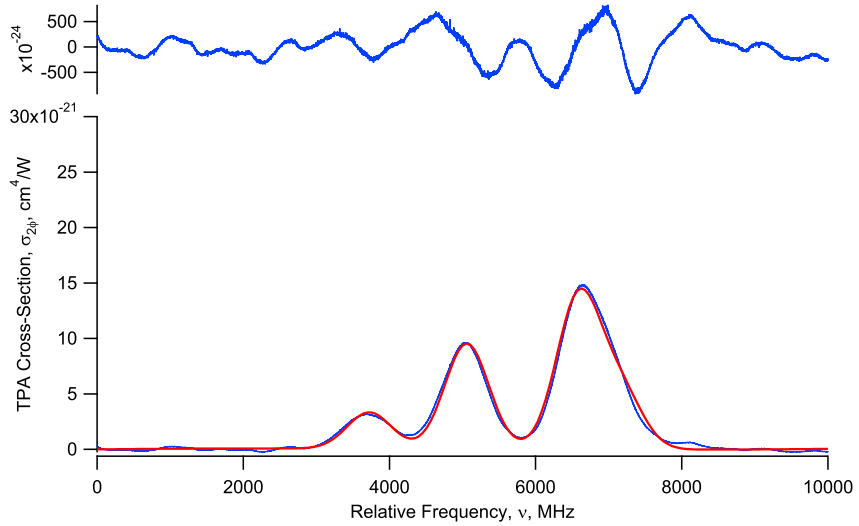

Figure 61. $\sigma_{2\phi} = 9.47 \times 10^{-21} \frac{cm^4}{W}$.

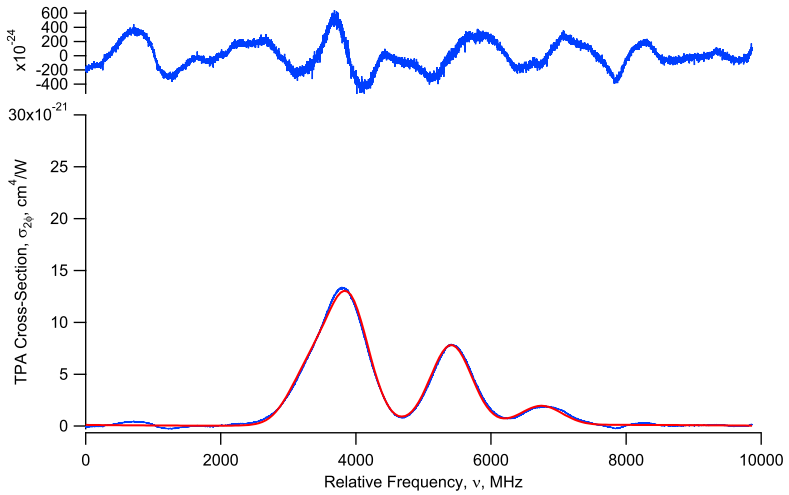

Figure 62. $\sigma_{2\phi} = 9.66 \times 10^{-21} \frac{cm^4}{W}$.

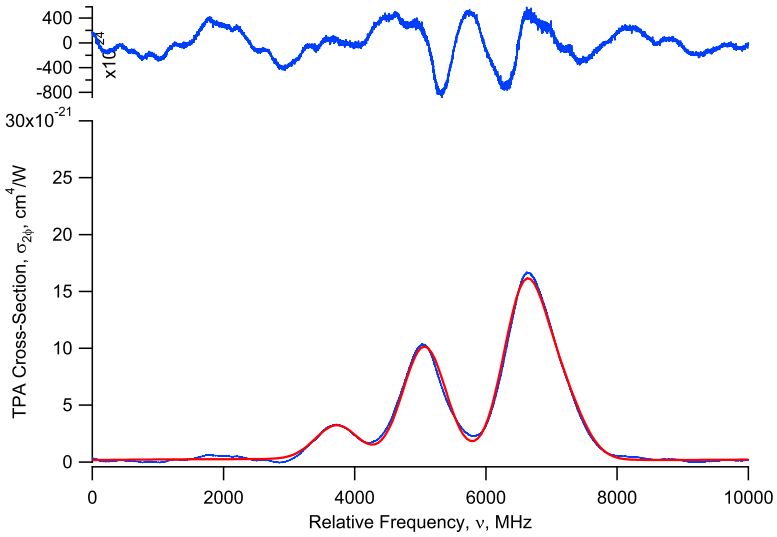

Figure 63. $\sigma_{2\phi} = 1.01 \times 10^{-20} \frac{cm^4}{W}$.

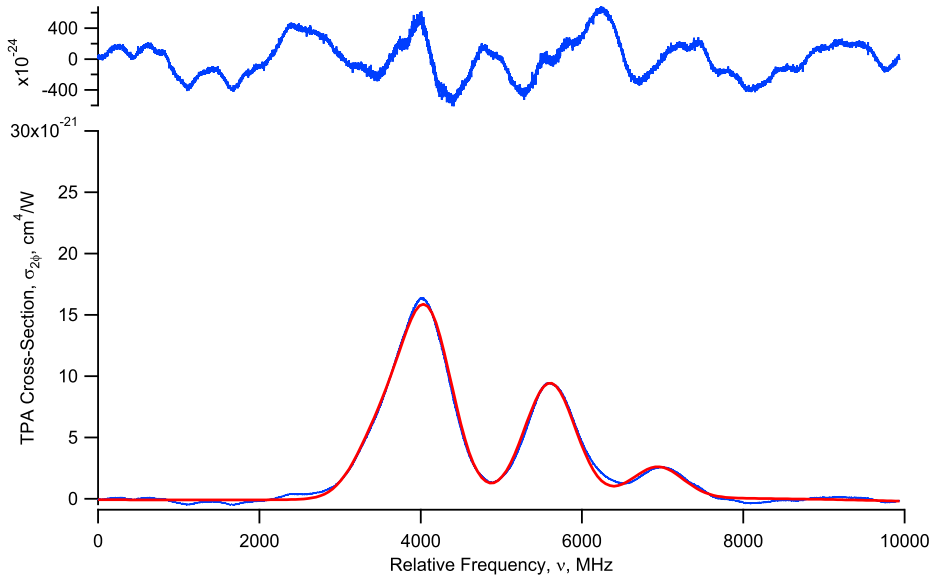

Figure 64. $\sigma_{2\phi} = 9.52 \times 10^{-21} \frac{cm^4}{W}$.

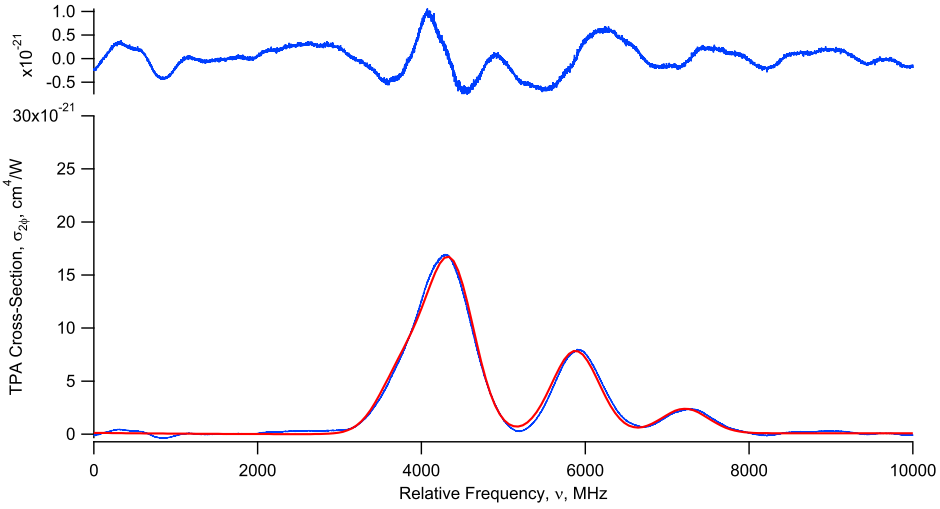

Figure 65. $\sigma_{2\phi} = 7.93 \times 10^{-21} \frac{cm^4}{W}$.

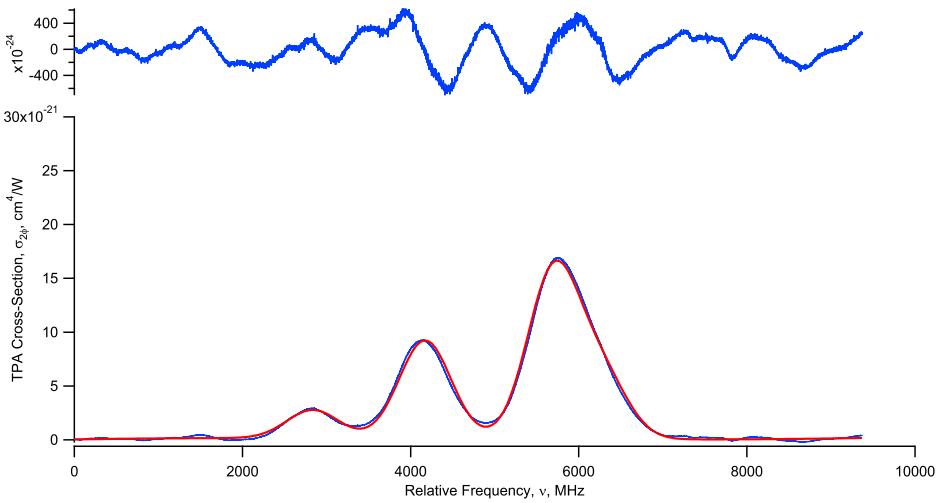

Figure 66. $\sigma_{2\phi} = 9.26 \times 10^{-21} \frac{cm^4}{W}$.

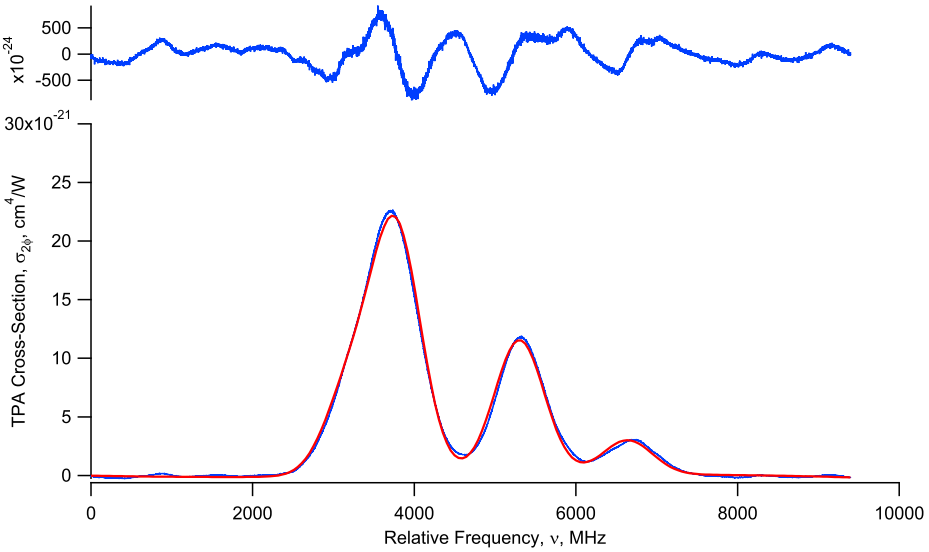

Figure 67. $\sigma_{2\phi} = 1.17 \times 10^{-20} \frac{cm^4}{W}$.

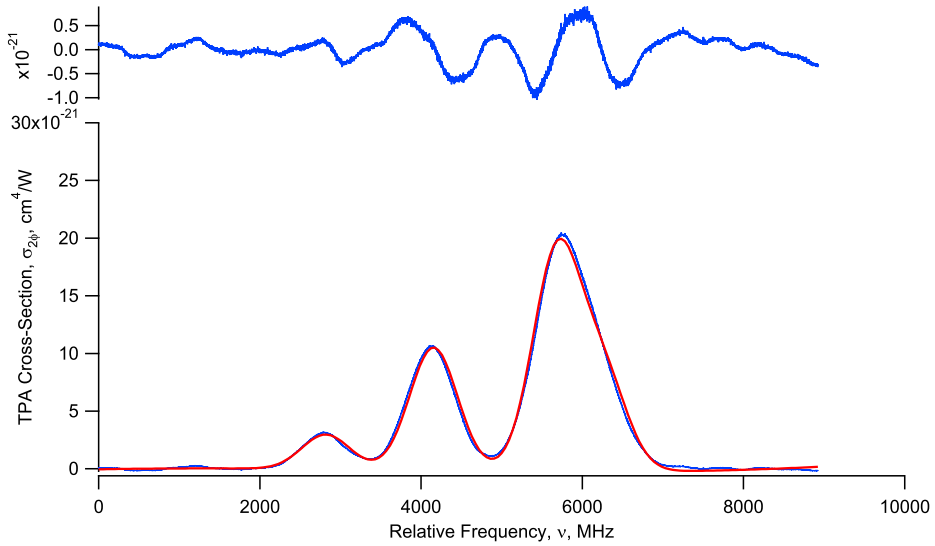

Figure 68. $\sigma_{2\phi} = 1.08 \times 10^{-20} \frac{cm^4}{W}$.

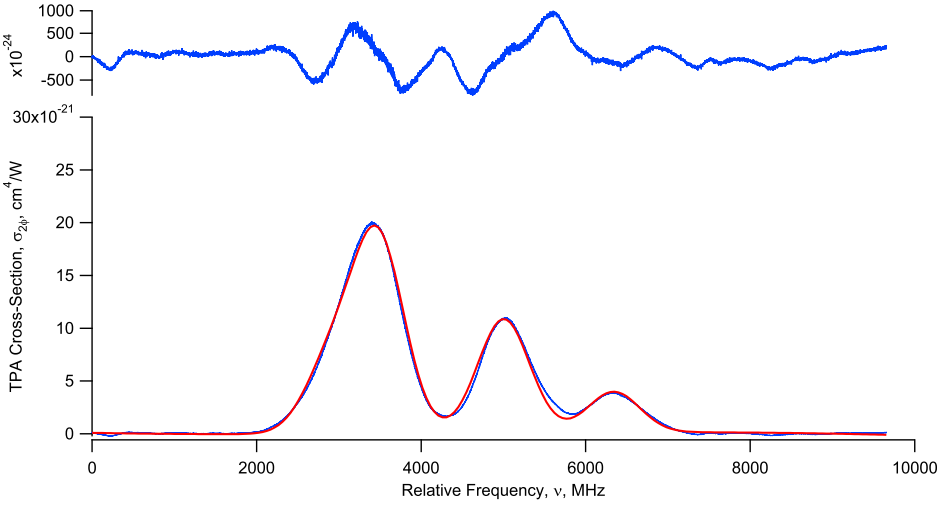

Figure 69. $\sigma_{2\phi} = 1.09 \times 10^{-20} \frac{cm^4}{W}$.

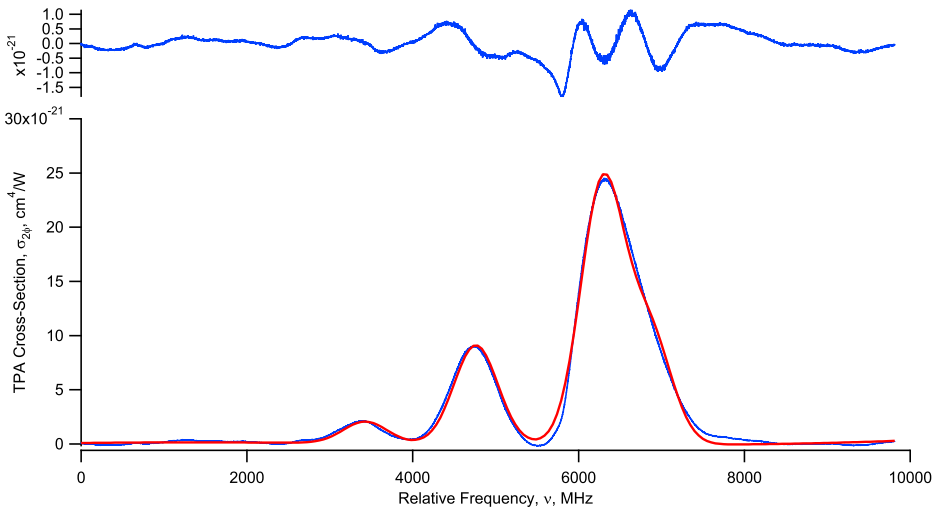

Figure 70. $\sigma_{2\phi} = 9.28 \times 10^{-21} \frac{cm^4}{W}$.

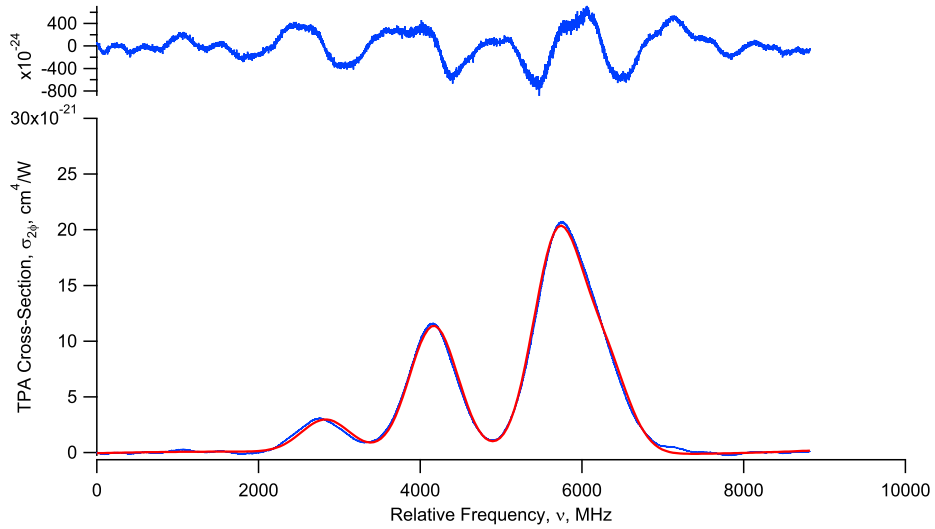

Figure 71. $\sigma_{2\phi} = 1.16 \times 10^{-20} \frac{cm^4}{W}$.

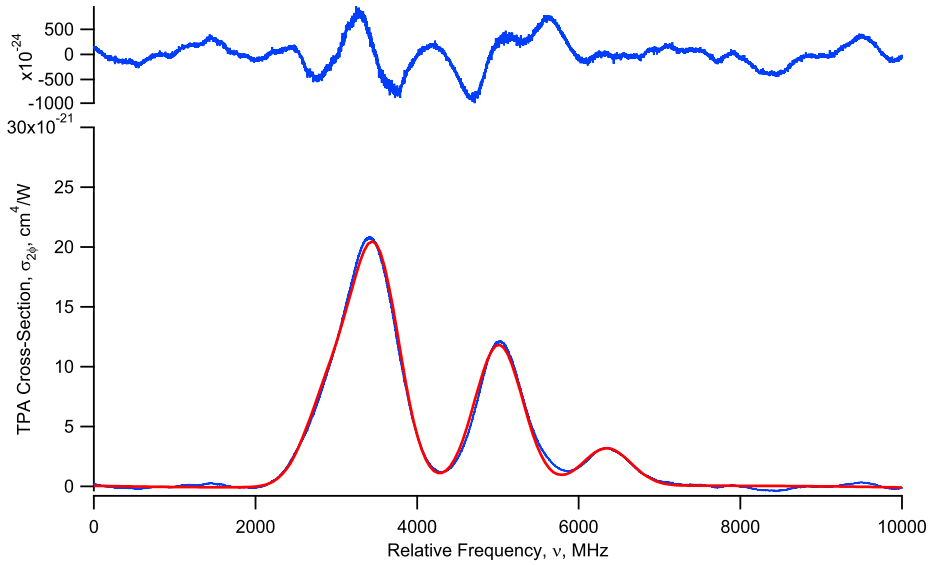

Figure 72. $\sigma_{2\phi} = 1.20 \times 10^{-20} \frac{cm^4}{W}$.

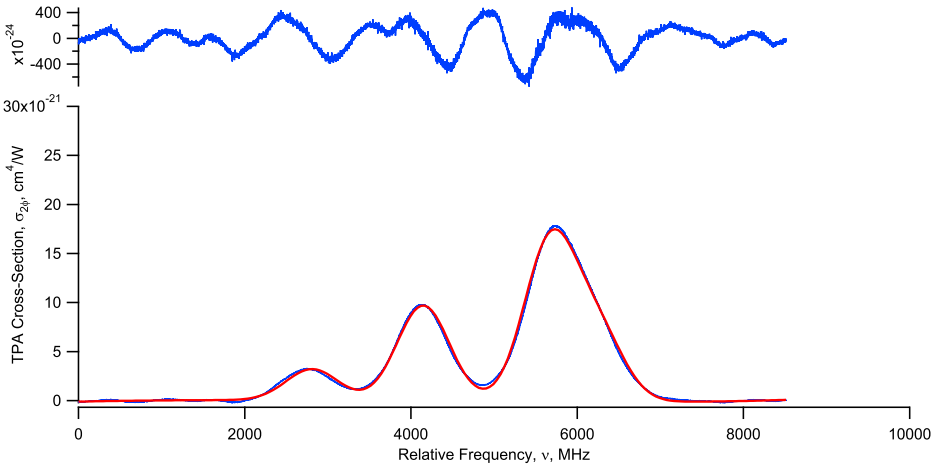

Figure 73. $\sigma_{2\phi} = 9.92 \times 10^{-21} \frac{cm^4}{W}$.

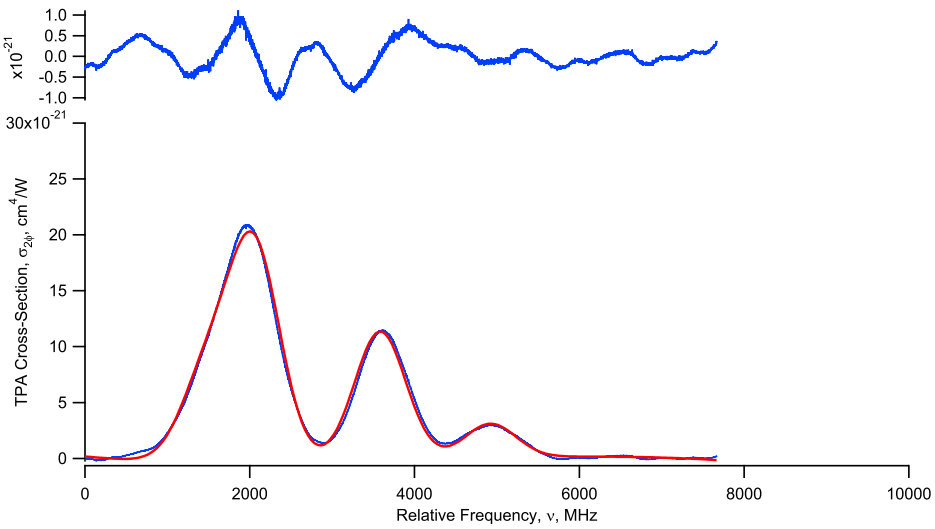

Figure 74. $\sigma_{2\phi} = 1.18 \times 10^{-20} \frac{cm^4}{W}$.

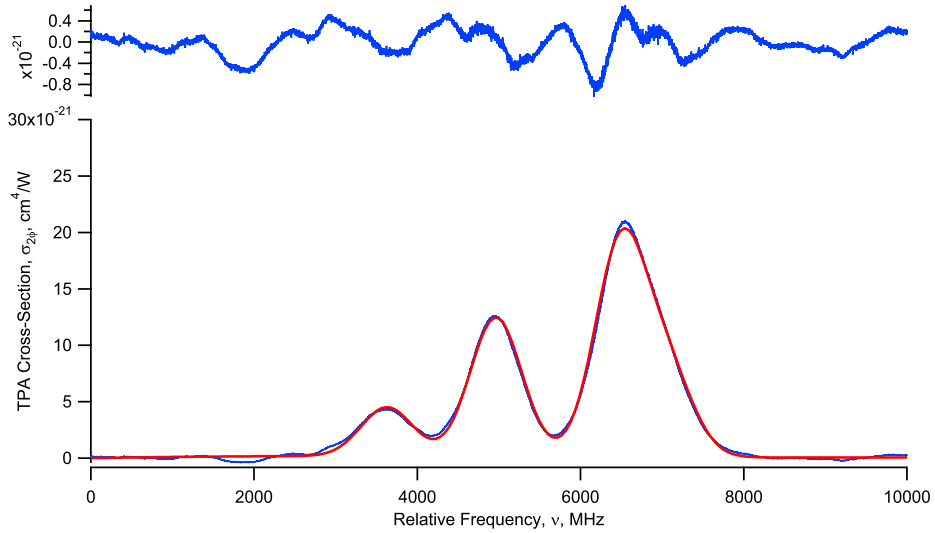

Figure 75. $\sigma_{2\phi} = 1.25 \times 10^{-20} \frac{cm^4}{W}$.

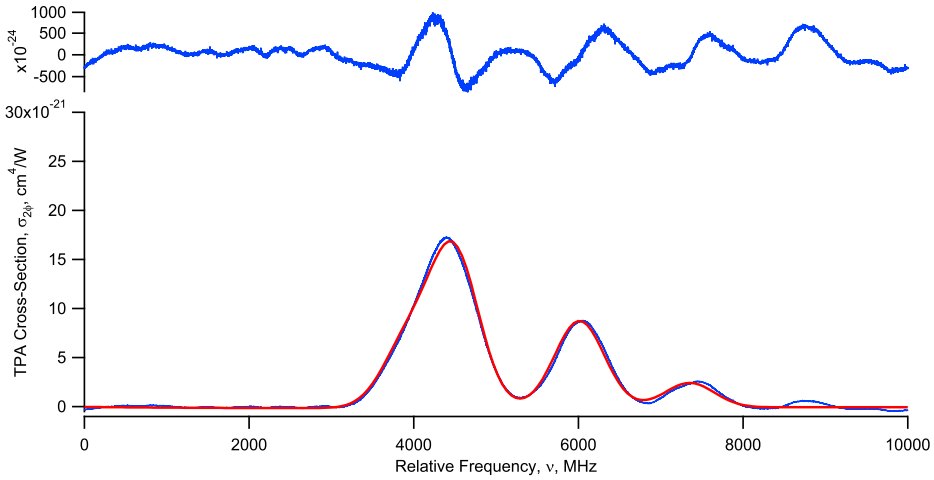

Figure 76. $\sigma_{2\phi} = 8.99 \times 10^{-21} \frac{cm^4}{W}$.

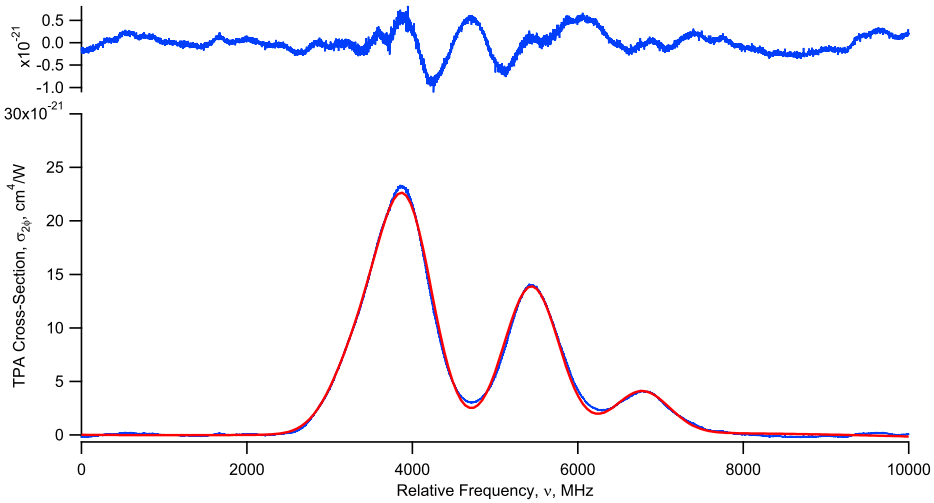

Figure 77. $\sigma_{2\phi} = 1.39 \times 10^{-20} \frac{cm^4}{W}$.

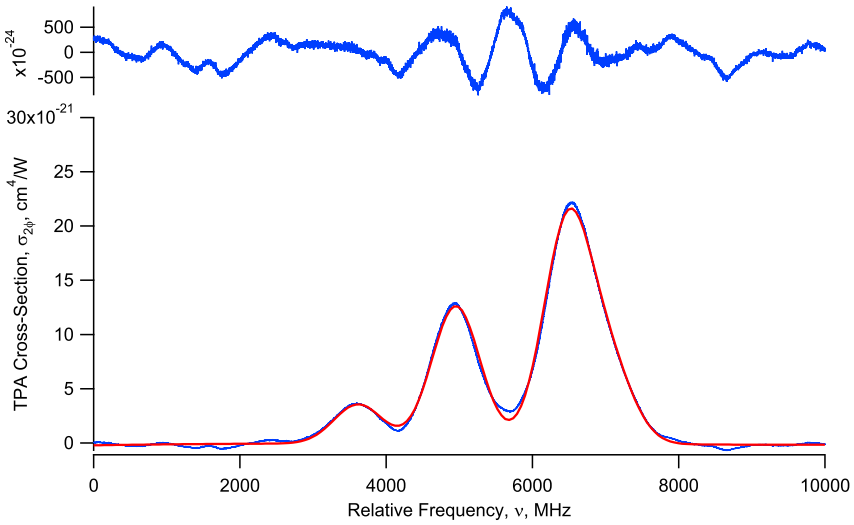

Figure 78. $\sigma_{2\phi} = 1.29 \times 10^{-20} \frac{cm^4}{W}$.

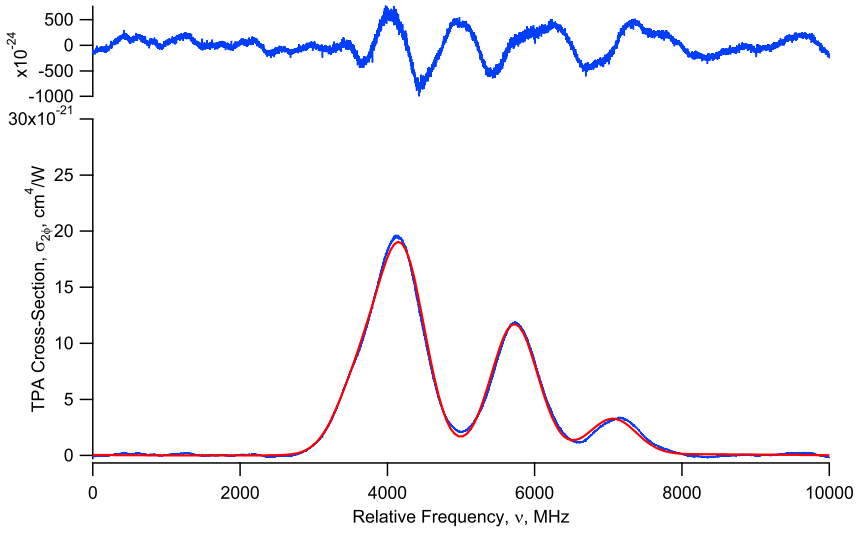

Figure 79. $\sigma_{2\phi} = 1.18 \times 10^{-20} \frac{cm^4}{W}$.

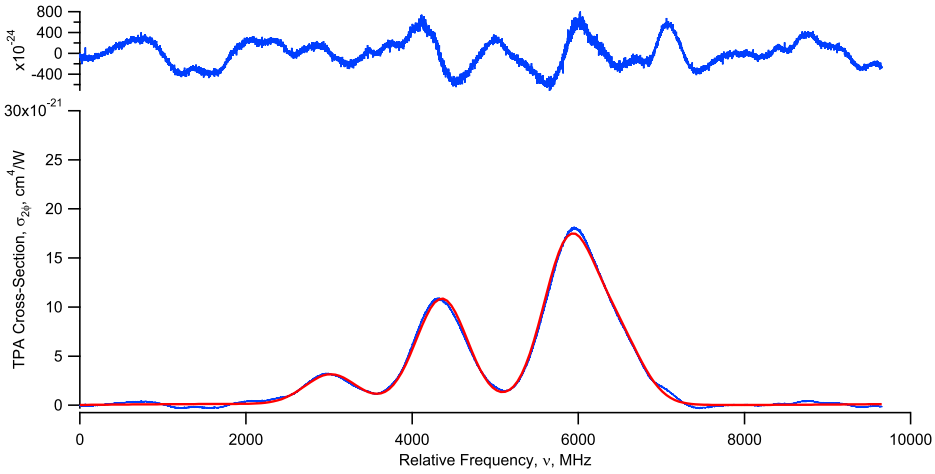

Figure 80. $\sigma_{2\phi} = 1.09 \times 10^{-20} \frac{cm^4}{W}$.

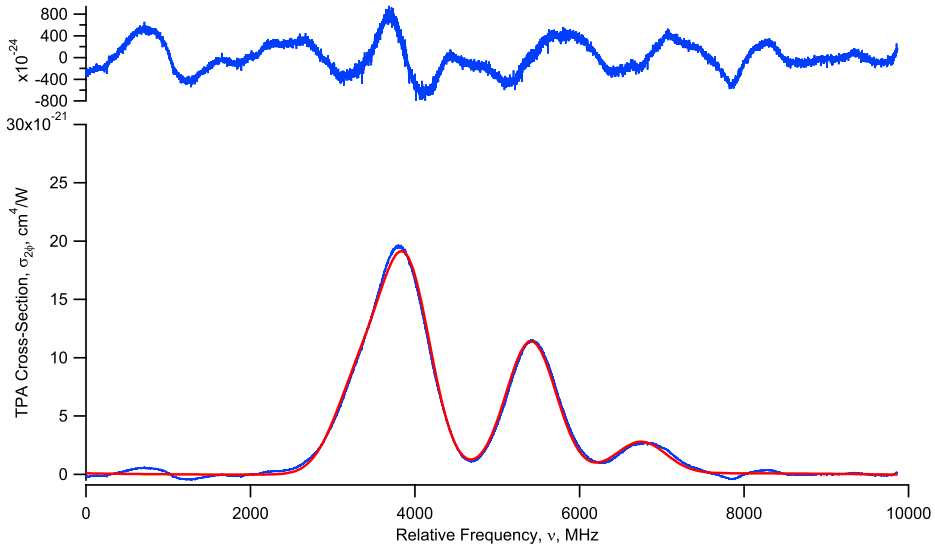

Figure 81. $\sigma_{2\phi} = 1.15 \times 10^{-20} \frac{cm^4}{W}$.

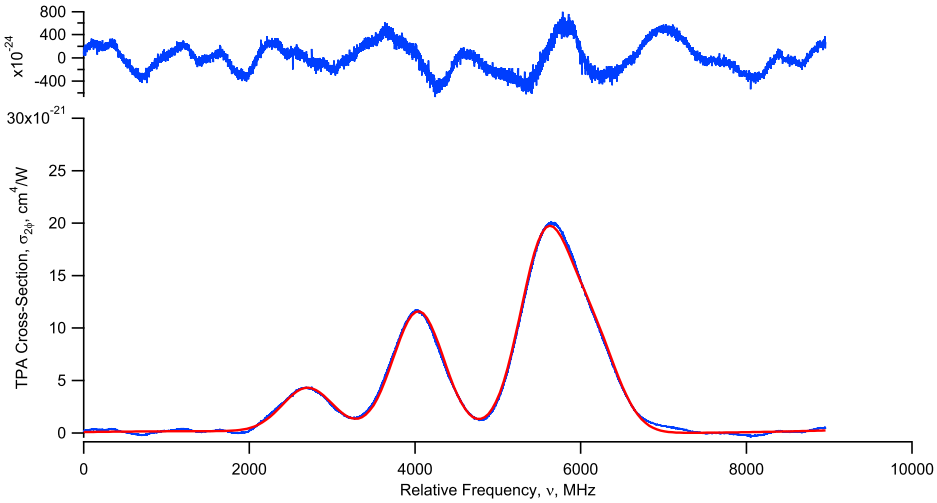

Figure 82. $\sigma_{2\phi} = 1.17 \times 10^{-20} \frac{cm^4}{W}$.

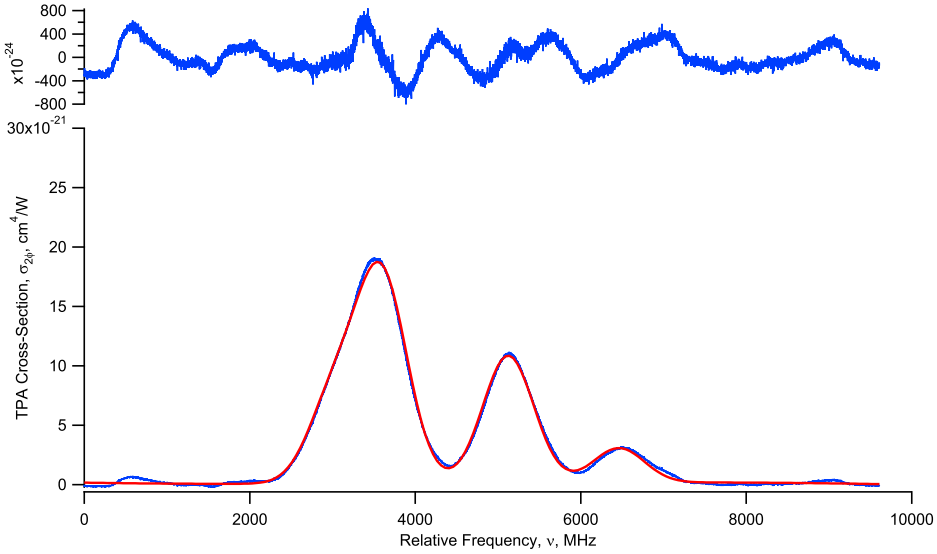

Figure 83. $\sigma_{2\phi} = 1.09 \times 10^{-20} \frac{cm^4}{W}$.

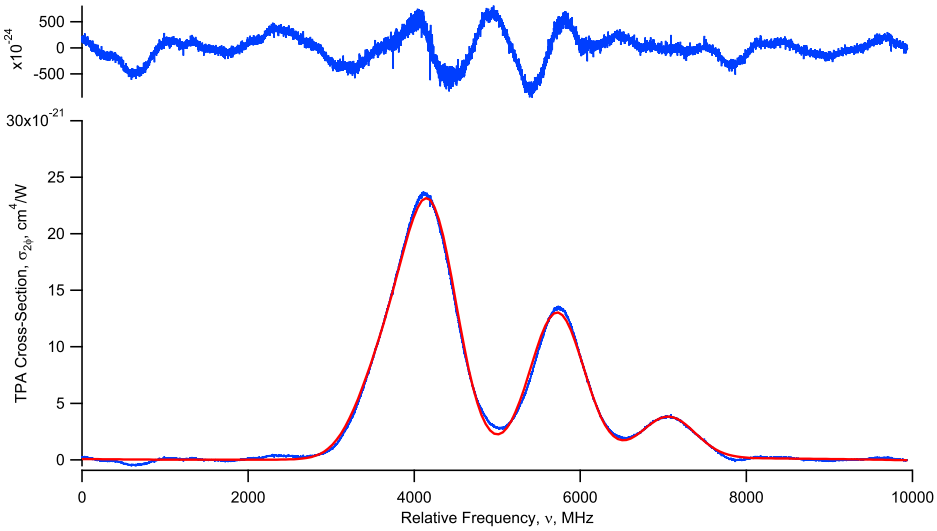

Figure 84. $\sigma_{2\phi} = 1.31 \times 10^{-20} \frac{cm^4}{W}$.

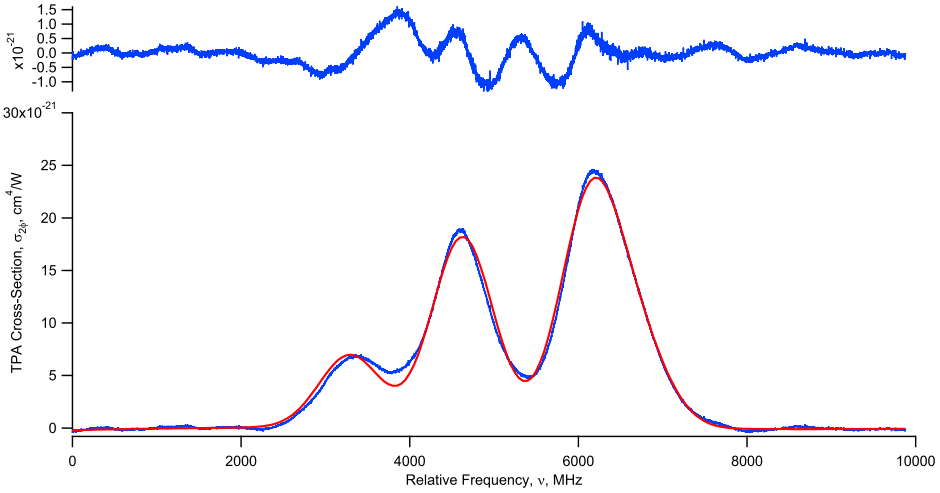

Figure 85. $\sigma_{2\phi} = 1.84 \times 10^{-20} \frac{cm^4}{W}$.

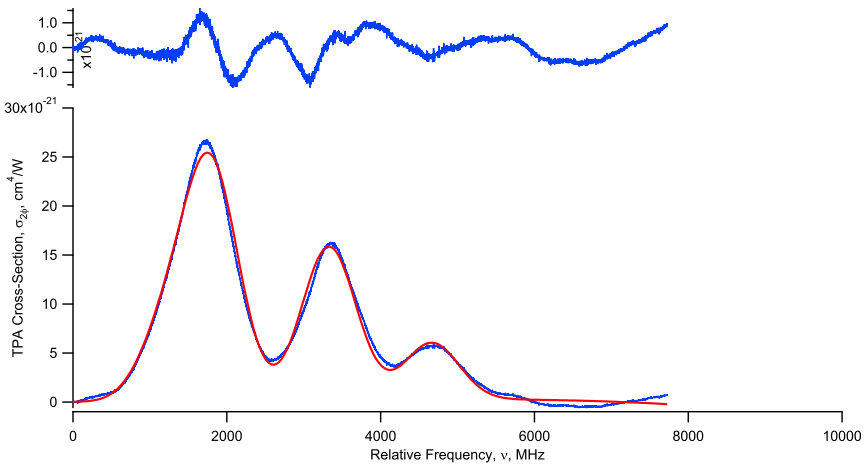

Figure 86. $\sigma_{2\phi} = 1.59 \times 10^{-20} \frac{cm^4}{W}$.

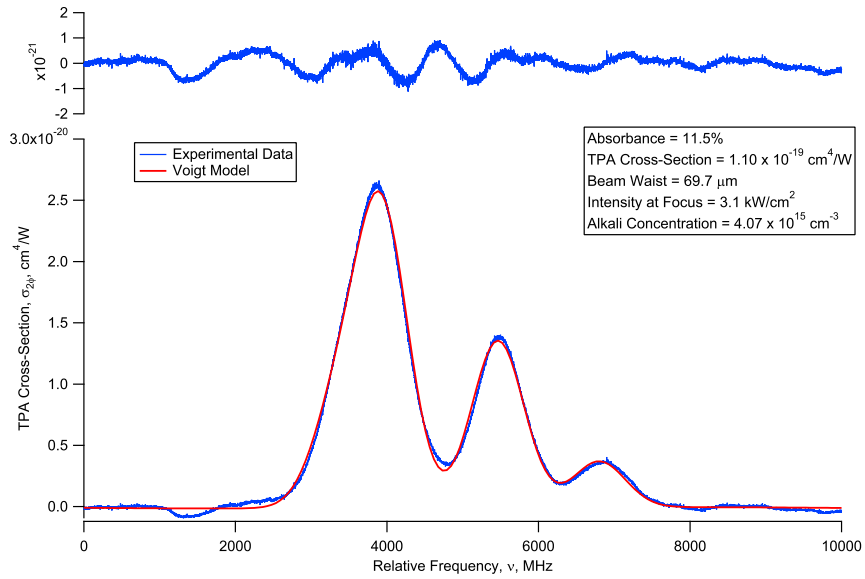

Figure 87. $\sigma_{2\phi} = 1.38 \times 10^{-20} \frac{cm^4}{W}$.

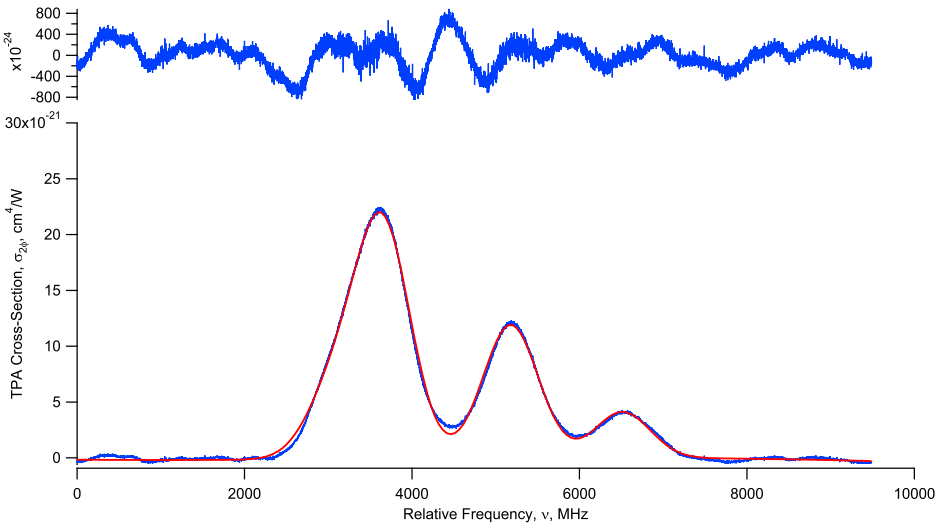

Figure 88. $\sigma_{2\phi} = 1.21 \times 10^{-20} \frac{cm^4}{W}$.

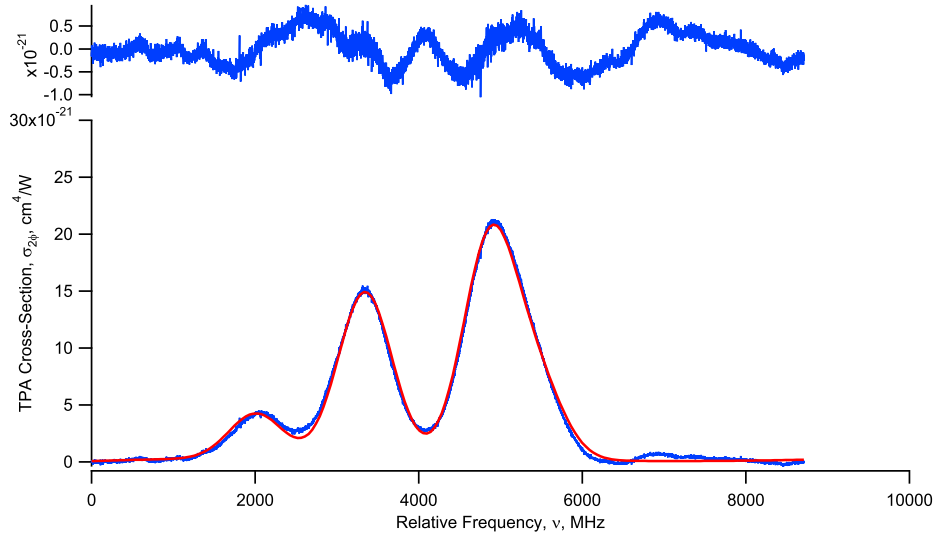

Figure 89. $\sigma_{2\phi} = 1.48 \times 10^{-20} \frac{cm^4}{W}$.

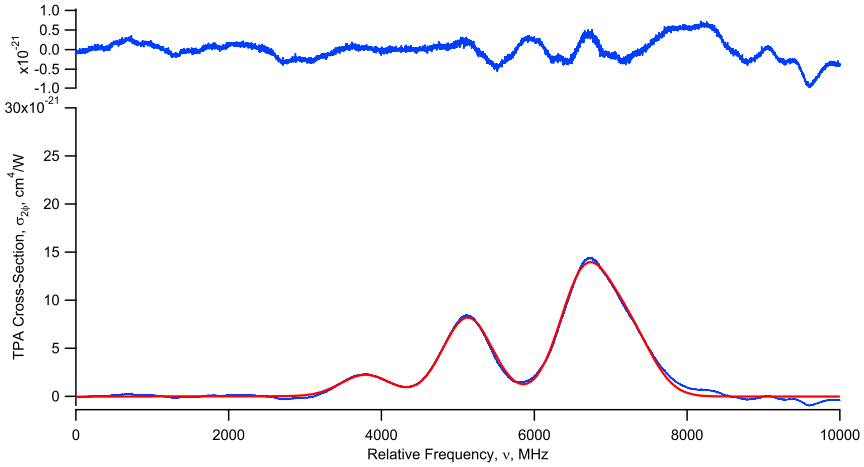

Figure 90. $\sigma_{2\phi} = 8.31 \times 10^{-21} \frac{cm^4}{W}$.

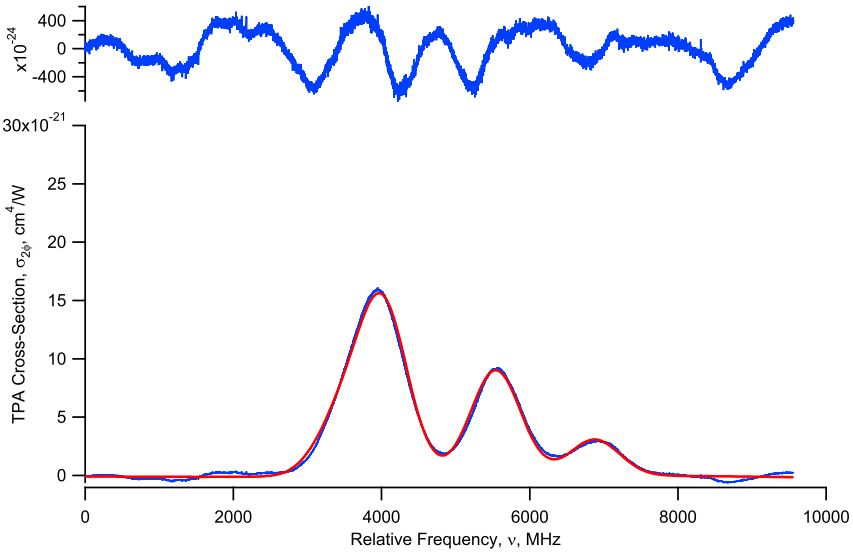

Figure 91. $\sigma_{2\phi} = 9.19 \times 10^{-21} \frac{cm^4}{W}$.

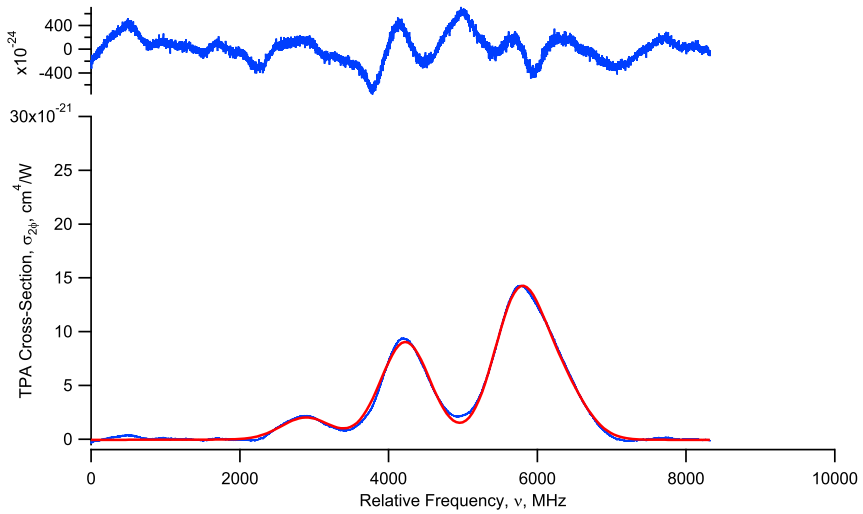

Figure 92. $\sigma_{2\phi} = 9.19 \times 10^{-21} \frac{cm^4}{W}$.

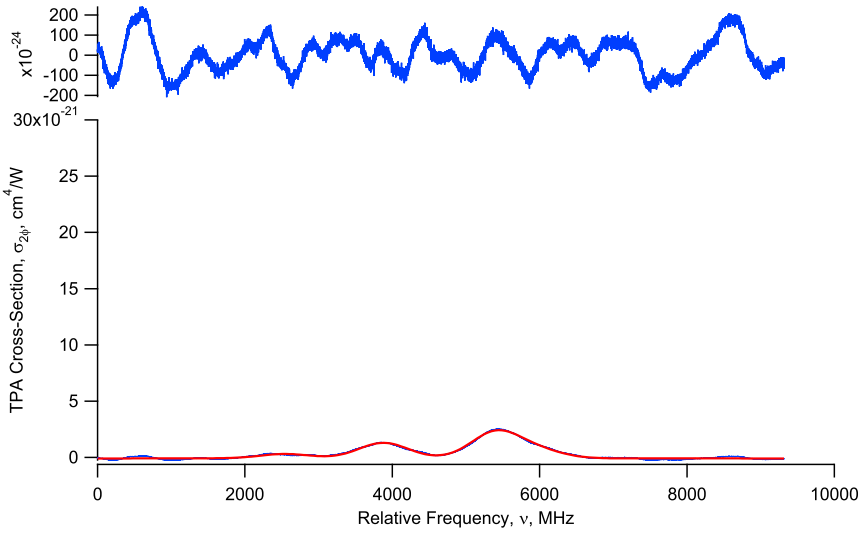

Figure 93. $\sigma_{2\phi} = 1.39 \times 10^{-21} \frac{cm^4}{W}$.

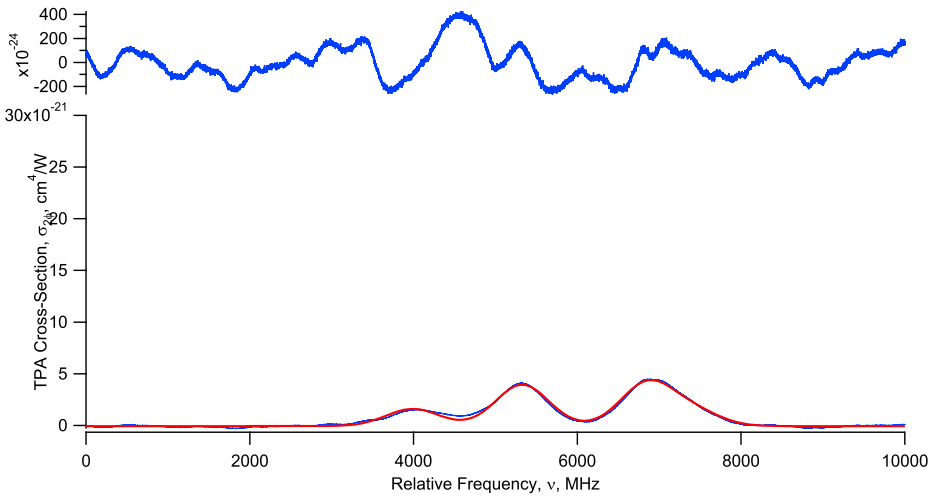

Figure 94. $\sigma_{2\phi} = 4.06 \times 10^{-21} \frac{cm^4}{W}$.

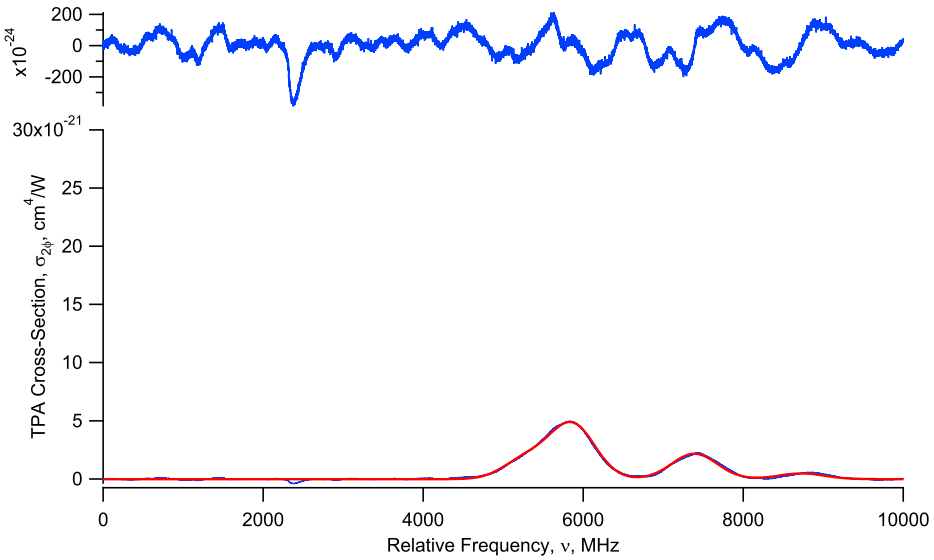

Figure 95. $\sigma_{2\phi} = 2.23 \times 10^{-21} \frac{cm^4}{W}$.

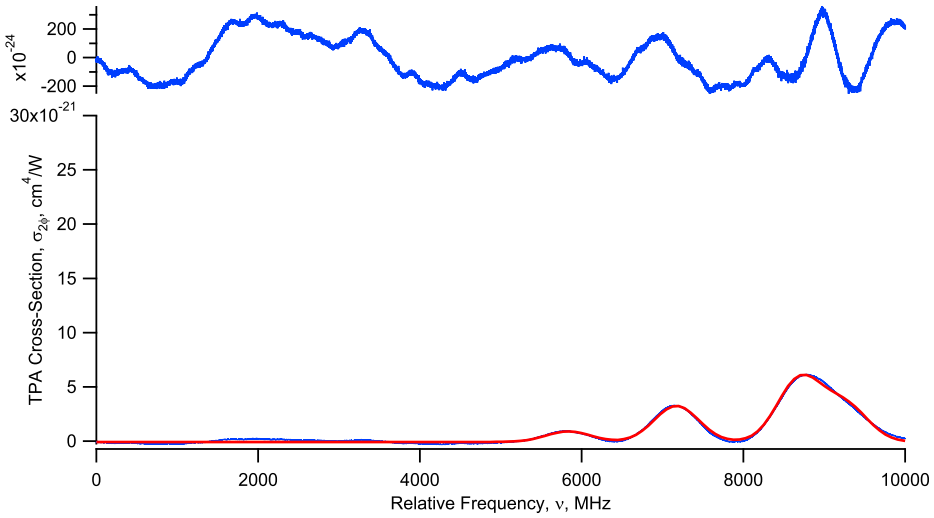

Figure 96. $\sigma_{2\phi} = 3.38 \times 10^{-21} \frac{cm^4}{W}$.

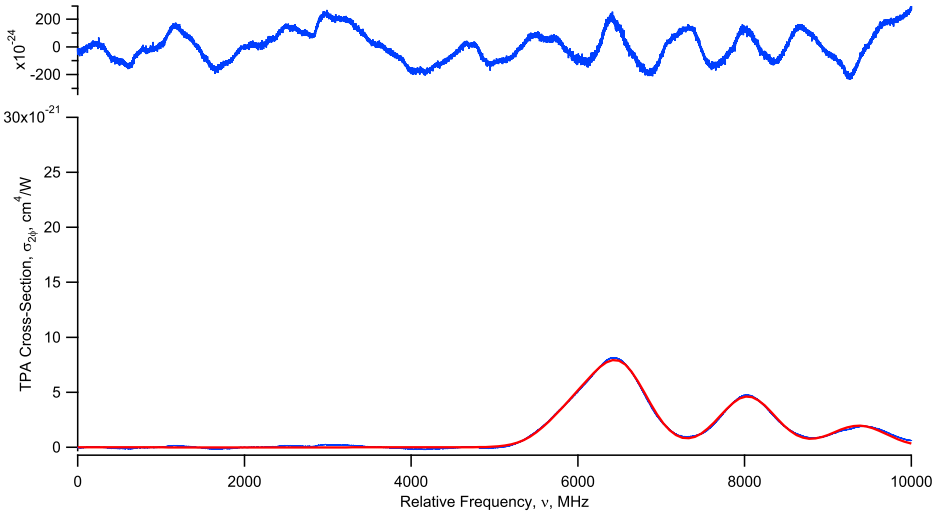

Figure 97. $\sigma_{2\phi} = 4.68 \times 10^{-21} \frac{cm^4}{W}$.

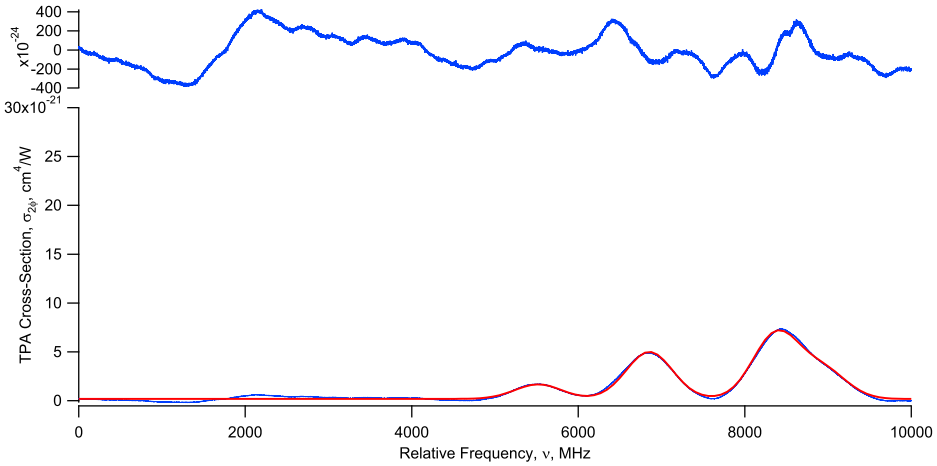

Figure 98. $\sigma_{2\phi} = 4.83 \times 10^{-21} \frac{cm^4}{W}$.

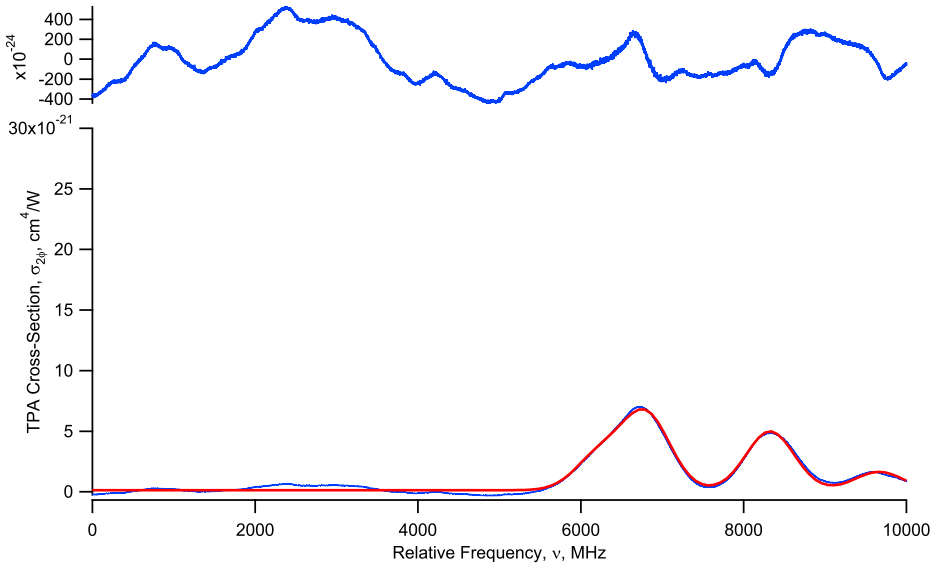

Figure 99. $\sigma_{2\phi} = 4.93 \times 10^{-21} \frac{cm^4}{W}$.

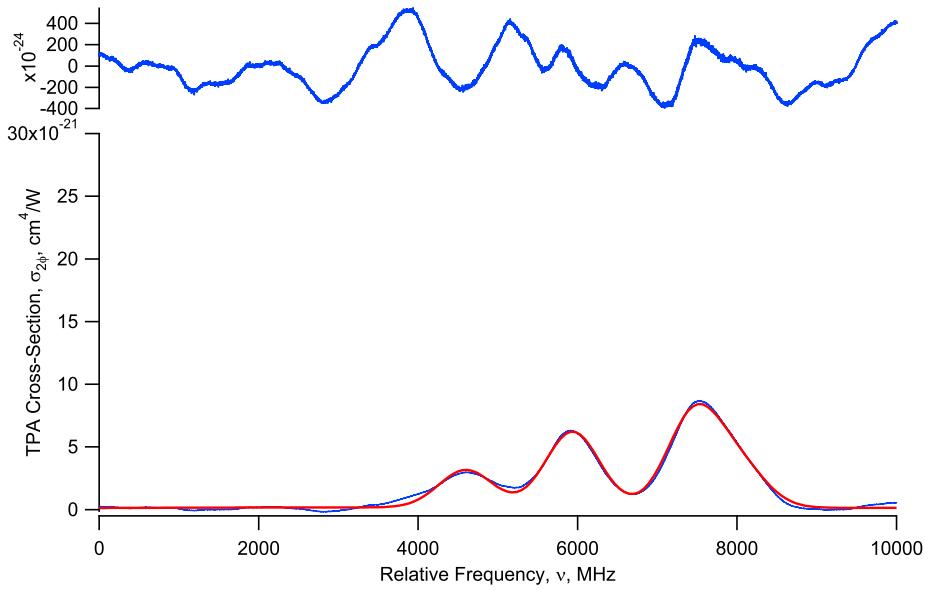

Figure 100. $\sigma_{2\phi} = 6.14 \times 10^{-21} \frac{cm^4}{W}$.

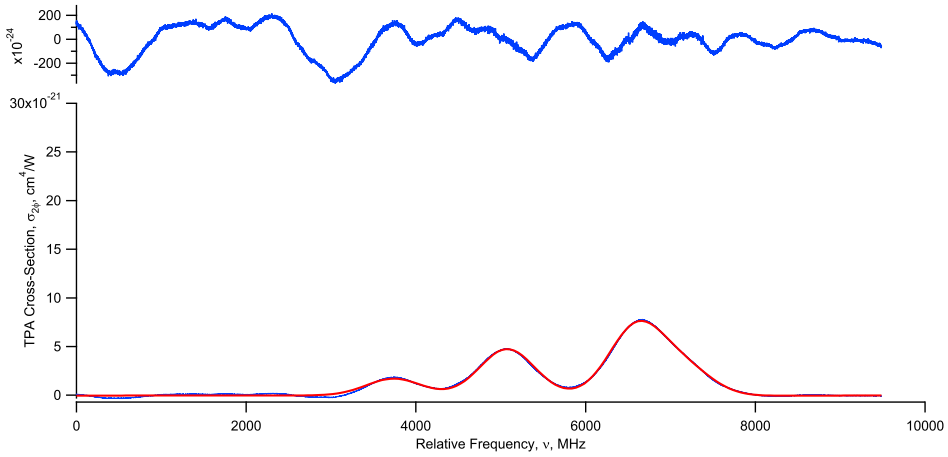

Figure 101. $\sigma_{2\phi} = 4.87 \times 10^{-21} \frac{cm^4}{W}$.

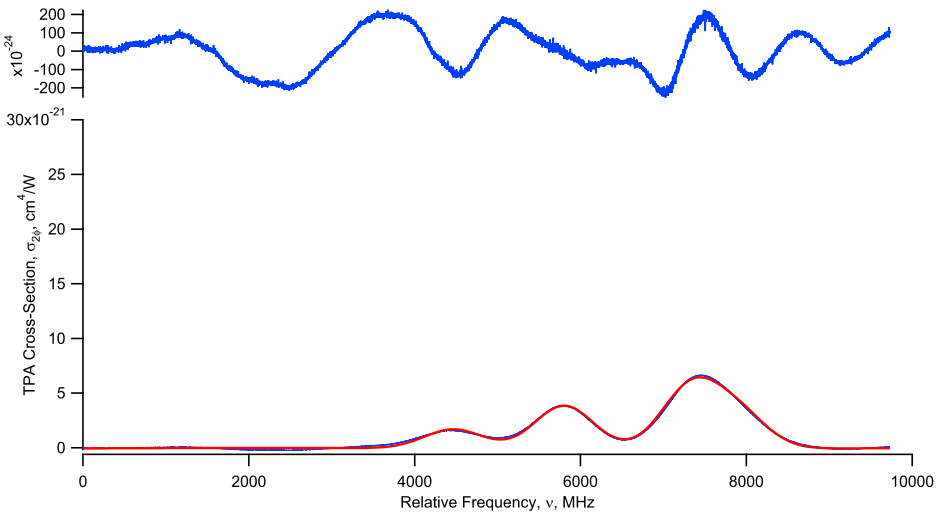

Figure 102. $\sigma_{2\phi} = 3.99 \times 10^{-21} \frac{cm^4}{W}$.

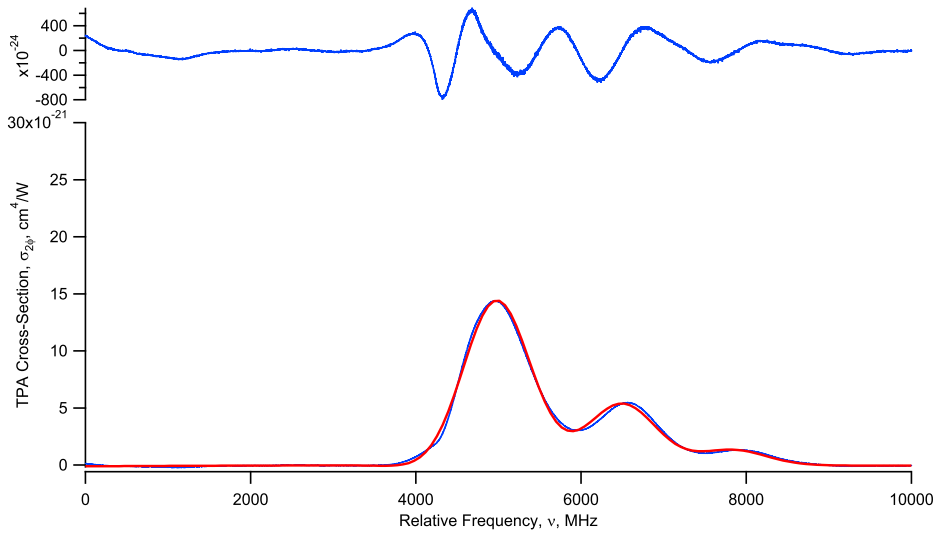

Figure 103. $\sigma_{2\phi} = 5.45 \times 10^{-21} \frac{cm^4}{W}$.

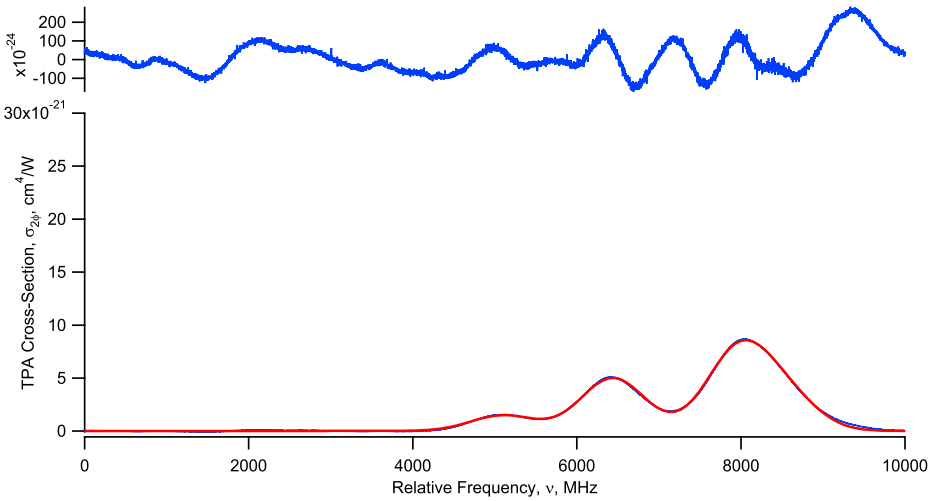

Figure 104. $\sigma_{2\phi} = 5.05 \times 10^{-21} \frac{cm^4}{W}$.

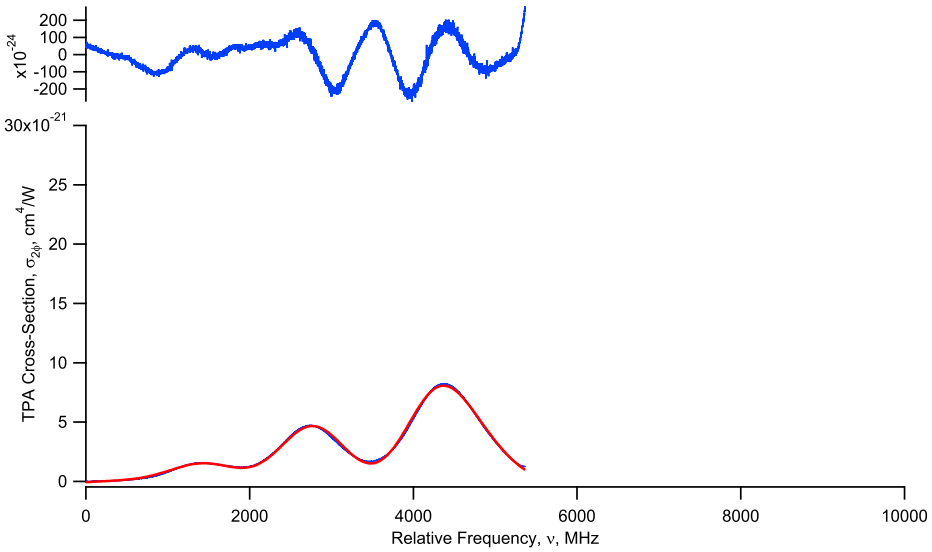

Figure 105. $\sigma_{2\phi} = 4.86 \times 10^{-21} \frac{cm^4}{W}$.

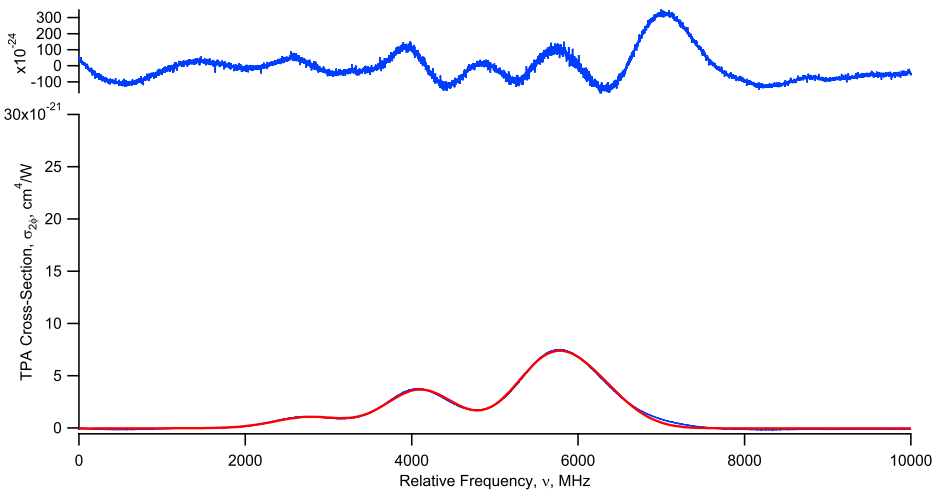

Figure 106. $\sigma_{2\phi} = 3.72 \times 10^{-21} \frac{cm^4}{W}$.

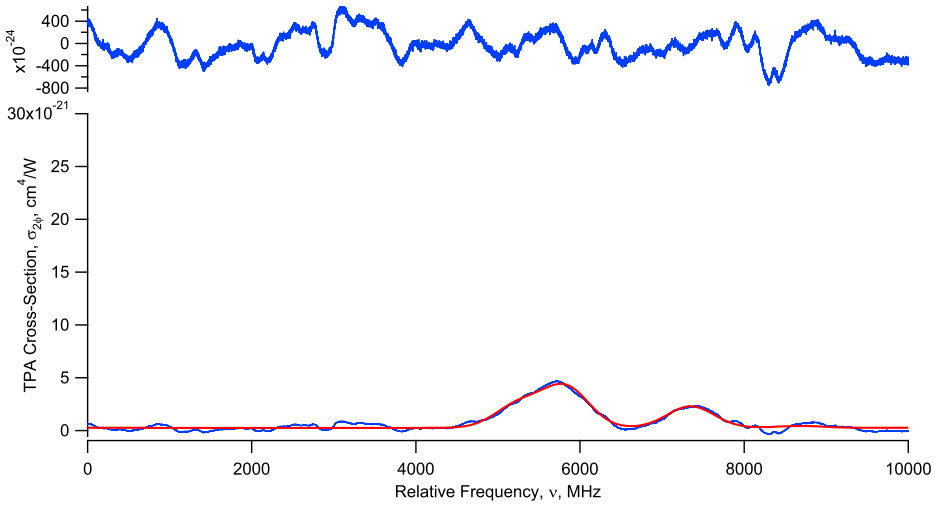

Figure 107. $\sigma_{2\phi} = 2.09 \times 10^{-21} \frac{cm^4}{W}$.

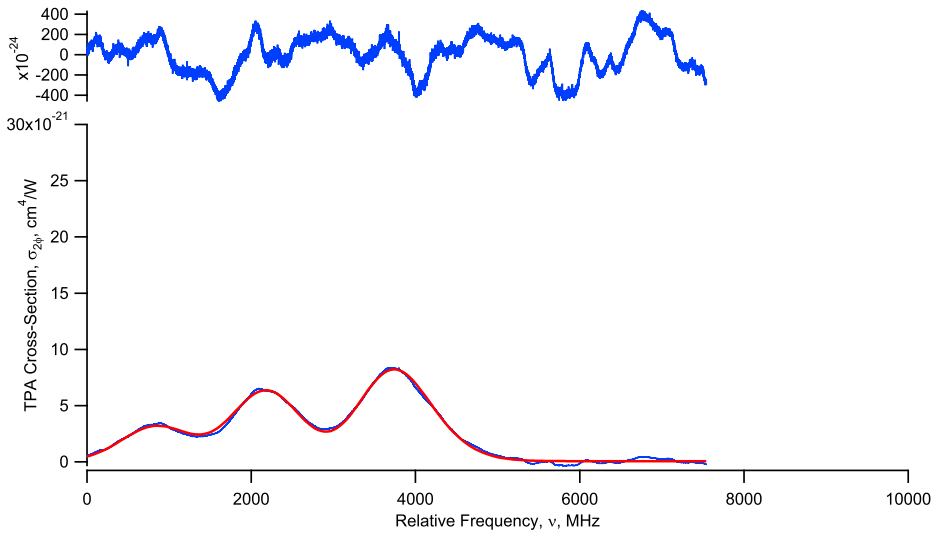

Figure 108. $\sigma_{2\phi} = 6.21 \times 10^{-21} \frac{cm^4}{W}$.

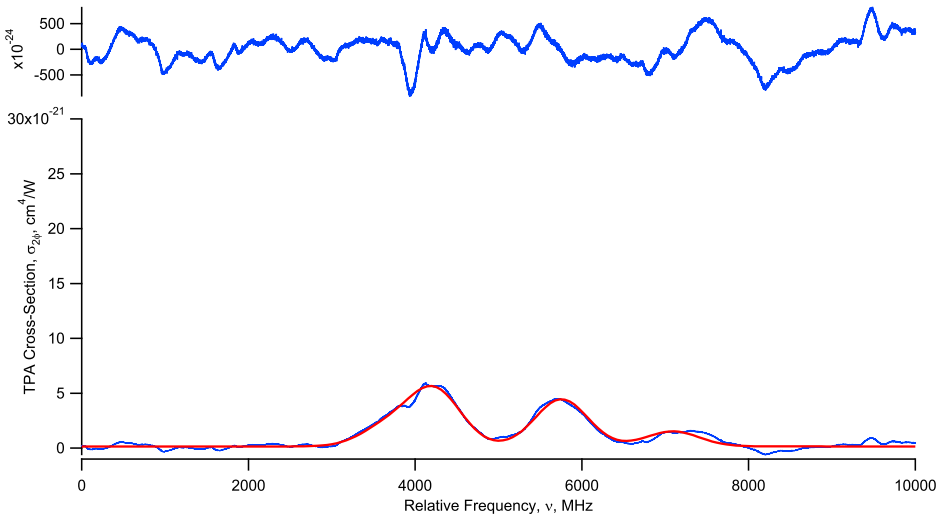

Figure 109. $\sigma_{2\phi} = 4.35 \times 10^{-21} \frac{cm^4}{W}$.

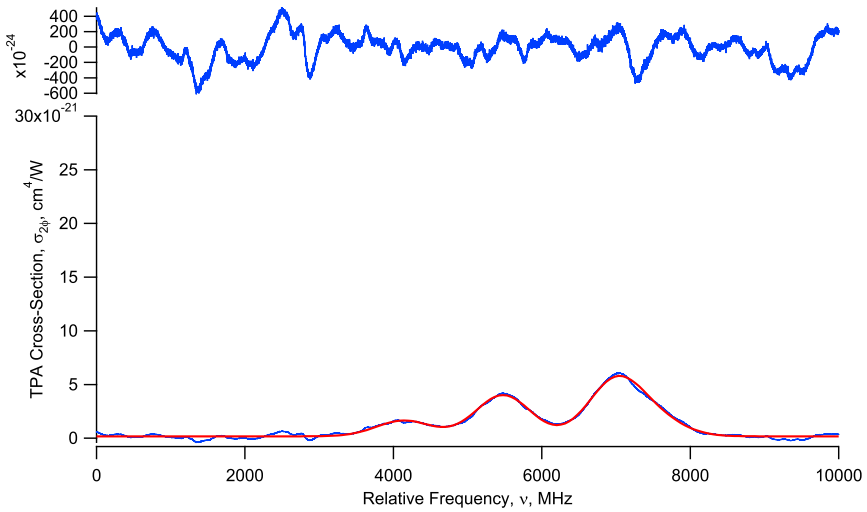

Figure 110. $\sigma_{2\phi} = 3.88 \times 10^{-21} \frac{cm^4}{W}$.

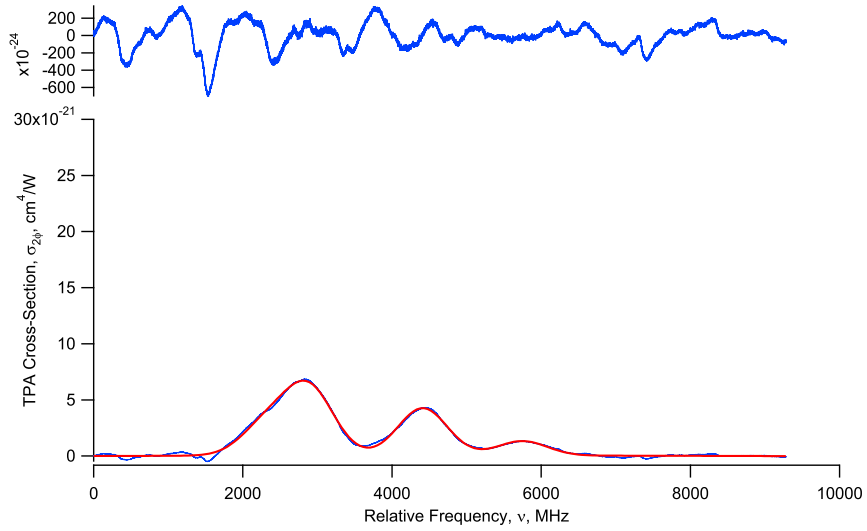

Figure 111. $\sigma_{2\phi} = 4.28 \times 10^{-21} \frac{cm^4}{W}$.

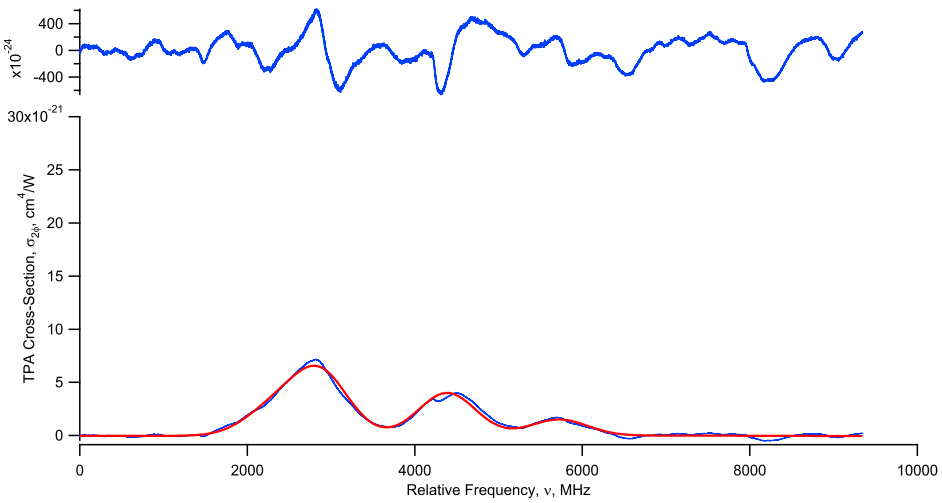

Figure 112. $\sigma_{2\phi} = 4.08 \times 10^{-21} \frac{cm^4}{W}$.

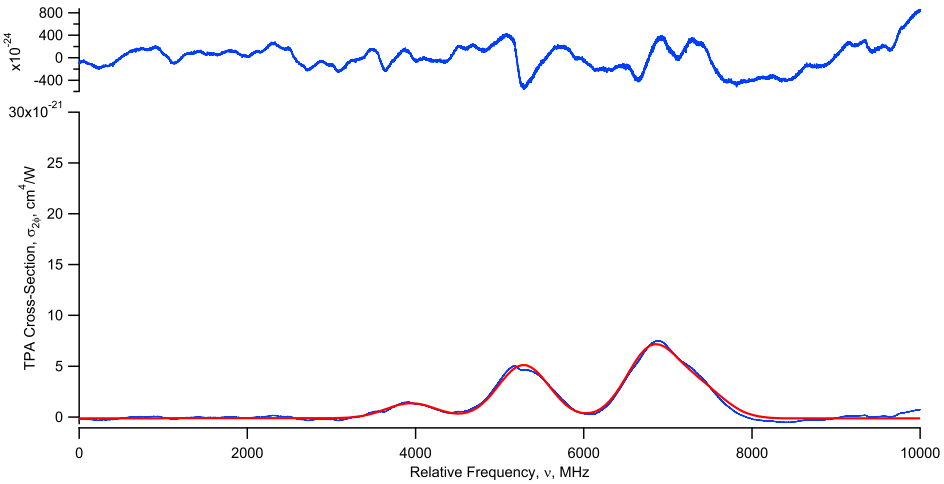

Figure 113. $\sigma_{2\phi} = 5.33 \times 10^{-21} \frac{cm^4}{W}$.

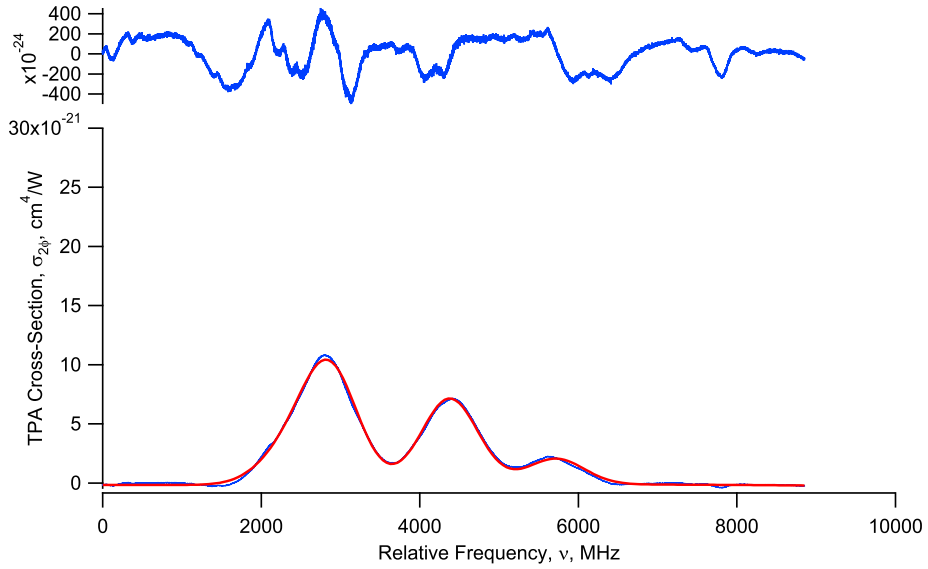

Figure 114. $\sigma_{2\phi} = 7.35 \times 10^{-21} \frac{cm^4}{W}$.

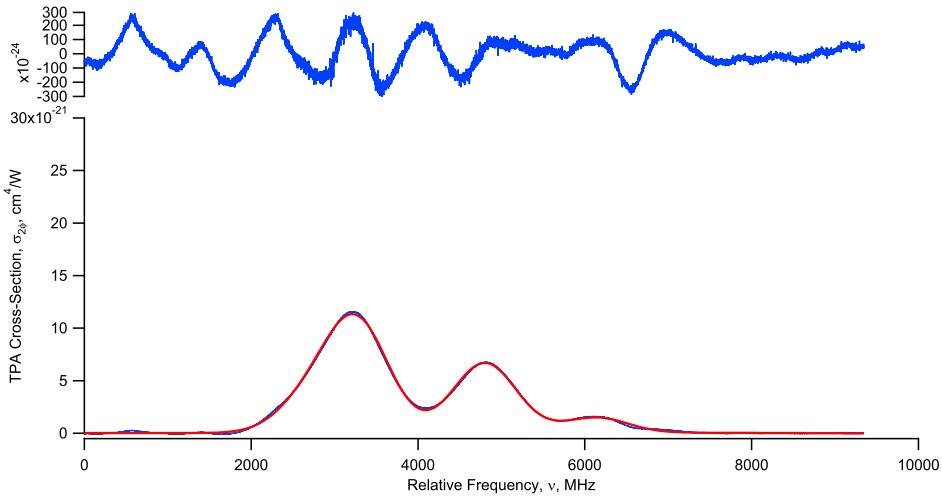

Figure 115. $\sigma_{2\phi} = 6.72 \times 10^{-21} \frac{cm^4}{W}$.

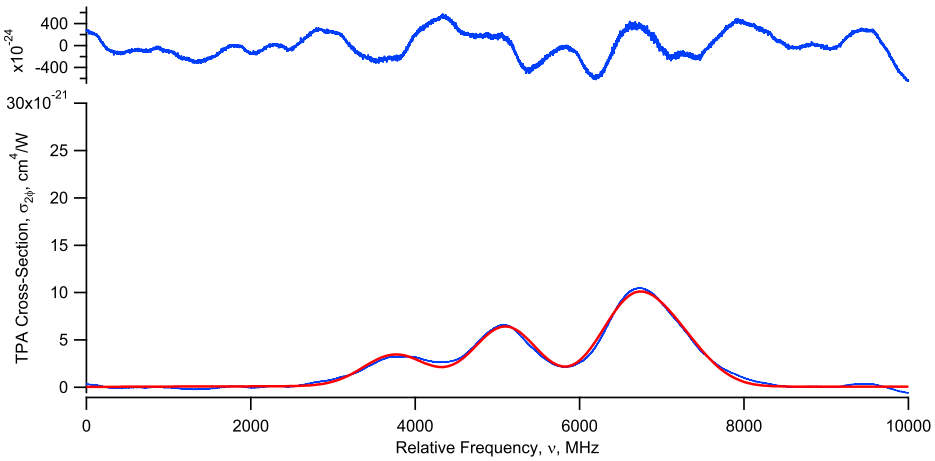

Figure 116. $\sigma_{2\phi} = 6.39 \times 10^{-21} \frac{cm^4}{W}$.

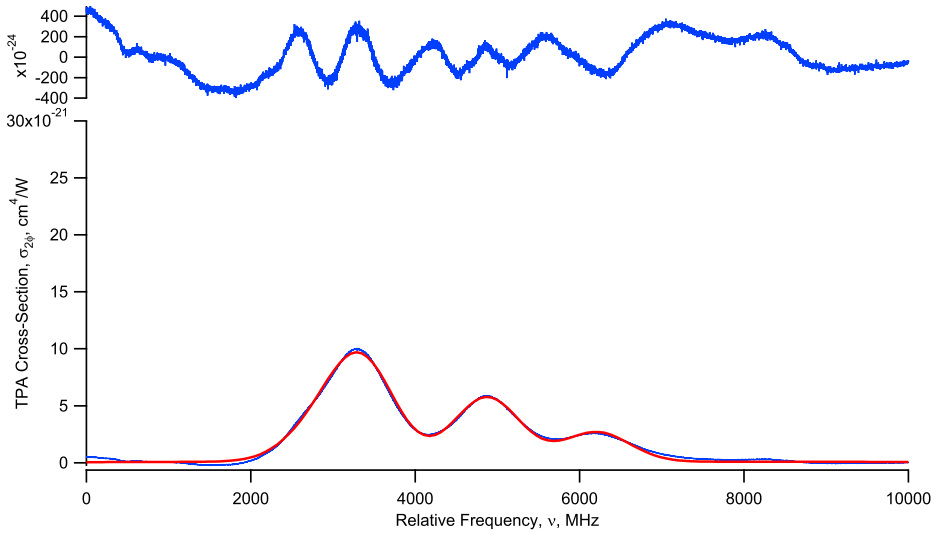

Figure 117. $\sigma_{2\phi} = 5.73 \times 10^{-21} \frac{cm^4}{W}$.

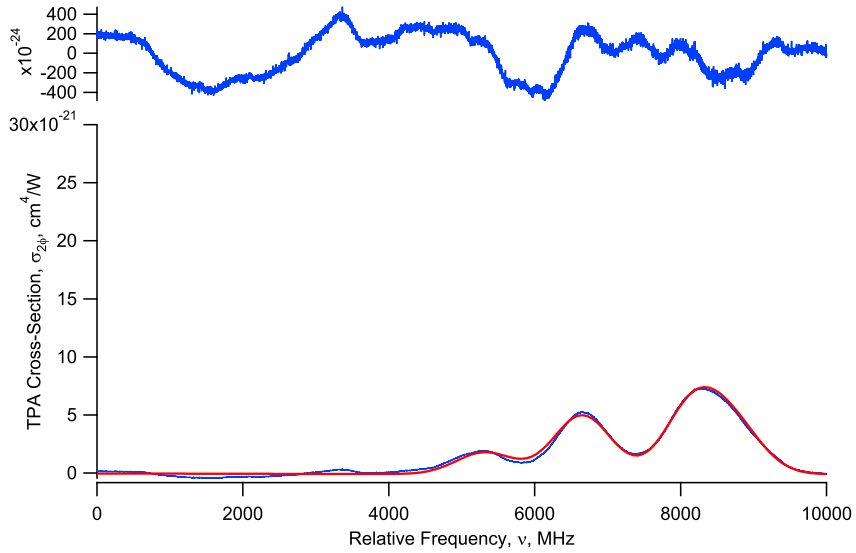

Figure 118. $\sigma_{2\phi} = 5.16 \times 10^{-21} \frac{cm^4}{W}$.

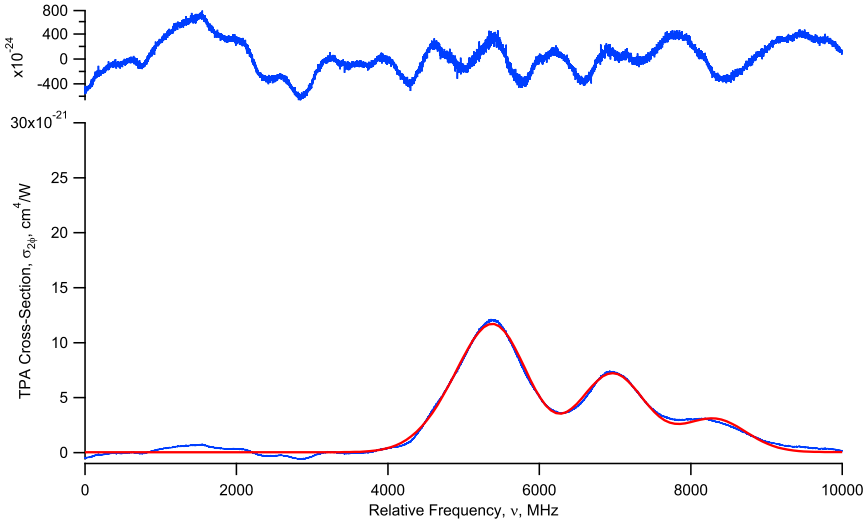

Figure 119. $\sigma_{2\phi} = 7.22 \times 10^{-21} \frac{cm^4}{W}$.

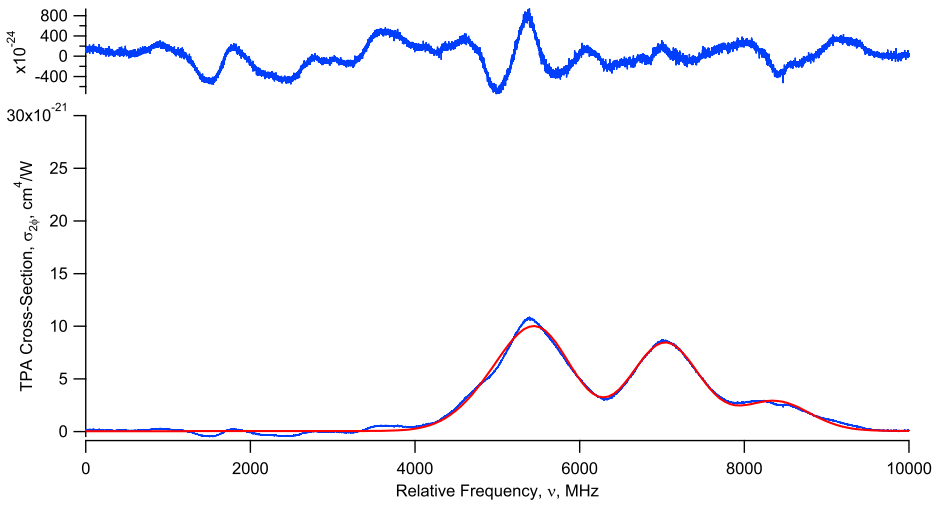

Figure 120. $\sigma_{2\phi} = 8.47 \times 10^{-21} \frac{cm^4}{W}$.

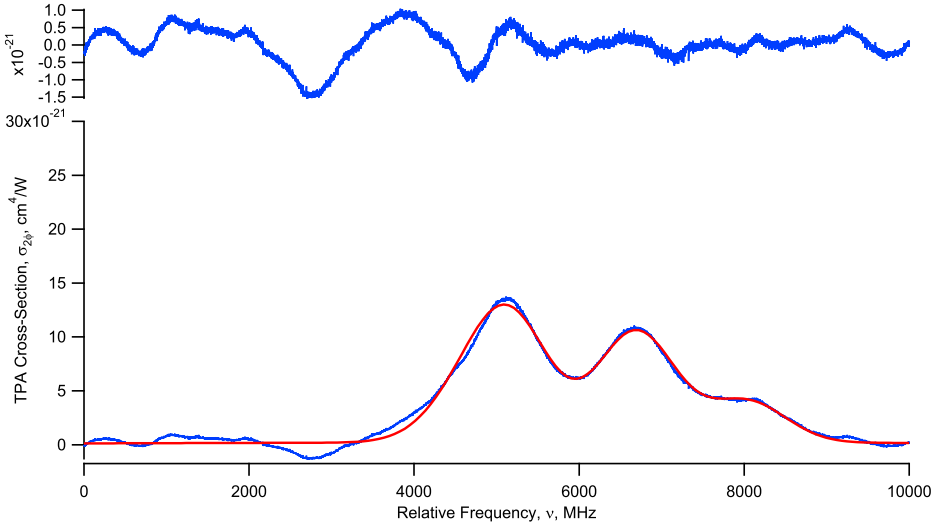

Figure 121. $\sigma_{2\phi} = 1.04 \times 10^{-20} \frac{cm^4}{W}$.

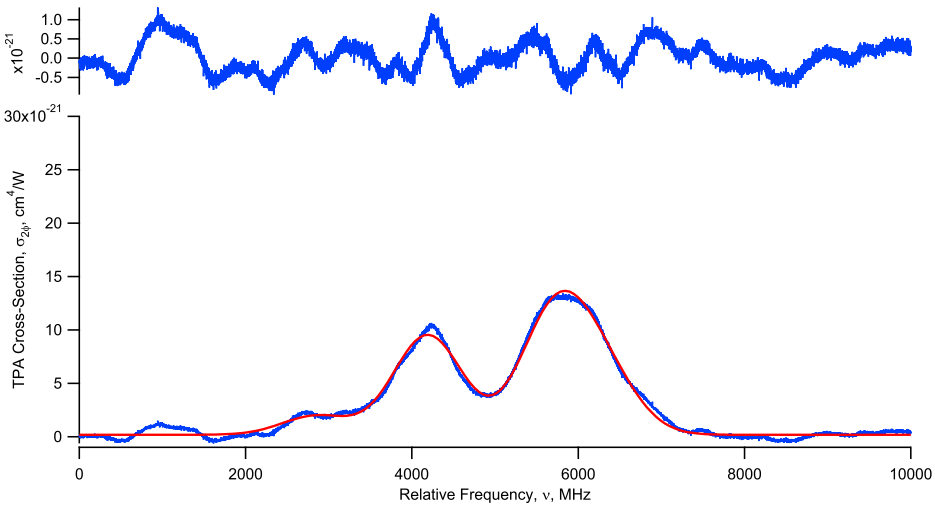

Figure 122. $\sigma_{2\phi} = 9.44 \times 10^{-21} \frac{cm^4}{W}$.

Appendix D. Voigt Model in IGOR Pro

The Equations below are the main pieces to the IGOR Pro code used for the Voigt model. There are 17 Voigts corresponding to the 17 allowed hyperfine transitions.

$$cw[2] = \frac{\Delta\nu_h}{\nu_0}\sqrt{\frac{mc^2}{8kT}} \quad (Lorentzian\ width) \tag{102}$$

$$cw[3] = \frac{1}{\nu_0}\sqrt{\frac{mc^2}{2kT}} \quad (1/Doppler\ width) \tag{103}$$

$$fVoigt = \frac{y}{\pi}\int_{-\infty}^{\infty}\frac{e^{-t^2}dt}{y+(x-t)^2} \tag{104}$$

In addition to the equations above, the Voigt model contains the isotope fraction, the Boltzmann factor and the two-photon relative signal strength. Finally, the Voigt model also includes four factors for the 3rd order polynomial baseline.

Bibliography

1. A. Akulshin, A. Sidorov, R. McLean and P. Hannaford. "Coherent and collimated blue light generated by four-wave mixing in Rb vapour". *Optics Express*, 17(25):22861–22870, 2009.

2. A. Danielli, A. Arie M. Chou, P. Rusian and M. Fejer. "Frequency stabilization of a frequency-doubled 1556-nm source to the $5S_{1/2} \longrightarrow 5D_{5/2}$ two-photon transitions of rubidium". *Optics Letters*, 25(12):905–907, 2000.

3. A. Olsen, E. Carlson and S. Mayer. "Two-photon spectroscopy of rubidium using a grating-feedback diode laser". *Am. J. Phys.*, 74(3):218–223, 2006.

4. A. Palla, J. Verdeyen, D. Carroll and M. Heaven. *J Phys B:At. Mol. Opt.*, 44:135402, 2011.

5. A. Sharma, Y. Lu, N. Bhaskar and W. Happer. "Continuous-wave mirrorless lasing in optically pumped atomic Cs and Rb vapors". *Applied Physics letters*, 39(3):209–211, 1981.

6. A. Zibrov, D. Nikonov L. Holberg M. Scully-V. Velichansky, M. Lukin and H. Robinson. "Experimental Demonstration of Laser oscillation without Population Inversion via Quantum Interference in Rb". *Physical Review Letters*, 75(8):1499–1502, 1995.

7. A. Zibrov, D. Nikonov L. Holberg M. Scully-V. Velichansky, M. Lukin and H. Robinson. "Efficient frequency up-conversion in resonant coherent media". *Physical Review A*, 65(021801), 2002.

8. Abella, I. "Optical Double-Quantum Absorption in Cesium Vapor". *Physical Review Letters*, 9:453, 1962.

9. Adams, C. "Saturated spectroscopy and two-photon absorption spectroscopy in rubidium using an actively stabilised Ti:Al_2O_3 ring laser". *Optics Communications*, 75(5,6):419–424, 1990.

10. B. Cagnac, L. Julien F. Nez, F. Biraben and S. Boutzeix. "Two-photon Spectroscopy of Optical Frequencies in Rubidium and Hydrogen". *Laser Physics*, 6(2):213–219, 1996.

11. B. Zhdanov, G. Boyadjian A. Voci, A. Stooke and R. Knize. "Laser diode array pumped continuous wave Rubidium vapor laser". *Optics Express*, 16(2):748–751, 2008.

12. B. Zhdanov, T. Ehrenreich and R. Knize. "Highly efficient optically pumped cesium vapor laser". *Optics Communications*, 260:696–698, 2006.

13. Bauch, A. *Meas. Sci. Technol.*, 14:1159–1173, 2003.

14. Bebb, B. "Multiphoton Ionization of Hydrogen and Rare-Gas Atoms". *The Physical Review*, 143(1):1–24, 1966.

15. Bebb, B. "Quantitative Theory of the Two-Photon Ionization of the Alkali Atoms". *The Physical Review*, 149(1):25–32, 1966.

16. C. Sulham, G. Pitz and G. Perram. 2009. Submitted to Applied Physics B.

17. C. Sulham, M. Wilkson, G. Perram and D. Hostutler. *Optics Communications*, 283:4328, 2010.

18. Carrington, C. and A. Gallagher. *Phys Rev A*, 10:1464, 1974.

19. Collins, C. "Absolute two-photon cross section of Rb measured by differential absorption". *Optics Letters*, 18(20):1754, 1993.

20. D. Bamford, L. Jusinski and W. Bischel. "Absolute two-photon absorption and three-photon ionization cross-sections for atomic oxygen". *Physical Review A*, 34(1):185–198, 1986.

21. D. Touahri, A. Clairon J. Zondy R. Felder-L. Hilico B. de Beauvoir F. Biraben, O. Acef and F. Nez. "Frequency measurement of the $5S_{1/2}(F = 3) - 5D_{5/2}(F = 5)$ two-photon transition in rubidium". *Optics Communications*, 133:471–478, 1997.

22. Demtröder, W. *Laser Spectroscopy*. Springer, 3^{rd} edition, 2003. ISBN 3-540-65225-6.

23. E. Courtade, D. Ciampini J. Müller O. Morsch-E. Arimondo M. Aymer, M. Anderlini and E. Robinson. "Two-photon ionization of cold rubidium atoms with a near resonant intermediate state". *Journal of Physics B*, 37:967–979, 2004.

24. F. Nez, R. Felder, F. Biraben and Y. Millerioux. "Optical frequency determination of the hyperfine components of the $5S_{1/2} - 5D_{3/2}$ two-photon transitions in rubidium". *Optics Communications*, 102:432–438, 1993.

25. Göppert-Mayer, M. "Über Elementarakte mit zwei Quantensprüngen". *Annalen der Physik*, 401(3):273–294, 1931.

26. Gordon, G. "The Ann Arbor Conference on Optical Pumping". P.A. Franken and R.H. Sands (editors), *The LASER, Light Amplification by Stimulated Emission of Radiation*, 128. University of Michigan, June 1959.

27. H. You, S. Hendrickson and J. Franson. "Enhanced two-photon absorption using entagled states and small mode volumes". *Journal of Physics A*, 80, 2009.

28. Hager, G. and G. Perram. *Applied Physics B*, 101:45, 2010.

29. Herzberg, G. *The Spectra of Diatomic Molecules*. New York, 2^{nd} edition, 1957.

30. Hostutler, D. *to be published.*

31. Hurd, Edward. M.S. thesis, Graduate School of Engineering, Air Force Institute of Technology (AETC), Wright-Patterson AFB OH, March 2012.

32. J. Garreau, L. Julien, M. Allegrini and F. Biraben. "High resolution spectroscopy of the hydrogen atom. I. Method and experiment". *Journal de Physique France*, 51(5,6):2263–2273, 1990.

33. J. Hewitt, J. Gallagher D. Carroll G. Perram, T. Houlahan and J. Eden. "Role of Excited State Photoionization in the 852.1 nm Cs Laser Pumped by Cs-Ar Photoassociation". *Applied Physics Letters*, 102:111104–111104–4, 2013.

34. J. Readle, J. Eden S. Davis K. Gabally-Kinney W. Rawlins, J. Verdeyen and W. Kessler. "Cs 894.3 nm laser pumped by photoassociation of Cs-Kr pairs: excitation of the Cs D_2 blue and red satellites". *Optics Letters*, 34(23):3638–3640, 2009.

35. J. Readle, J. Verdeyen D. Carroll, C. Wagner and J. Eden. "Lasing in Cs at 894.3 nm pumped by the dissociation of CsAr excimers". *Electronic Letters*, 44(25), 2008.

36. J. Readle, J. Verdeyen D. Carroll, C. Wagner and J. Eden. "Lasing in alkali atoms pumped by the dissociation of alkali-rare gas exciplexes (excimers)". High Energy/Average Power Lasers and Intense Beam Applications III. 2009. SPIE proceedings volume 7196.

37. J. Readle, J. Verdeyen D. Carroll, C. Wagner and J. Eden. *Applied Physics Letters*, 97:021104, 2010.

38. J. Readle, J. Verdeyen T. Spinka D. Carroll, C. Wagner and J. Eden. "Pumping of atomic alkali lasers by photoexcitation of a resonance line blue satellite and alkali-rare gas excimer dissociation". *Applied Physics Letters*, 94(251112), 2009.

39. J. Schultz, D. Doring J. Debs P. Altin-J. White N. Robins, S. Abend and J. Close. "Coherent 455nm beam production in a cesium vapor". *Optics Letters*, 34(15):2321–2323, 2009.

40. J. Shultz, D. Doring J. Debs P. Altin-J. White N. Robins, S. Abend and J. Close. *Optics Letters*, 34:2321, 2009.

41. Jones, P. *Broadband Pumping Effectson the Diode Pumped Alkali Laser*. M.S. thesis, Graduate School of Engineering, Air Force Institute of Technology (AETC), Wright-Patterson AFB OH, March 2011. AFIT/GAP/ENP/11-M04.

42. K. Brown, E. Hurd and G. Perram. *Tunable Hyper-Raman Laser in Potassium Vapor*, 42nd AIAA Plasmadynamics and Lasers Conference. AIAA, 2011.

43. K. Saha, P. Londero, V. Venkataraman and A. Gaeta. "Enhanced two-photon absorption in a hollow-core photonic-band-gap fiber". *Physical Review A*, 83(033833), 2011.

44. Kaiser, W. and C. Garrett. "Two-photon excitation in CaF_2:Eu_2". *Physical Review Letters*, 7:229–232, 1961.

45. Ko, M. and Y. Liu. "Observation of rubidium $5S_{1/2} \longrightarrow 7S_{1/2}$ two-photon transitions with a diode laser". *Optics Letters*, 29(15):1799–1801, 2004.

46. L. Blank, D. Weeks and G. Kedziora. "M + Ng potential energy curves including spin-orbit coupling for M=K, Rb, Cs and Ng=He, Ne, Ar". *The Journal of Chemical Physics*, 136(124315), 2012.

47. Levenson, M. and N. Bloembergen. "Observation of Two-Photon Absorption without Doppler Broadening on the $3S$-$5S$ Transition in Sodium Vapor". *Physical Review Letters*, 32(12):645–648, 1974.

48. Lott, G. *Cesium Absorption Spectrum Perturbed by Argon: Observation of Non-Linear Wing Properties*. M.S. thesis, Graduate School of Engineering, Air Force Institute of Technology (AETC), Wright-Patterson AFB OH, March 2012. AFIT/APPLPHY/ENP/12-M08.

49. M. Marinescu, V. Florecu and A. Dalgarno. "Two-photon excitation of the 5^2D states of rubidium". *Physical Review A*, 49(4):2714, 1994.

50. M. Niering, J. Reichert P. Pokasov T. Udem-M. Weitz, R. Holzwarth and T. Hansch. "Measurement of the Hydrogen 1S-2S Transition Frequency by Phase Comparison with a Microwave Cesium Fountain Clock". *Physical Review Letters*, 84(24):5496–5499, 2000.

51. Maiman, T. "Stimulated optical rediation in ruby". *Nature*, 187:493–494, 1960.

52. Moulton, P. "Spectroscopic and laser characteristics of Ti:Al_2O_3". *Journal of Optical Society B*, 3:125, 1986.

53. O. Roslyak, C. Marx and S. Mukamel. "Generalized Kramers-Heisenberg expressions for stimulated Raman scattering and two-photon absorption". *Journal of Physics A*, 79, 2009.

54. P. Rabinowitz, S. Jacobs and G. Gould. "Continuous Optically Pumped Cs Laser". *Applied Optics*, 1(4):513–516, 1962.

55. R. Beach, V. Kanz, V. Krupke and S. Payne. *Diode-Pumped Alkali Atom Lasers*. Technical report, Lawrence Livermore National Laboratory, 2005.

56. R. Beach, V. Kanz, W. Krupke and S. Payne. "End-pumped continuous-wave alkali vapor lasers: experiment, model, and power scaling". *Journal of Optical Society of America B*, 21(12):2151–2163, 2004.

57. R. Page, V. Kanz, R. Beach. "Multimode-diode-pumped gas (alkali-vapor) laser". *Optics Letters*, 31(3):353–355, 2006.

58. R. Page, V. Kanz, R. Beach and W. Krupke. *First demonstration of a diode-pumped gas (alkali vapor) laser*. Technical report, Lawrence Livermore National Laboratory, 7000 East Ave., Livermore California 94551-0808, 2005.

59. S. Hamadani, R. Compton, J. Stockdale and M. Pindzola. "Two-photon resonant four-wave mixing and multiphoton ionization of cesium in a heat-pipe oven". *Applied Physics letters*, 34(3), 1986.

60. S. Yatisv, G. Picus, W. Wagner and F. McClung. "Saturation of a Resonant Optical Double-Quantum Transition". *Physical Review Letters*, 15(15):614–618, 1965.

61. Schawlow, A. and C. Townes. "Infrared and Optical Masers". *Physical Review*, 112(6):1940–1949, 1958.

62. Steck, D. *Rubidium 87 Line Data*. Los Alamos National Laboratory, Theorectical Division (T-8), MS B285, Los Alamos, NM 87545, 2003.

63. T. Meijer, B. Smeets M. Jeppesen, J. White and R. Scholten. "Blue five-level frequency-upconversion system in rubidium". *Optics Letters*, 31(7):1002–1004, 2006.

64. Theodosiou, C. "Lifetimes of alkali-metal-atom Rydberg states". *Physics Review A*, 30(6):2881–2909, 1984.

65. W. Krupke, K. Kanz, R. Beach and S. Payne. "Resonance Transition 795-nm Rubidium Laser". *Optics Letters*, 28(23):2336, 2003.

66. W. Krupke, V. Kanz S. Payne, R. Beach and J. Early. *New Class of CW High-Power Diode-Pumped Alkali Lasers (DPALs)*, High-Power Laser Ablation 2004. Lawrence Livermore National Laboratory, Taos, New Mexico, United States, April 2004.

67. W. Zapka, F. Schellenberg A. Tam, M. Levenson and G. Bjorklund. "Continuous-wave Doppler-free two-photon frequency-modulated spectroscopy in Rb vapor". *Optics Letters*, 8(1):27, 1983.

68. Yatsiv, S. and M. Rokni. "Resonance Raman effect in free atoms of potassium". *Physical Letters A*, 24(5):277–278, 1967.

REPORT DOCUMENTATION PAGE

Form Approved
OMB No. 0704–0188

1. REPORT DATE (DD–MM–YYYY)	2. REPORT TYPE	3. DATES COVERED *(From — To)*
13-06-2013	Dissertation	01-10-2008 – 13-06-2013

4. TITLE AND SUBTITLE
Optically Pumped Atomic Rubidium Lasers: Two-Photon and Exciplex Excitation Mechanisms

5a. CONTRACT NUMBER
5b. GRANT NUMBER
5c. PROGRAM ELEMENT NUMBER

6. AUTHOR(S)
Gallagher, Jeffrey E, Maj

5d. PROJECT NUMBER
5e. TASK NUMBER
5f. WORK UNIT NUMBER

7. PERFORMING ORGANIZATION NAME(S) AND ADDRESS(ES)
Air Force Institute of Technology
Graduate School of Engineering and Management (AFIT/ENY)
2950 Hobson Way
WPAFB OH 45433-7765

8. PERFORMING ORGANIZATION REPORT NUMBER
AFIT-ENP-DS-13-J-01

9. SPONSORING / MONITORING AGENCY NAME(S) AND ADDRESS(ES)
Harro Ackerman (505) 248-8208
High Energy Laser Joint Technology Office
901 University Blvd. S.E. Suite 100
Kirtland AFB, NM 87106

10. SPONSOR/MONITOR'S ACRONYM(S)
HEL JTO

11. SPONSOR/MONITOR'S REPORT NUMBER(S)

12. DISTRIBUTION / AVAILABILITY STATEMENT
APPROVED FOR PUBLIC RELEASE; DISTRIBUTION UNLIMITED

13. SUPPLEMENTARY NOTES This material is declared a work of the U.S. Government and is not subject to copyright protection in the United States.

14. ABSTRACT

The Doppler-broadened two-photon absorption (TPA) cross-section for the $5^2S_{1/2}$-> $5^2D_{5/2}$ transition in Rb is measured using direct absorption methods. A detailed model of the intensity profile was developed to account for a focused Gaussian beam propagating through a two-photon absorption medium. A peak absorbance of 24% was observed for an intensity of 6.28 kW/cm^2 at the focus, a Rb density of 4.6×10^{15} cm^{-3} concentrations from $1.61-8.52 \times 10^{15}$ cm^{-3} line. Extracting the hyperfine-broadened TPA cross-section from 87 test configurations, while varying the pump power, alkali concentration and focal length, yielded an error-weighted average of 6.75×10^{-21} cm^4/W. This cross-section is sufficient for a pulsed dye laser to bleach the pump transition in the Two-Photon Pumped Alkali Laser (TPAL) that lases at 420 nm and 5.2 μm. Additionally, optically pumped atomic rubidium lasers pumped in the blue satellite of the D_2 line from the ground Rb-Ar or Rb-Kr collision pair to the dissociative $B^2\Sigma_{1/2}$ produce laser emission at 780.2 nm. Lasing is achieved for the Rb-Ar system and 757.1 − 760.4 nm for the Rb-Kr system. Slope efficiencies exceed 0.25% using a heat pipe configuration. The gain is very high with photon build-up times of 1−3.7 ns.

15. SUBJECT TERMS
Two-photon absorption cross section, excimer pumped alkali lasers, heat pipe, rubidium alkali laser

16. SECURITY CLASSIFICATION OF:			17. LIMITATION OF ABSTRACT	18. NUMBER OF PAGES	19a. NAME OF RESPONSIBLE PERSON
a. REPORT	b. ABSTRACT	c. THIS PAGE	UU	157	Dr. Glen P. Perram AFIT/ENP
U	U	U			19b. TELEPHONE NUMBER (Include Area Code) (937)255-3636, ext